University of Salerno
Department of Chemistry and Biology

UNIVERSITÀ DEGLI STUDI
DI SALERNO

Ph.D. Thesis in Chemistry

"Carbon-based nanomaterials"

Mario Maggio

Tutor: prof. Gaetano Guerra
Co-tutor: prof. Pasquale Longo
Tutor esterno: dr. Luca Giannini

XXIX Cycle 2014-2017

Introduction

Chapter 1

Carbon Allotropes

1.1 Carbon Allotropes / **9**
1.2 Structures of Layered Carbons / **10**
1.2.1 Graphites / **11**
1.2.2 Turbostratic Graphites / **13**
1.2.3 Amorphous Carbons / **15**
1.2.4 Carbon Blacks / **16**
1.2.5 Carbon Nanotubes / **18**
1.3 Structural Characterization of Graphitic Materials for the Preparation of Anisotropic Carbon Nanofillers / **20**
1.4 Graphite Oxide / **24**
1.4.1 Preparation, Composition and Surface Areas of Graphite Oxide Samples / **25**
1.4.2 Characterization of Graphite Oxide Samples / **28**
1.4.3 Mechanical Exfoliation of Graphite Oxide / **31**

Chapter 2

Experimental part:
Materials, preparation procedures and characterization techniques

2.1 Preparation of GO with Higher Content of Oxygenated Groups / **41**
2.2 Preparation of GO with Lower Content of Oxygenated Groups / **41**
2.3 Preparation of GOICs / **41**
2.4 Preparation of GO and GOIC films / **42**
2.5 Preparation of Chemically Reduced Graphite Oxide / **42**
2.6 Graphite Oxide Exfoliation by Ball-Milling / **43**
2.7 GO paper preparation / **43**

2.8 Preparation of adducts of oxidized carbon black with ammonium ions with long alkyl chains / **44**
2.9 Oxidation of carbon blacks with different surface area /**44**
2.10 Wide Angle X-ray Diffraction / **45**
2.11 Fourier Trasform Infrared Spectroscopy / **47**
2.12 Differential Scanning Calorimetry / **47**
2.13 Thermogravimetric Analysis / **47**
2.14 Elemental Analysis / **48**
2.15 BET Surface Area Measurements / **48**
2.16 Scanning Electron Microscopy / **48**
2.17 Transmission Electron Microscopy / **48**
2.18 Back Titration of Graphite Oxides / **49**

Chapter 3

Intercalation Compounds of graphite oxide

3.1 Graphite Oxide Intercalation Compounds with long alkyl chains ammoniun cations / **53**

3.2.1 Characterization of graphite intercalation compounds with ammonium cations / **54**

3.2.2 Structural reversibility of the graphite oxide intercalation compounds with temperature / **58**

3.2.3 Structure of the graphite oxide intercalation Compounds / **59**

3.3 Graphite Oxide Intercalation and Exfoliation compounds with Phosphonium ions / **62**

3.3.1 Intercalation compounds with quaternary phosphonium ions / **62**

3.3.2 Exfoliation compounds with quaternary phosphonium ions / **65**

3.3.3 Structural Organization of GOIC and GOEC Compounds with TPP^+ / 6**7**

3.3.4 Spectroscopic characterization of GOIC and GOEC Compounds with TPP+ / **69**

3.3.5 Release of Organo-Phosphonium Ions in Aqueous Solutions from GOIC and GOEC / **71**

Conclusions / **74**

CHAPTER 4

Carbon Black Oxide and Carbon black oxide adducts with organic ammonium ions

4.1 Preparation, Composition and Surface Areas of Carbon Black Oxide Samples / **81**
4.2 oCB/2HT adducts / **88**
Conclusions / 93

CHAPTER 5

Graphite and Graphene Oxide paper

5.1 Structural characterizations of GO and b-GO papers / **99**
5.2 Structural changes with thermal and microwave treatments / **103**
5.3 Thermal behavior / **106**
5.4 Dimensional stability in solvents / **108**
5.5 Paper flexibility / **111**
5.6 FTIR characterization and possible rationalization of b-GO properties / **112**
Conclusions / **115**

General Conclusions

Introduction

Carbon-based nanomaterials have become important due to their unique combinations of chemical and physical properties (*i.e.*, thermal and electrical conductivity, high mechanical strength, and optical properties), and extensive research efforts are being made to utilize these materials for various industrial applications, such as high-strength materials and electronics.

In particular, layered oxidized carbon-based nanomaterials, like graphite and graphene oxide, can be easily manipulated not only to obtain intercalation and/or exfoliation compounds with organic ions, but also to form thermally stable, solvent resistant and flexible papers.

This PhD thesis reports some advances in the field of carbon-based nanomaterials.

In **Chapter 1**, as literature reports, well-known carbon allotropes are described, focusing on their structure properties. A substantial part of this chapter also reports preparation procedures and characterization of graphite oxide, as described in PhD thesis of Marco Mauro (2011-2014).

In **Chapter 2** and **3**, materials, preparation procedures and characterization techniques are listed and described in detail.

The following chapters report the main results obtained during this PhD program.

Chapter 4 shows the preparation and structural characterizations of graphite oxide (GO), graphite oxide intercalation compounds (GOICs) and graphite oxide exfoliation compounds (GOEC) with organic ions.

Specifically, when intercalation of organic cations containing two long hydrocarbon tails (quaternary ammonium ions) is obtained, the GOICs exhibit a large distance between graphite oxide sheets as well as a long-range order in the organization of guest species.

Moreover, for the first time for phosphonium salts (known for their antibacterial activity), it is reported the preparation procedures that are suitable to produce highly ordered graphite oxide intercalation compounds (GOIC) or fully disordered graphite oxide exfoliated compounds (GOEC).

These intercalated and exfoliated compounds are structurally characterized, and their largely different ion release behaviors in neutral and acid aqueous solutions are compared. In the first part of **Chapter 5**, oxidation studies on different carbon black (CB) samples, exhibiting largely different BET surface areas, are reported. While in the second part of the **Chapter 5** formation of an intercalate crystalline structure of small and highly disordered oxidized CB layers is for the first time reported. This intercalate is obtained by self-assembling of CB with ammonium ions with two long hydrocarbon tails (similar to those reported in **Chapter 4**), and its crystalline structure is described mainly on the basis of x-ray diffraction (WAXD) patterns.

In addition to a rich intercalation chemistry, graphene oxide can be used to produce free-standing papers by vacuum filtration of colloidal dispersions.

Therefore, **Chapter 6** presents graphene oxide papers, prepared by suspending graphite oxide powders in basified aqueous solution, that exhibit thermal stability and solvent resistance much higher than usual GO papers. In this way casting procedures, which are generally unsuitable for production of robust GO papers, become suitable for basified GO.

Chapter 1

Carbon Allotropes

1.1 Carbon Allotropes

Carbon, the sixth element in the Periodic Table of Elements, is truly remarkable for its extraordinary ability of catenation to combine with itself and other chemical elements in different ways and thereby form the basis of organic chemistry and of life. Diamond and graphite are well-known allotropes of carbon. Elemental carbon with sp^3 hybridization builds up a tetrahedral lattice, giving rise to diamond (**Fig. 1.1A**), while sp^2 hybridized extended networks are responsible for the formation of graphite (**Fig. 1.1B**).

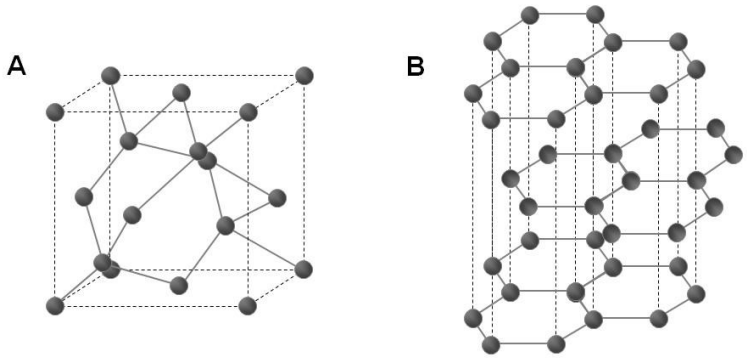

Figure 1.1. Crystal structures of (A) diamond and (B) hexagonal graphite.

Graphene is an atomically thick, two-dimensional (2D) sheet composed of sp^2 carbon atoms arranged in a honeycomb structure

(**Scheme 1.1**). It has been viewed as the building block of all other graphitic carbon allotropes of different dimensionality. For example, graphite (3D carbon allotrope) is made of graphene sheets piled on top of each other with …*ABABAB*… stacking and separated by 0.335 nm. More disordered graphitic structures exist for coals, cokes and carbon blacks. The 0D carbon allotrope, fullerenes (buckyballs), can be envisioned to be made by wrapping a section of graphene sheet. The 1D carbon allotropes, carbon nanotubes (CNT), can be made by rolling graphene sheets.

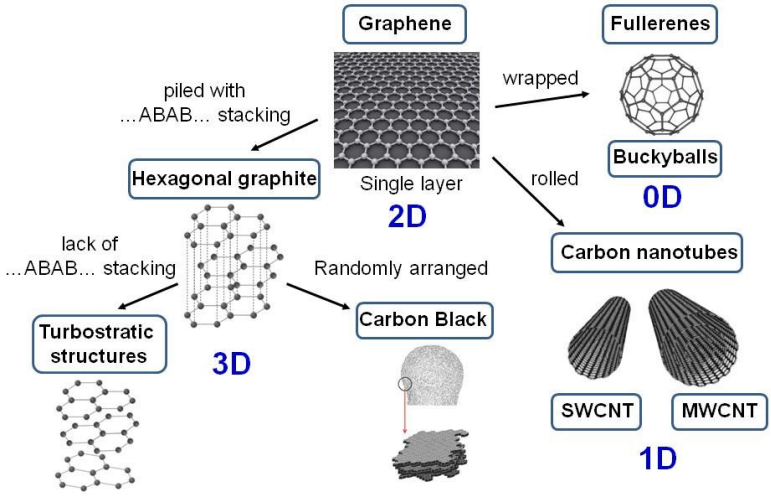

Scheme 1.1. Mother of all graphitic forms. Graphene is a 2D building material for carbon materials of all other dimensionalities. It can be wrapped up into 0D buckyballs, rolled into 1D nanotubes, piled with a …*ABABAB*… stacking into 3D graphite or randomly stacked in primary particles of carbon black.

1.2 Structures of Layered Carbons

Materials with layers of sp^2-bonded carbon atoms exhibit a large variety of structures characterized by different degree of structural order and morphologies. These materials, principally, differ for their degree of order perpendicular to the graphitic layers (out-of-plane order) and in the graphitic layers (in-plane order).

The structures of layered carbons, from ordered graphites to amorphous carbons, are discussed in the following. A systematic X-ray diffraction characterization of different graphitic materials was also performed, in order to select the most suitable starting material for the preparation of anisotropic carbon nanofillers to be used in rubber nanocomposites.

1.2.1 Graphites

Graphite is a crystalline, polymorphic form of elementary carbon with ordered layers. Each carbon atom in the graphite crystal is hybridised trigonally, forming three σ and one π bonds. The hybridised orbitals of the sp^2 type give σ bonds of a length of 1.42 Å, arranged at 120° angles with respect to one another, with sheets made up of regular hexagons. The fourth electron of each atom, being in the p orbital, forms π bonds with all the neighbouring atoms. The structure of graphite consists of six-membered rings in which each carbon atom has three near neighbours at the apices of an equilateral triangle. Within the large planar layers, there are linkages intermediate between atomic and metallic bonds. The layers in the crystal are held together by van der Waals bonding forces. Weak bonding perpendicular to the layers gives rise to easy gliding parallel to the sheets.**[1]**

According to the structural model proposed by Hull in 1917 **[2]** and described by Bernal in 1924,**[3]** the hexagonal unit cell of hexagonal graphite contains four atoms in the positions listed below compared to the reference system in **Fig. 1.2**:

(0,0,0) ; (0,0,1/2) ; (1/3,2/3,1/2) ; (2/3,1/3,0)

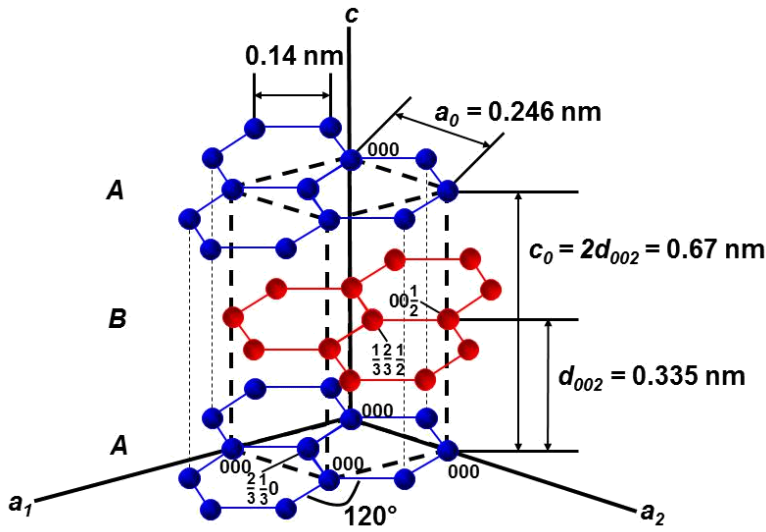

Figure 1.2. Detailed crystal structure of hexagonal graphite.

Hexagonal graphite consists of sheets stacked along the crystallographic *c* axe with a regular …*ABABAB*… sequence and lattice costant c_0 = 0.67 nm (see **Fig. 1.2**). The X-ray diffraction analysis is the most powerful tool to study the structure of graphites and of carbon materials in general. The hexagonal graphite reflections can be classified into three groups: reflections with 00ℓ, hk0 and hkℓ indices. Reflections with 00ℓ are due to the diffraction from the basal planes stacked along the crystallographic *c* axe. Only even ℓ values are permitted because of the systematic extinction of 00ℓ reflections with odd ℓ values, related to the …*ABABAB*… stacking. Reflections with hk0 are due to the diffraction from the crystal planes perpendicular to the basal planes and the hkℓ reflections are related to the diffraction from the inclined planes respect to the basal planes.

The X-Ray diffraction pattern of hexagonal graphite in **Fig. 1.3 [4]** presents the 002, 004 and 006 reflections characteristic of the stacking along the crystallographic *c* axe, while the 100 and 110 reflections are related to the order inside the graphitic layers. The distance between the *A* and *B* planes is the Bragg's distance *d002* = 0.335 nm and the distance

between the *A* and *A* planes is the lattice costant *c0* = *2d002* = 0.67 nm. The Bragg's distances *d100* = *a0· cos(30°)* = 0.213 nm and *d110* = *a0· sin(30°)* = 0.123 nm, are related to the 100 and 110 planes, orthogonal to the *A* and *B* planes (see **Fig. 1.2**).

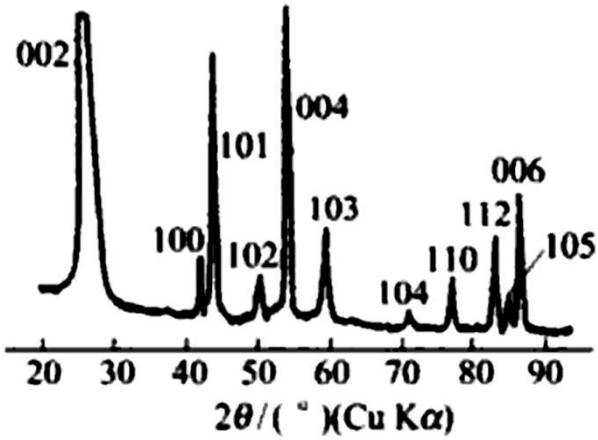

Figure 1.3. X-ray diffraction (Cu Kα) pattern of hexagonal graphite

1.2.2 Turbostratic Graphites

The described hexagonal structure of graphite refers to its crystalline form defined as ideal models. However, in nature graphite usually appears in less perfect forms and in a variety of disordered types from the so-called turbostratic graphites to the amorphous carbons.

According to the random layer lattice structural model proposed by Warren in 1941, turbostratic graphite is characterized by the lack of …*ABABAB*… stacking with graphitic sheets randomly translated to each other and rotated respect to the normal of the layers (see **Scheme 1.2**).**[5]**

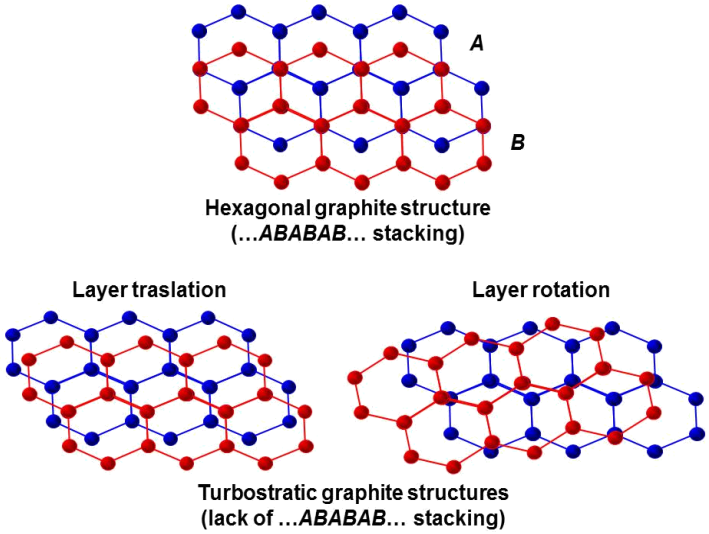

Scheme 1.2. Top view of the turbostratic graphite structures compared with the hexagonal graphite structure, after ref. 4.

Distortions from the hexagonal graphite structure determine the intensity decrease or the disappearance of hkℓ reflections, such as 101, 102, 103, 104, 105 and 112, while the 00ℓ and the hk0 reflections are not suppressed. The Bragg's distance *d002* and the width at half height *β002* increase.**[6]**

Turbostratic structures are often observed in extensively ball-milled graphites **[7]** or in carbon materials heated at relatively low temperatures of 1300–1500 °C,**[8]** where the size of each layer is small and only a few layers are stacked in ordered manner. By heating these carbons to high temperatures, up to 3000 °C,**[9]** both the size and number of stacked layers usually increase, and the regularity in stacking is also improved. Heat treatment at intermediate temperatures gives a partial improvement in stacking regularity. A wide range of structures from completely turbostratic structures to graphite structures with pure …*ABABAB*… stacking is possible, depending primary on the starting materials and the heat treatment temperature.

1.2.3 Amorphous Carbons

Amorphous carbons such as coals, cokes and carbon blacks are materials without long-range crystalline order. Short-range graphite-like order still exists, and the degree of this kind of order gives rise to intermediate structures between the graphitic and the completely amorphous (lack of any crystalline structure) carbons, according to the random layer lattice structural model.**[5]** Deviations of the interatomic distances and interbonding angles with respect to the graphite lattice as well as to the diamond lattice occur in such materials.

The X-Ray diffraction pattern of petroleum coke heat treated at 1000 °C in **Fig. 1.4 [4]** is characterized by very broad 00ℓ reflections, due to the small number of layers stacked in an orered manner, unsymmetrical two-dimensional hk reflections, and no hkℓ reflections, due to random turbostratic stacking of the layers.

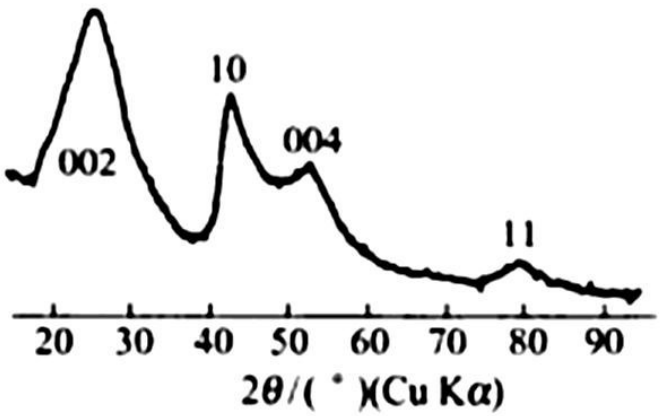

Figure 1.4. X-ray diffraction (Cu Kα) pattern of petroleum coke heat treated at 1000 °C.

The structure of amorphous carbons with short-range graphite-like order can be rationalized by the Franklin's model proposed in 1950.**[10]** According to this model, this kind of carbons are characterized by two types of carbon structures: carbon crystallites and completely amorphous carbon. Small graphitic crystallites, containing few layers, are joined together by cross-links. These cross-links are established by aliphatic chains on the edges of each crystalline domains. The structural units in non-graphitizing carbons are distributed randomly, and the cross-links are sufficiently strong to impede movement of the layers into a more parallel arrangement (see **Fig 1.5A**). The structural units in a graphitizing carbon are approximately parallel to each other, and the links between adjacent units are assumed to be weak (see **Fig 1.5B**).**[11]**

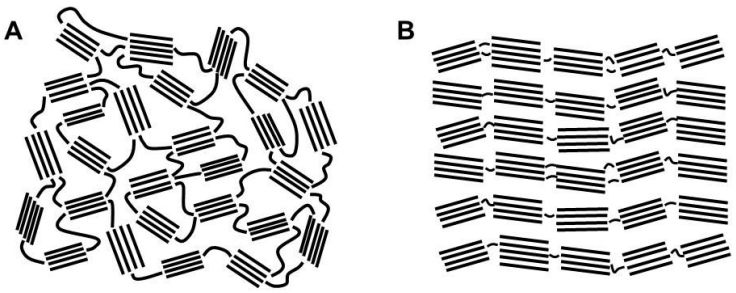

Figure 1.5. Franklin's structural model of: (A) non-graphitizing and (B) graphitizing carbons.

1.2.4 Carbon Blacks

Carbon blacks (CBs), formed through incomplete combustion of high molecular weight hydrocarbon fractions of petroleum crude oils, coal tar, ethylene cracking tar, and vegetable oil, are very important industrial products, in particular these materials are the most important reinforcing

filler used to improve strenght, rolling resistance and abrasion resistance in tire compounds.

CB samples are characterized by aggregates (200 – 1000 nm) of nearly spherical particles (20 - 100 nm) with an internal structure made of graphite-like units having a random orientation of the graphitic layers, as shown in **Fig. 1.6**.**[12]**

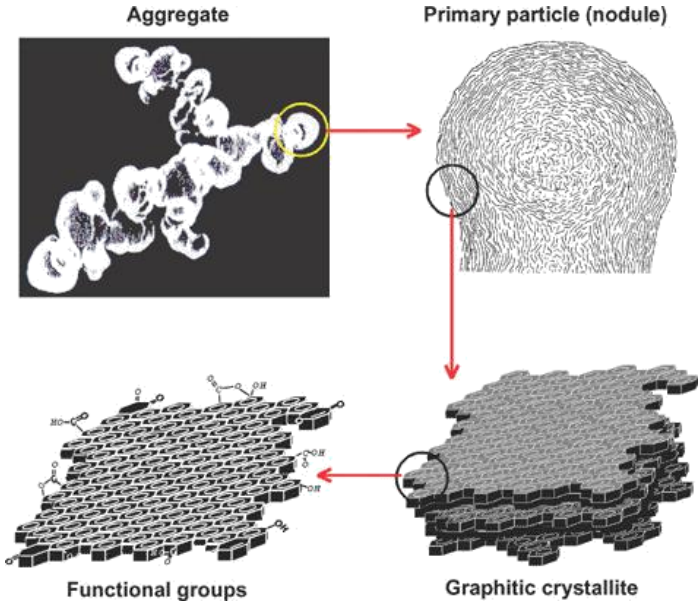

Figure 1.6. Structure of carbon black aggregates.

CB powders are characterized by high surface areas, as a consequence of their nanometric primary particles, that determine high filler-polymer interfacial areas, when CB particles are dispersed in a polymer matrix. The degree of aggregation of primary particles defines a very important technological parameter, the so-called ‘‘structure’’ of CBs. High structure

CBs are characterized by high degree of aggregation (low void volume) (see **Fig. 1.7**)

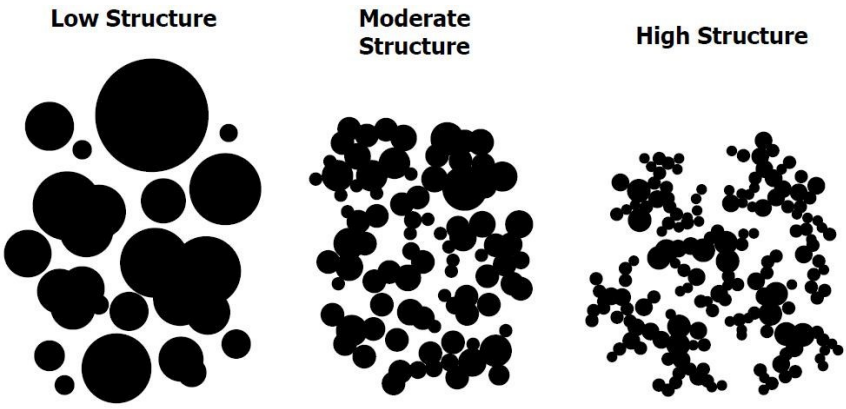

Figure 1.7. Degree of aggregation of primary particles of carbon black.

Another peculiar feature of CB particles is their surface activity, that derives from both high energy graphitic edges and the oxygen groups (carbonyl, carboxylic, lactonic and phenolic groups), at the edges of each graphitic layer (see **Fig. 1.6**). The surface activity of CB particles is responsible for the filler-filler and filler-polymer interactions in polymeric nanocomposites.

1.2.5 Carbon Nanotubes

The discovery of carbon nanotubes (CNT) in 1991 opened up a new era in materials science by Lijima **[13]**. These incredible structures have an array of fascinating electronic, magnetic and mechanical properties. CNT are at least 100 times stronger than steel, but only one-sixth as heavy, so nanotube fibers could strengthen almost any material.**[14]** Nanotubes can

conduct heat and electricity far better than copper. CNT are already being used in polymers to control or enhance conductivity and mechanical properties.

Carbon nanotubes are composed of carbon atoms linked in hexagonal shapes, with each carbon atom covalently bonded to three other carbon atoms. Carbon nanotubes have diameters as small as 1 nm and lengths up to several centimeters. Although, like buckyballs, carbon nanotubes are strong, they are not brittle. They can be bent, and when released, they will spring back to their original shape. Carbon nanotubes can occur as multiple concentric cylinders of carbon atoms, called multi-walled carbon nanotubes (MWCNTs) and as one cylinder which are called single-walled carbon nanotubes (SWCNTs) (**Fig. 1.8**). Both MWCNT and SWCNT are used to strengthen composite materials. **[15, 16]**

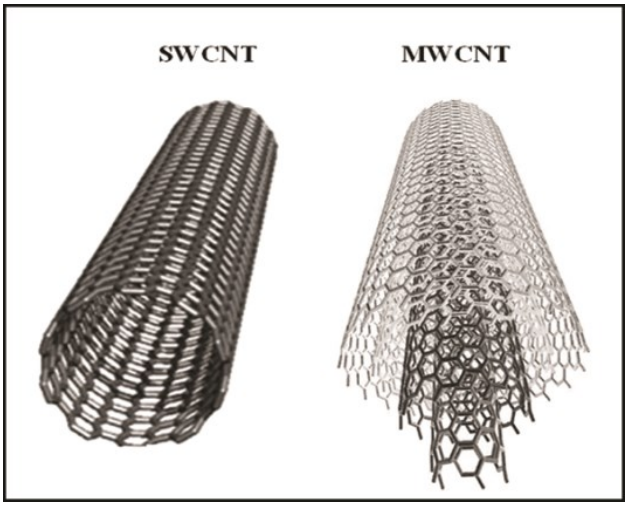

Figure 1.8 Structure of Single-Walled Carbon Nanotubes (SWCNT) and Multi-Walled Carbon Nanotubes (MWCNT)

1.3 Structural Characterization of Graphitic Materials for the Preparation of Anisotropic Carbon Nanofillers

Physical properties of fillers and of composites based on them are better when fillers have a high anisotropy,**[17–21]** that means when they have short and long correlation lengths in the direction perpendicular and parallel to the structural layers, respectively.

Among layered fillers based on sp^2-carbon atoms, highly anisotropic graphites, with a high in-plane order and a reduced out-of-plane order, are the most suitable starting material for the preparation of anisotropic carbon nanofillers. In this respect, aiming to select a graphite with high shape anisotropy of the crystallites and a long-range structural order in graphene layers, a systematic X-ray diffraction characterization of different graphitic materials was performed.

The X-ray diffraction patterns of six commercial graphitic materials are compared in **Fig. 1.9** and are organized from A to F, on the basis of a progressive reduction of structural order. The relative Williamson-Hall plots are presented in **Fig. 1.10** and the derived correlation lengths and strains, parallel and perpendicular to the structural layers, are reported in **Table 1.1**. Of course, errors in correlation lengths and strains, when only two reflections are available, can be large (up to 10 % for samples D-F).

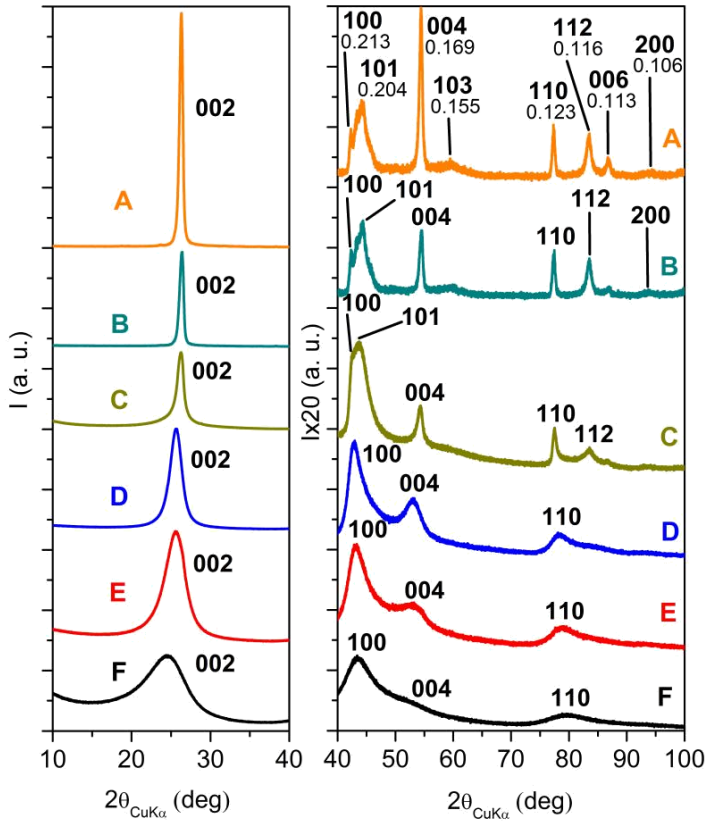

Figure 1.9. X-ray diffraction patterns (Cu Kα) of six commercial graphitic materials: (A, B) graphites, (C) ball-milled graphite, (D, E) needle coke and calcined petroleum coke and (F) carbon black N326. The patterns are reported from A to F on the basis of a progressive reduction of structural order.

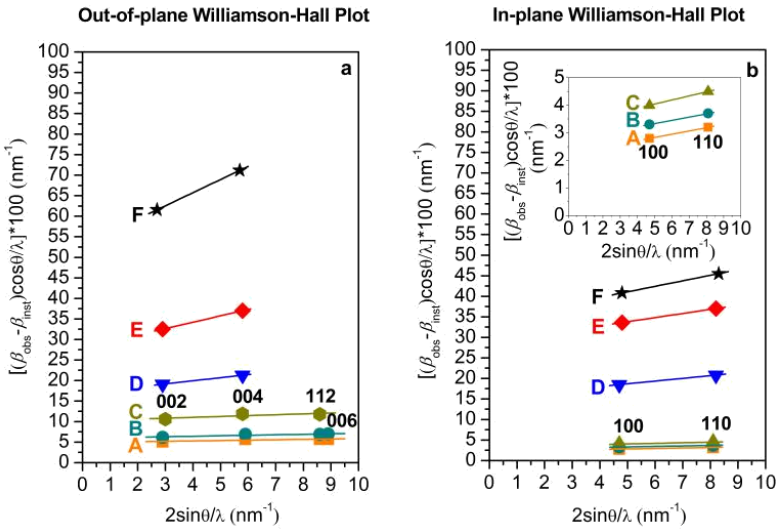

Figure 1.10. Out-of-plane (a) and in-plane (b) Williamson–Hall plots for the graphitic samples from A to F, whose X-ray diffraction patterns are reported in Fig. 2.8.

Table 1.1. Structural parameters derived from Bragg's lawand Williamson-Hall plots of Fig. 2.9.

Sample	*d*002 (nm)	$D_\perp$ (nm)	$D_\parallel$ (nm)	$D_\parallel / D_\perp$	$\varepsilon_\perp$ (%)	$\varepsilon_\parallel$ (%)	$\varepsilon_\perp / \varepsilon_\parallel$
A	0.339	20.3	44.5	2.2	0.047	0.059	0.8
B	0.339	16.8	36.4	2.2	0.060	0.059	1.0
C	0.339	9.8	30.2	3.1	0.107	0.073	1.5
D	0.347	5.9	6.5	1.1	0.38	0.33	1.1
E	0.348	3.5	3.6	1.0	0.78	0.50	1.5
F	0.365	1.9	2.9	1.5	1.6	0.67	2.4

All samples of **Fig. 2.8** present broad 00ℓ reflections and out-of-plane correlation lengths (3rd column of **Table 1.1**) from 20 nm down to 2

nm. Moreover, all samples of **Fig. 2.8**, due to their structural disorder, present distances between the structural layers (d002 in the 2nd column of **Table 1.1**) slightly larger than those of ordered graphite samples (d002 = 0.335 nm).**[22]**

In particular, for samples A-C, the in-plane correlation lengths (4th column of **Table 1.1**) are larger than the out-of-plane correlation lengths (3rd column of **Table 1.1**) and the out-of-plane correlation length is significantly reduced for sample C. Moreover, going from A to C there is also a progressive reduction of the intensities of the 101 and 112 reflections with respect to the hk0 reflections. This clearly indicates a progressive increase of disorder in the relative position of parallel graphitic layers and hence a tendency toward the so-called turbostratic graphite.**[6]** An almost perfect turbostratic structure is present in samples D-F, whose 101 and 112 reflections are negligible.

Samples D-F exhibit low out-of-plane correlation lengths (corresponding to few graphitic layers). However, their in-plane correlation lengths are also low, thus leading to poor shape anisotropy of the crystallites (5th column of **Table 1.1**).

The whole structural information from **Figs 1.8–1.9** (and **Table 1.1**) clearly indicates that the ball-milled graphite (sample C in **Fig. 1.8**, renamed G in the following), which presents the highest shape anisotropy ($D_{\parallel}$ / $D_{\perp}$ = 3.1, see **Scheme 1.3**), associated with a large in-plane correlation length and a reduced order in the relative position of parallel graphitic layers, appears to be the most suitable starting material for the preparation of anisotropic carbon nanofillers (see the next paragraphs) to be used in rubber nanocomposites.**[23]**

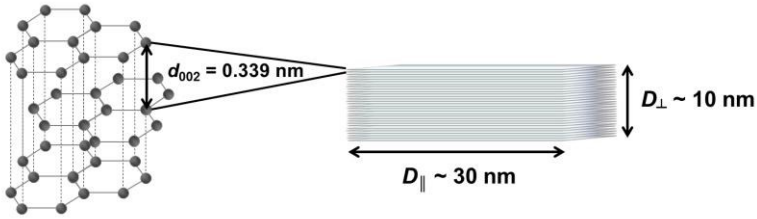

Scheme 1.3. Schematic representation of G with a basal spacing of *d*002 = 0.339 nm and a high shape anisotropy of $D_{\parallel} / D_{\perp} \approx 3$.

1.4 Graphite Oxide

Graphite oxide (GO) is a layered material, which can be obtained by chemical oxidation of graphite. Graphite oxide can be prepared by the treatment of graphite with strong mineral acids and oxidizing agents, typically via treatment with a mixture of sulfuric and nitric acid, using potassium chlorate, as in the Brodie's **[24]** or Staudenmaier's **[25]** methods, or with a mixture of sodium nitrate and concentrated sulfuric acid, using potassium permanganate, as in the Hummers' method.**[26]**

The precise structure of GO remains a matter of debate,**[27]** and, according to the Lerf-Klinowski model,**[28]** GO consists of oxidized sheets having oxygen containing functional groups, that confer polar surface properties and a strong hydrophilic character. Hydroxyl and epoxide groups are at the surface of the basal planes and carbonyl and carboxyl groups are at the edges. Therefore, GO forms colloidal dispersion in water, which are stabilized by negative charges from the carboxyl groups, without the need for any surfactant.**[29]**

1.4.1 Preparation, Composition and Surface Areas of Graphite Oxide Samples

Two sets of GO samples, containing higher (H-GO) and lower (L-GO) oxygen content, were prepared by using Staudenmaier's method and Hummers' method, respectively, starting from the highly anisotropic graphite G. The oxidation methods of G are represented in **Scheme 1.4**.

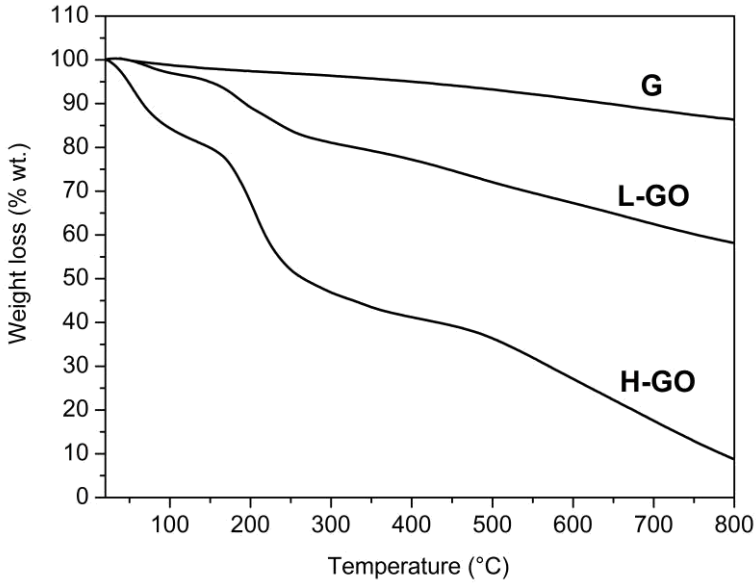

Scheme 1.4. Schematic representation of the oxidation reactions of the graphite (G) with Staudenmaier's and Hummers' methods.

Measurements of the water loss up to 150 °C by TGA (roughly 20 %wt. for H-GO and 5 %wt. for L-GO), reported in **Fig. 1.10**, and elemental analysis of the GO powders, reported in **Table 1.2**, indicate that the carbon to oxygen weight ratio (see C/O ratios in **Table 2.2**) in H-GO is about 1.6 and 1.9 in L-GO. Hence, the compositions of GO samples are $CO_{0.47}H_{0.2}\cdot 0.28H_2O$ for H-GO and $CO_{0.39}H_{0.12}\cdot 0.05H_2O$ for L-GO.

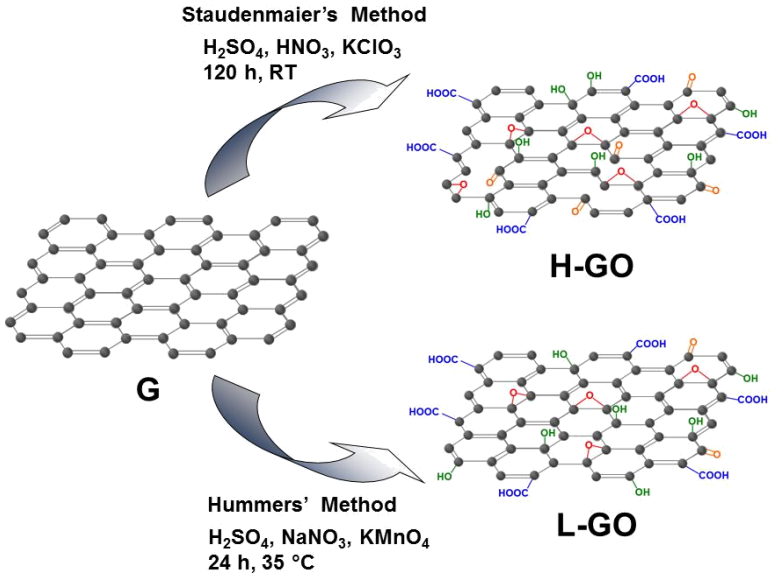

Figure 1.10. TGA curves in N_2 of the starting high surface area graphite (G) and of the derived L-GO and H-GO.

Table 1.2. Results of elemental analysis and BET measurements on the starting high surface area graphite G and of the derived L-GO and H-GO.[a]

Sample	S_{BET} (m^2/g)	Elemental composition (%wt.) C	H	N	O	S	C/O
G	308	99.8	0.1	0.1	0.0	0.0	/
L-GO	0.8	63.7	0.6	0.1	33.7	1.9	1.9
H-GO	1.1	59.1	1.4	0.1	35	4.4	1.6

[a]Elemental composition of the anhydrous GO samples: water contents of nearly 20 %wt. and 5 %wt. are evaluated by TGA for H-GO and L-GO, respectively.

Results of the BET measurements, reported in **Table 1.2**, show that G exhibits a high surface area, *S*BET = 308 m^2/g, associated to its highly porous morphology, as shown in the SEM images in **Fig. 1.11**.

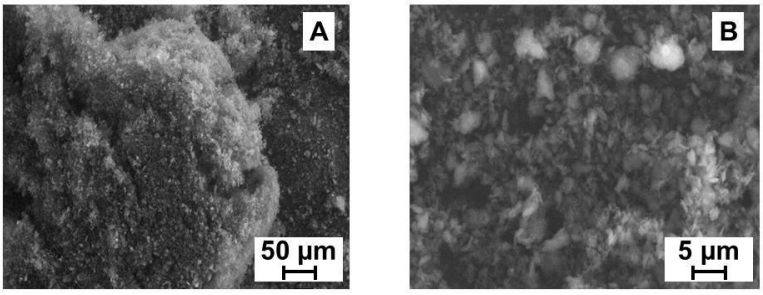

Figure 1.11 SEM images of G at different magnifications: (A) 50 µm and (B) 5 µm.

The oxidation of G definitely decreases its surface area from 308 m^2/g to 0.8 m^2/g for L-GO and 1.1 m^2/g for H-GO. These surface area values agree well with those reported in the literature for GO samples.**[30-32]**

1.4.2 Characterization of Graphite Oxide Samples

FTIR spectra in **Fig. 1.12** show the presence of oxygenated functional groups on the layers of both H-GO and L-GO, whose concentration is negligible in the starting graphite sample (G). Absorption bands of carboxyl groups (1730cm^{-1}), hydroxyl groups (stretching at 3420 cm^{-1} and bending at 1385 cm^{-1}) and epoxide groups (1145-1065 cm^{-1}) are observed.**[34]**

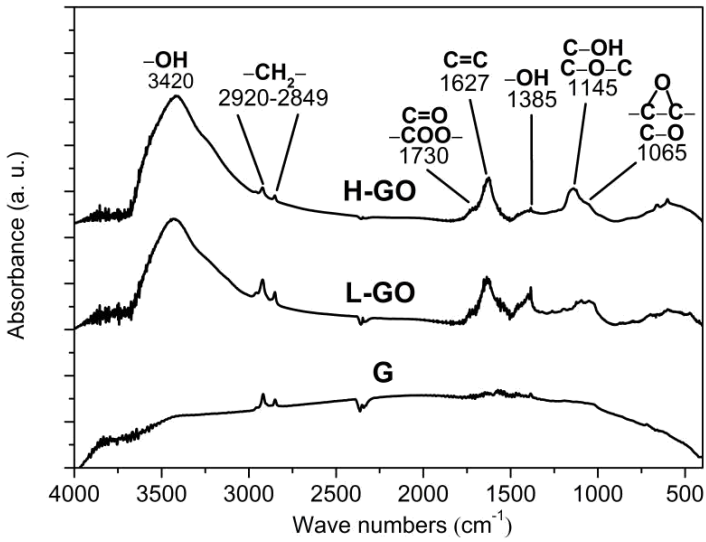

Figure 1.12. FTIR spectra in the range 4000−400 cm^{-1} of the starting high surface area graphite (G) and of the derived L-GO and H-GO.

The TGA curves in **Fig. 1.10** also confirm the presence of oxygenated functional groups, infact, both GO samples exhibit a weight loss from 150 °C to 300 °C, caused by the decarboxylation reactions and a weight loss above 300 °C, associated to the removal of hydroxyl and epoxide groups.**[33]**

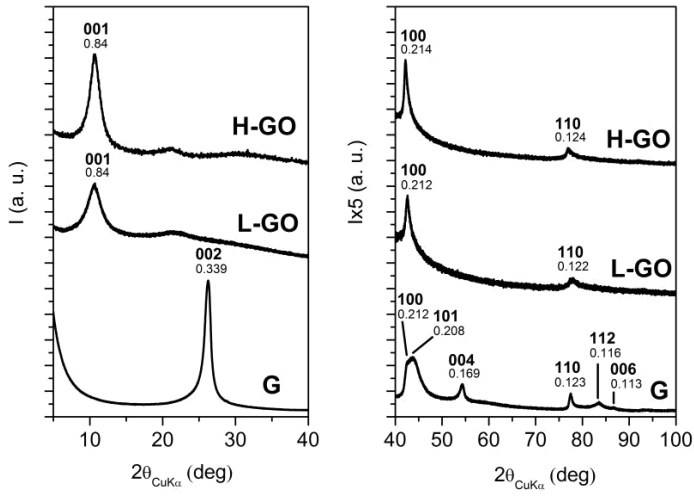

Fig. 1.13. X-ray diffraction patterns (Cu Kα) of the starting high surface area graphite (G) and of the derived L-GO and H-GO.

The X-ray diffraction patterns of GO samples in **Fig. 1.13** reveal a broad 001 reflection, corresponding to an interlayer distance of 0.84 nm, as already reported by some literature studies.**[35-38]** This value is higher than the interlayer distance observed in the starting graphite, about 0.339 nm. Hence, the oxidation of G produces an oxidized layered material with increased interlayer distance, from 0.339 nm to 0.84 nm, as represented in **Scheme 1.5**.

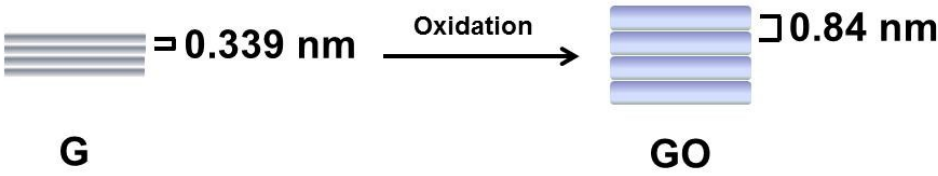

Scheme 1.5. Schematic representation of the increasing of the interlayer distance in GO after oxidation of graphite G.

The out-of-plane correlation lengths, determined by the Scherrer equation (see Chapter 6) were 5.4 nm for H-GO and 4.5 nm for L-GO. Correspondingly, the in-plane periodicities (*d*100 and *d*110) and correlation lengths ($D_{\parallel}$ = 30 nm) of both GO samples remain nearly unaltered with respect to the values observed in the starting graphite. Hence, GO layers present a long-range in-plane order as well as a high shape anisotropy of the crystallites ($D_{\parallel}$ / $D_{\perp}$ = 5.6 for H-GO and 6.7 for L-GO).

The pH back titration curves of GO samples dissolved in 0.05 M NaOH aqueous solution toward H^+ ion are given in **Fig. 1.14**.

Different inflection points, corresponding to distinctive acidic groups, such as carboxylic and phenolic groups, that form sodium salts in the presence of sodium hydroxide, are observed. The CEC values were evaluated as 7.3 mmol/g for H-GO and as 5.7 mmol/g for L-GO, when 17.8 mmol of H^+ and 19.3 mmol of H^+ were added to the well dispersed colloidal solutions of H-GO and L-GO, respectively.

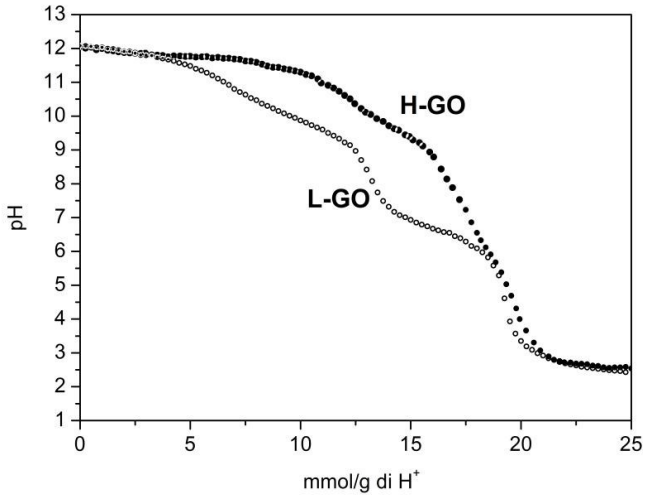

Figure 1.14. The pH back titration curve of L-GO (empty circles) and H-GO (filled circles) dissolved in 0.05 M NaOH aqueous solution toward H^+ ion.

In order to obtain graphitic fillers with improved compatibility with polymer matrices, the intercalation chemistry of GO with organic ions was

investigated. The method promotes a non-covalent functionalization of highly anisotropic GO layers and the results are discussed in the next paragraph.

1.4.3 Mechanical Exfoliation of Graphite Oxide

The mechanical exfoliation of GO by ball-milling is a simple but effective technique to produce exfoliated graphite oxide (eGO, also called graphene oxide) in the bulk state (see **Scheme 1.6**).

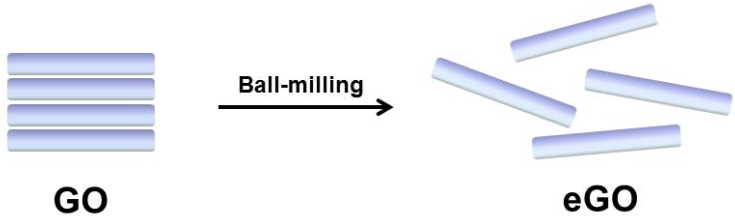

Scheme 1.6. Schematic representation of the exfoliation of GO by ball-milling.

The large increase of the interlayer spacing, from 0.34 nm up to nearly 0.8 nm, during the oxidation process of graphite and the disordered arrangement of the functional oxidized groups on the layer surfaces of GO lead to weak interlayer attractive forces, making easy the GO exfoliation by simple mechanical processes.
Exfoliated GO samples were prepared according the procedure in paragraph 5.6 , starting from L-GO, and the related X-ray diffraction patterns are shown in **Fig. 1.15**.

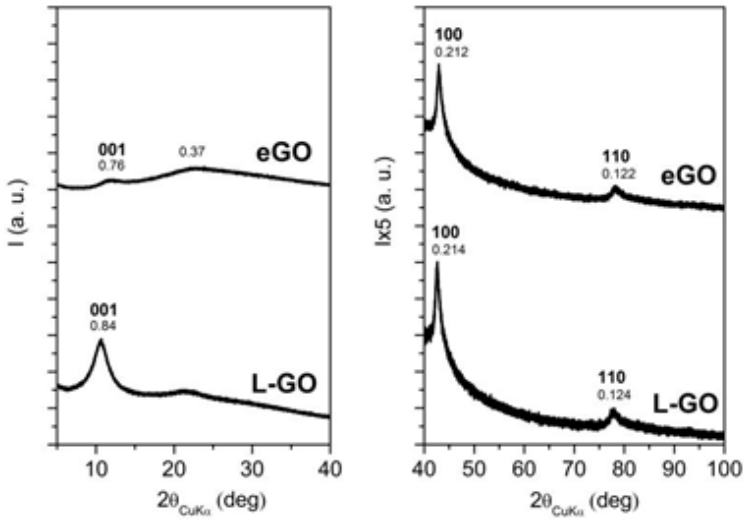

Figure 1.15. X-ray diffraction patterns (Cu Kα) of the starting graphite oxide (L-GO) and of the derived eGO after ball-milling.

The pattern of eGO shows, beside the maintenance of the 100 and 110 reflections, a very broad intense halo, centered at d = 0.37 nm with a correlation length of about 1 nm, indicating the presence of a large fraction of essentially exfoliated GO. The weak reflection with d = 0.76 nm and $D_{\perp} \approx$ 2.5 nm can be interpreted as the 001 reflection of unexfoliated GO, occurring in an amount lower than 10 %wt.

The bands of carboxyl, phenolic and epoxide groups in the FTIR spectrum of eGO appear enhanced in intensity with respect to the same bands in the L-GO FTIR spectrum in **Fig. 1.16**. This result could be attributed to the greater exposure of the oxygenated functional groups on the exfoliated layers of eGO.

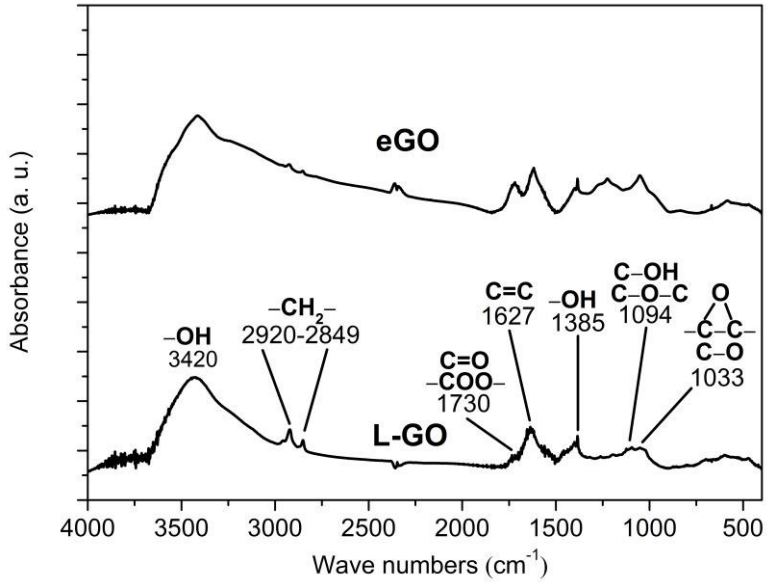

Figure 1.16. FTIR spectra of the starting graphite oxide (L-GO) and of the derived eGO after ball-milling.

Similar considerations can be made by comparing the TGA of L-GO and eGO in **Fig. 1.17**. In fact, above 150 °C, the oxygenated functional groups of eGO decompose earlier with respect to the same groups of L-GO, and, again, this phenomenon could be attributed to a greater exposure of the groups on the exfoliated layers of eGO.

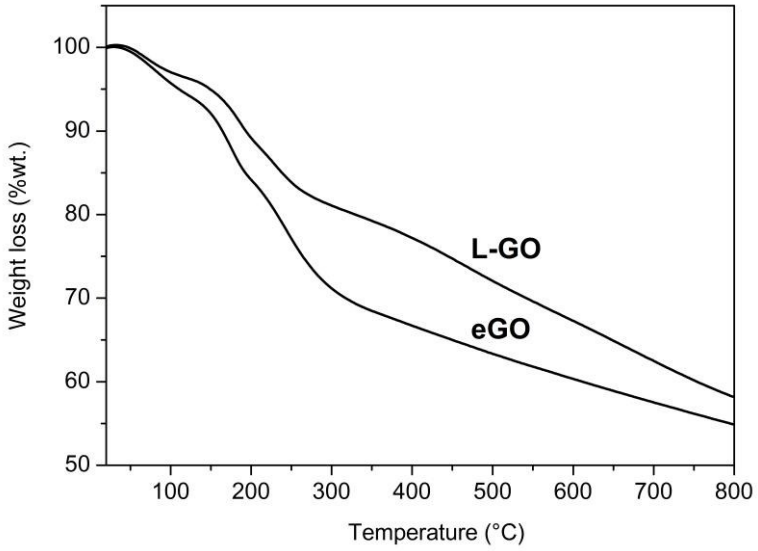

Figure 1.17. TGA curves in N_2 of the starting graphite oxide (L-GO) and of the derived eGO after ball-milling.

The results of the elemental analysis and the BET measurements, reported in **Table 1.5**, show that L-GO and eGO samples have similar C/O ratios and largely different surface areas, 0.8 m^2/g and 4.6 m^2/g, respectively, definitely lower than the value for G (308 m^2/g).

Table 1.5. Results of elemental analysis on the starting graphite oxide (L-GO) and of the derived eGO after ball-milling.[a]

Sample	S_{BET} (m^2/g)	Elemental composition (%wt.)					
		C	H	N	O	S	C/O
L-GO	0.8	63.7	0.6	0.1	33.7	1.9	1.9
eGO	4.2	66.1	0.5	0.1	31.4	1.9	2.1

[a]Elemental composition of the anhydrous samples: water contents of nearly 5 %wt. and 6 %wt. are evaluated by TGA for L-GO and eGO, respectively.

The SEM images of L-GO in **Figs 1.18A-B** indicate that the oxidation of G leads to dense aggregates of graphene oxide sheets (surface area largely decreases from 308 m^2/g to 0.8 m^2/g). The mechanical exfoliation of L-GO by ball-milling strongly reduced the dimension of the particles, providing sub-micrometric aggregates of thin crumpled graphene oxide sheets, stacked in a disordered manner (**Figs 1.18C-D**).**[39]**

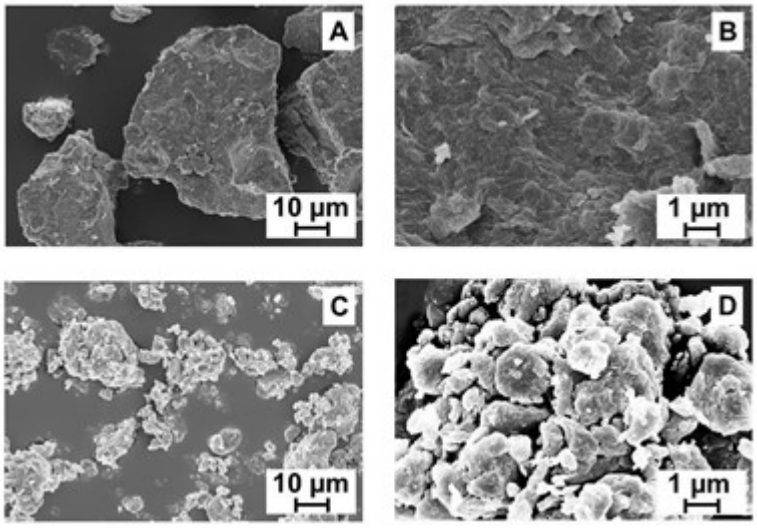

Figure 1.18. SEM images of: (A,B) L-GO and (C,D) eGO at different magnifications.

The high degree of exfoliation of eGO is also confirmed by the TEM images in **Fig. 1.19**. Particularly, in **Fig. 1.19B** single graphene oxide layers are clearly visible.

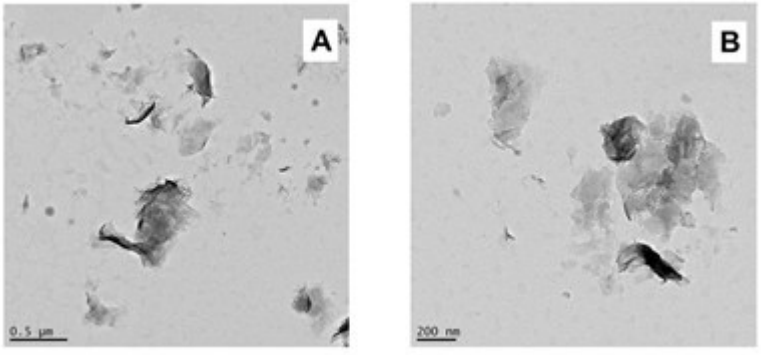

Fig. 1.19. TEM images of eGO at different magnifications: (A) 0.5 µm and (B) 200 nm.

References

[1] B. Kwiecińska, H. I. Petersen. *Int. J. Coal Geol.* **2004**, *57*, 99– 116.

[2] A. W. Hull. *Phys. Rev.* **1917**, *10*, 661–696.

[3] J. D. Bernal. *Proc. R. Soc. A* **1924**, *106*, 749–773.

[4] M. Inagaki and F. Kang, *Carbon Materials Science and Engineering: from Fundamentals to Applications*, Chapter 2, *36*,**2006**.

[5] B. E. Warren. *Phys. Rev.* **1941**, *59*, 693–698.

[6] Z. Q. Li, C. J. Lu, Z. P. Xia, Y. Zhou, Z. Luo. *Carbon* **2007**, *45*, 1686–1695

[7] A. Milev, M. Wilson, G. S. Kamali Kannangara, N. Tran. *Mater. Chem. Phys.* **2008**, *111*, 346–350.

[8] J. Zhao, L. Yang, F. Li, R. Yu, C. Jin. *Carbon* **2009**, *47*, 744– 751.

[9] O. J. Guentert. *J. Chem. Phys.* **1962**, *37*, 884–891.

[10] R. E. Franklin. *Acta Crystallogr.* **1950**, *3*, 107–121.

[11] P. J. F. Harris. *Interisciplinary Science Reviews* **2001**, *26*, 204–210.

[12] M. J. Wang, C. A. Gray, S. A. Reznek, K. Mahmud, Y. Kutsovsky, *Kirk-Othmer Encyclopedia of Chemical Technology*, **2003**.

[13] S. Lijima*. Nature* **1991**, 354, 56 – 58.

[14] M. Treacy, T. W. Ebbesen, J. M. Gibson. *Nature* **1996**, 381, *678–680*

[15] E. Flahaut, R. Bacsa, A. Peigney, C. Laurent. *ChemComm* **2003**, 12 1442–1443.

[16] Cumings, J.; Zettl, A. (2000). "Low-Friction Nanoscale Linear Bearing Realized from Multiwall Carbon Nanotubes".Science. 289 (5479): 602–604

[17] S. Babu, M. S. Seehr. *Carbon* **1996**, *34*, 1259–1265.

[18] O. J. Guentert, C. A. Klein. *Appl. Phys. Lett.* **1963**, *2*, 125–127

[19] C. N. Hooker, A. R. Ubbelohde, D. A. Young. *Proc. R. Soc. London A* **1965**, *284*, 17–31.

[20] A. Celzard, J. F. Marêché, G. Furdin, S. Puricelli. *J. Phys. D: Appl. Phys.* **2000**, *33*, 3094–3101.

[21] M. Cardinali, L. Valentini, J. M. Kenny. *J. Phys. Chem. C* **2011**, *115*, 16652–16656.

[22] H. Fujimoto. *Carbon* **2003**, *41*, 1585–1592.

[23] Lavoro J phys chem…Mauro et al 2013

[24] B. C. Brodie. *Philos. Trans. R. Soc. London* **1859**, *149*, 249–259.

[25] D. R. Dreyer, R. S. Ruoff, C. W. Bielawski. *Angew. Chem. Int. Ed.* **2010**, *49*, 9336–9344.

[26] H. He, J. Klinowski, M. Forster, A. Lerf. *Chem. Phys. Lett.* **1998**, *287*, 53–56.

[27] J. Luo, L. J. Cote, V. C. Tung, A. T. Tan, P. E. Goins, J. Wu, J. Huang. *J. Am. Chem. Soc.* **2010**, *132*, 17667–17669.

[28] D. R. Dreyer, C. W. Bielawski. *Adv. Funct. Mater.* **2012**, *12*, 3247–3253;

[29] A. D. Todd, C. W. Bielawski. *Catal. Sci. Technol*. **2013**, *3*,135–139; D. R. Dreyer, S. Murali, Y. Zhu, R. S. Ruoff, C. W. Bielawski. *J. Mater. Chem.* **2011**, *21*, 3443–3447.

[30] Y. Si, E. T. Samulski. *Nano Lett.* **2008**, *8*, 1679–1682.

[31] K. Haubner, J. Morawski, P. Olk, L. M. Eng, C. Ziegler, B. Adolphi, E. Jaehne. *ChemPhysChem* **2010**, *10*, 2131–2139.

[32] D. Chen, H. Zhu, T. Liu. *Appl. Mater. Interface* **2010**, *2*, 3702−3708.

[33] Z. J. Fan, W. Kai, J. Yan, T. Wie, L. J. Zhi, J. Feng, Y. M. Ren, L. P. Song, F. Wei. *ACS Nano* **2011**, *5*, 191−198.

[34] S. Zhang, Y. Shao, H. Liao, M. H. Engelhard, G. Yin, Y. Lin. *ACS Nano* **2011**, *5*, 1785−1791.

[35] J. Wang, X. Wang, C. Xu, M. Zhang, X. Shang. *Polym. Int.***2011**, *60*, 816−822.

[36] H. Kim, S. Kobayashi, M. A. AbdurRahim, M. J. Zhang, A. Khusainova, M. A. Hillmyer. *Polymer* **2011**, *52*, 1837−1846.

[37] S. Ansari, E. P. Giannelis. *J. Polym. Sci.: Part B* **2009**, *47*, 888−889.

[38] I. Y. Jeon, Y. R. Shin, G. J. Sohn, H. J. Choi, S. Y. Bae, J. Mahmood, S. M. Jung, J. M. Seo, M. J. Kim, D. W. Chang, L. Dai, J. B. Baek. *PNAS* **2012**, *109*, 5588–5593.

[39] M. Mauro, V. Cipolletti, M. Galimberti, P. Longo and G. Guerra. *J. Phys. Chem. C* **2012**, 116, 24809–24813.

Chapter 2

Experimental part:

Materials, Preparation Procedures and Characterization techniques

2.1 Preparation of GO with Higher Content of Oxygenated Groups

A 2000 mL three-neck round bottomed flask was flushed with gaseous N_2 and was then immersed into an ice bath.**[1]** 33 mL of nitric acid and 67 mL of sulfuric acid were fed to the flask under nitrogen and were then stirred obtaining a homogenous mixture. After introducing 5 g of graphite powder under vigorous agitation, 42 g of potassium chlorate was then added very slowly, to minimize the risk of explosion. The reaction mixture was stirred for 120 h at room temperature. The resulting dark green suspension was poured into a large amount of a 5 %wt. HCl aqueous solution. Centrifugation was then performed at 10000 rpm for 15 min using a Hermle Z 323 K centrifuge. The isolated GO powder was washed twice with 100 mL of a 5 %wt. HCl aqueous solution and subsequently with deionized water. Finally, it was dried at 60 °C for 12 h in an oven.

2.2 Preparation of GO with Lower Content of Oxygenated Groups

120 mL of sulfuric acid and 2.5 g of sodium nitrate were introduced into a 2000 mL three-neck round bottomed flask immersed into an ice bath and 5 g of graphite were added, under nitrogen, with a magnetic stirring.**[2]** After obtaining a uniform dispersion of graphite powder, 15 g of potassium permanganate were added very slowly to minimize the risk of explosion. The reaction mixture was thus heated to 35 °C and stirred for 24 h. The resulting dark green slurry was first poured into a copious amount of deionized water, and then centrifugated at 10000 rpm for 15 min with a Hermle Z323 K centrifuge. The isolated GO powder was washed twice with 100 mL of a 5 %wt. HCl aqueous solution and subsequently with deionized water. Finally, it was dried at 60 °C for 12 h in an oven.

2.3 Preparation of GOICs

Intercalates with 2HT, TPP and MUTP were prepared in analogy with the procedure reported by Matsuo et al. for graphite oxide intercalation

compounds with quaternary alkylammonium or alkylpyridinium ions, containing one long hydrocarbon chain.**[3]** GO powders (100 mg) were dispersed in 0.05 M NaOH solution (20 mL), 2HT (420 mg; 100% CEC), TPPBr or MUTPBr (260 mg; 308 mg 100% CEC) aqueous solutions (100 mL) was added in this dispersion and the reaction mixture was stirred at 40 °C for 12 h. The slurry was centrifugated at 10000 rpm for 15 min and the precipitate was washed with deionized water and dried at 60 °C for 12 h in an oven. 280 mg of GO/2HT, 140 mg of GO/TPP and 130 mg of GO/MUTP powders were obtained, without any loss of GO.
GO/2HT/SAES intercalates were also prepared by adding SAES (390 mg; corresponding to molar ratio 2HT/SAES = 1:1) alcoholic solution (100 mL ethanol) in the reaction mixture containing the GO dispersion and the 2HT aqueous solution, as reported above. 430 mg of GO/2HT/SAES powders were obtained, without any loss of GO.

2.4 Preparation of GO and GOIC films

Dispersions of GO in deionized water (5 mg/mL) and of GOIC in a mixture of cyclohexane (5 mg/mL) were subjected to sonication in 10 L batches bath ultrasound (Badelin Sonorex RK 1028 H) for 30 min. The dispersions were cast in a Petri dish at 50 °C and ~ 30 μm thick films were obtained.

2.5 Preparation of Chemically Reduced Graphite Oxide

GO powders were chemically reduced using hydrazine monohydrate as reducing agent.**[4]** 3g of GO were placed in a 4000 mL three-neck flask and then 3000 mL of deionized water were added, till the complete dispersion of the GO powders in water. 30 mL of hydrazine monohydrate were added to the GO dispersion and the mixture was allowed to react under agitation at 80 °C for 24 h. The CRGO powders slowly precipitated as a black solid. This product was, then, centrifugated, washed with deionized water (2x100 mL) and finally dried at 60 °C for 12 h in an oven.

Chemical reduction of GO was also performed using ascorbic acid.[6] 0.5 g of GO were placed in a 200 mL three-neck flask and then 50 mL of deionized water were added, till the complete dispersion of the GO powders in water. 0.5 g of ascorbic acid were added to the GO dispersion and the mixture was allowed to react under agitation at 100 °C for 24 h. The CRGO powders slowly precipitated as a black solid. This product was, then, centrifugated, washed with deionized water and finally dried at 60 °C for 12 h in an oven.

2.6 Graphite Oxide Exfoliation by Ball-Milling

GO powders were introduced in 125 mL ceramic jars (inner diameter of 75 mm) together with stainless steel balls (10 mm in diameter) and were dry-milled in a planetary ball mill (Retsch GmbH 5657 Haan) for 2 h with a milling speed of 500 rpm and a ball-to-powder mass ratio of 10 to 1.

2.7 GO paper preparation

GO and basified GO **[5-9]** aqueous dispersions were prepared from graphite oxide powders (150 mg) in 20 mL of water and of 0.05 M NaOH aqueous solution, respectively. Complete dispersions were obtained with the aid of ultrasonication35 for 4 h at room temperature.
Both kinds of dispersions were processed by vacuum filtration 20 as well as by casting in Petri dishes at 60 °C. By using these procedures GO and b-GO papers with thickness in the range 10–70 mm were obtained. All the results reported for GO paper refer to samples obtained by vacuum filtration, because the cast samples are too brittle. Most of the results reported for b-GO paper refer instead to cast samples, which present on the contrary improved flexibility b-GO papers were washed by water and, to remove Na^+ ions, also by a 0.05 M HCl solution.
Robust b-GO papers have been obtained by using aqueous solutions with a suitable range of NaOH concentration (0.01– 0.08 M).

2.8 Preparation of adducts of oxidized carbon black with ammonium ions with long alkyl chains

oCB/1HT and oCB/2HT adducts have been prepared starting from oCB samples with different O/C ratios. 200 mg of oCB powders were dispersed in 0.05 M NaOH solution (40 mL) and 100 mL of 1HT or 2HT aqueous solution (2mg/mL) was added in this dispersion and the reaction mixture was stirred at 60° C for 1 h. The black slurry was centrifuged at 10,000 rpm for 15 min and the precipitate was washed with deionized water and dried at 60° C for 12 h in an oven. From oCB samples with 0.16, 0.37, 0.58 and 0.83 O/C weight ratios, 250, 290, 330 and 365 mg of oCB/2HT adducts were obtained (without any loss of oCB), respectively. As for the oCB/1HT adduct, 275 mg were obtained, starting from the oCB sample with O/C=0.83.

Simple stoichiometric considerations show that, with oxidation level, the n_{cation}/n_C ratio largely change (from 0.005 up to 0.033) while the n_{cation}/n_O ratio remains essentially constant to 0.047+-0.005. This suggests that in the considered preparation conditions only 4-5% of the bound oxygen atoms leads to anion formation.

2.9 Oxidation of carbon blacks with different surface area

Oxidized Carbon Black samples (oCB) were prepared by Hummers' method **[2]**. About 6 g of all oCB samples were obtained. The obtained Oxygen/Carbon weight ratio is 0.71 for graphite oxide while is 0.16, 0.37, 0.58 and 0.83 for oCB as obtained from CB samples with surface areas of 33, 77, 125 and 151 m^2/g, respectively.

2.10 Wide Angle X-ray Diffraction

Wide-angle X-ray diffraction (WAXD) patterns were obtained by an automatic Bruker D8 Advance diffractometer, in reflection, at 35 kV and 40 mA, using the nickel filtered Cu–Kα radiation (1.5418 Å). The d-spacings

were calculated using Bragg's law and the observed integral breadths (β_{obs}) were determined by a fit with a Lorentzian function of the intensity corrected diffraction patterns, according to the procedure described by Iwashita et al.**[10]** The instrumental broadening (β_{inst}) was also determined by fitting of the Lorentzian function to line profiles of a standard silicon powder 325 mesh (99%). For each observed reflection, the corrected integral breadths were determined by subtracting the instrumental broadening of the closest silicon reflection
from the observed integral breadths, $\beta = \beta_{obs} - \beta_{inst}$. The correlation lengths (D) were determined using Scherrer's equation(1).

$$D_{hk} = \frac{K\lambda}{\beta_{hk} \cos\theta_{hk}}$$

(1)

Where λ is the wavelength of the incident X-rays and θ the diffraction angle, assuming the Scherrer constant K = 1.

Wide-angle X-ray diffraction measurements were also obtained by using a cylindrical camera (radius = 57.3 mm). The WAXD patterns of films of GO and GO compounds were recorded on a BAS-MS imaging plate (FUJIFILM) and processed with a digital imaging reader (FUJIBAS 1800). In particular, to recognize the kind of crystalline orientation present in films, photographic X-ray diffraction patterns were taken by placing the film sample parallel to the axis of the cylindrical camera and by sending the X-ray beam parallel (EDGE measure) to the film surface.

The degree of the different kinds of uniplanar orientation of the crystallites with respect to the film plane has been formalized on a quantitative numerical basis using Hermans' orientation functions, in analogy to that one defined for the axial orientation:

$$\frac{(\beta_{obs} - \beta_{inst})\cos\theta}{\lambda} = \frac{K}{D} \quad \frac{(2\sin\theta)}{\lambda}$$

(2)

by assuming $\overline{\cos \chi_{hkl}^2}$ as the squared average cosine value of the angle, xhkl, between the normal to the film surface and the normal to the hkl crystallographic plane.

Since, in our cases, a θhkl incidence of X-ray beam is used, the quantity $\overline{\cos \chi_{hkl}^2}$ can be easily experimentally evaluated:

$$\overline{\cos^2 x_{hkl}} = \overline{\cos^2 \chi_{hkl}} = \frac{\int_0^{\pi/2} I(\chi_{hkl}) \cos^2 \chi_{hkl} \sin \chi_{hkl} \, d\chi_{hkl}}{\int_0^{\pi/2} I(\chi_{hkl}) \sin \chi_{hkl} \, d\chi_{hkl}}$$

(3)

where I(χhkl) is the intensity distribution of a hkl diffraction on the Debye ring and χhkl is the azimuthal angle measured from the equator.

The diffracted intensities I(χhkl) of eq 3 were obtained by EDGE patterns, as collected by using a cylindrical camera, by the azimuthal profile at a constant 2θ value. Because the collection was performed at constant 2θ values and in the equatorial geometry, the Lorentz and polarization corrections were unnecessary.

In these assumptions, f hkl is equal to 1 and −0.5 if hkl planes of all crystallites are perfectly parallel and perpendicular to the plane of the film, respectively.

2.11 Fourier Trasform Infrared Spectroscopy

Fourier transform infrared spectra (FTIR) spectra in transmission mode with 2.0 cm-1 resolution, were recorded with a BRUKER Vertex70 spectrometer equipped with a deuterated triglycine sulfate (DTGS) detector and a KBr beam splitter. The powder specimens were diluted with

KBr of spectroscopic grade. The frequency scale was internally calibrated to 0.01 cm-1 with a He-Ne laser and the noise was reduced by signal averaging 32 scans.

2.12 Differential Scanning Calorimetry

The differential scanning calorimetry (DSC) was carried out under nitrogen in the suitable temperature range for each material at a heating or cooling rate of 10 °C/min on a TA instruments DSC 2920. Two heating and one cooling run were consecutively carried out in a cycle and the peak maxima were considered as the transition temperatures.

2.13 Thermogravimetric Analysis

Thermogravimetric analysis (TGA) of the layered nanofillers was carried out on a TG 209 F1, manufactured by Netzsch Geraetebau, from 20 to 800 °C, at a heating rate of 10 °C, under N2 flow. TGA curves were also obtained for scrambled rubber samples, Grubbs catalyst-functionalized graphene oxides and grafted rubbers to graphene oxide sheets from 20 to 1000 °C, at a heating rate of 10 °C, under air flow.

2.14 Elemental Analysis

Elemental analysis was performed with a Thermo FlashEA 1112 Series CHNS-O analyzer, after pretreating samples in an oven at 100 °C for 12 h, in order to remove the absorbed water.

2.15 BET Surface Area Measurements

Nitrogen adsorption at liquid nitrogen temperature (-196 °C) was used to measure surface areas of the samples with a Nova Quantachrome 4200e instrument. Before the adsorption measurement, clay and carbon-based powders were degassed at 100 °C under nitrogen flow overnight to remove

water, while polymeric aerogels were degassed at 40 °C, in the same conditions. The surface area values were determined by using 11-point Braunauer-Emmett-Teller (BET) analysis.**[11]**

2.16 Scanning Electron Microscopy

The morphology of the samples was characterized by means of a scanning electron microscope (SEM, Zeiss Evo50 equipped with an Oxford energy dispersive X-ray detector). Low energy was used (5 keV) to obtain the highest possible surface resolution. Before imaging, all specimens were coated with gold using a VCR high resolution indirect ion-beam sputtering system. The coating procedure was necessary to prevent surface charging during measurement and to increase the image resolution.

2.17 Trasmission Electron Microscopy

TEM analysis on rubber nanocomposites was performed by Dr. Lucia Conzatti at the CNR, Institute for Macomolecular Studies (ISMAC)-UOS Genova with a Zeiss EM 900 microscope applying an accelerating voltage of 80 kV. Ultrathin sections (about 50 nm thick) of cross-linked specimens were obtained by using a Leica EM FCS cryo-ultramicrotome equipped with a diamond knife (sample temperature: –130 °C). Before the TEM analysis, eGO samples were dispersed and sonicated in isopropanol, then 10 µL of the dispersion were were deposited on Assing copper grids coated with carbon film.

2.18 Back Titration of Graphite Oxides

The cation-exchange-capacity of the GO samples (CEC) was determined by the back titration of sodium hydroxide solution (0.05 M, 50 ml) of GO (100 mg) by 0.05 M hydrochloric acid solution, according to the procedure reported by Matsuo et al.**[12]**

References

[1] L. Staudenmaier. *Ber. Dtsch. Chem. Ges.* **1898**, 31, 1481–1487.

[2] W. S. Hummers, R. E. Offeman. *J. Am. Chem. Soc.* **1958**, 80, 1339.

[3] Y. Matsuo, T. Niwa, Y. Sugie. *Carbon* **1999**, 37, 897–901.

[4] S. Stankovich, D. A. Dikin, R. D. Piner, K. A. Kohlhaas, A. Kleinhammes, Y. Jia, Y. Wu, S. T. Nguyen, R. S. Ruoff. *Carbon* **2007**, 45, 1558–1565.

[5] X. Fan, W. Peng, Y. Li, X. Li, S. Wang, G. Zhang and F. Zhang. *Adv. Mater.* **2008**, 20, 4490–4493.

[6] D. Li, M. B. Miller, S. Giljie, R. B. Kaner and G. G. Wallace. *Nat. Nanotechnol.* **2008**, 3, 101–105.

[7] M. Mauro, M. Maggio, V. Cipolletti, M. Galimberti, P. Longo and G. Guerra. *Carbon* **2013**, 61, 395–403.

[8] C.-J. Kim, W. Khan and S.-Y. Park. *Chem. Phys. Lett.* **2011**, 511, 110–115.

[9] M. Mauro, M. Maggio, A. Antonelli, M. R. Acocella and G. Guerra. *Chem. Mater.* **2015**, 27, 1590–1596.

[10] N. Iwashita, C. R. Park, H. Fujimoto, M. Shiraishi, M. Inagaki. *Carbon* **2004**, *42*, 701–714.

[11] S. Brunauer, P. H. Emmett , E. Teller. *J. Am. Chem. Soc.*, **1938**, *60*, 309–319.

[12] Y. Matsuo, T. Miyabe, T. Fukutsuka, Y. Sugie. *Carbon* **2007**, *45*, 1005–1012.

Chapter 3

Intercalation Compounds of graphite oxide

A rich intercalation chemistry, both with organic ions, is possible, due to the strong layers hydrophilicity of graphite oxide, **[1-12].**

All known graphite oxide intercalation compounds (GOIC) present poor crystalline order, being generally limited to the distance between the graphite oxide layers, which can largely increase (also up to 5 nm) **[5]**.These intercalated structures and their limited order are rather similar to those observed for most clays with intercalated organic molecules (the so called organoclays) **[13-23]**.

In this work, we show the formation of GOIC exhibiting a long-range order in the organization of the guest species in the interlayer space as well as a large distance between graphite oxide sheets.

In particular, graphite oxide layers with a long-range in-plane order are ionically bonded with cations, which exhibit a hexagonal rotator order in the packing of their long hydrocarbon substituents. These ordered layered structures are obtained provided that the cations contain at least two long hydrocarbon tails. We also show that the intercalation of a second guest species, exhibiting one or two long hydrocarbon tails, not only leads to a further large increase of the interlayer spacing (from 3.4 nm up to nearly 5.8 nm, for guests with C18 alkyl chains) but also, surprisingly, improves the order in the stacking of the layers as well as in the organization of the hydrocarbon chains in the interlayer space.

3.1 Graphite Oxide Intercalation Compounds with long alkyl chains ammoniun cations

Graphite Oxide intercalates with dimethyl ditalloyl ammonium (2HT) and with 2-stearamidoethyl stearate (SAES) (**Fig. 3.1**) were prepared in analogy with the procedure reported by Matsuo et al. for graphite oxide intercalation compounds with quaternary ions, containing one long hydrocarbon chain **[23],** by adding a basified GO dispersion to an aqueous solution of the ammonium ions.

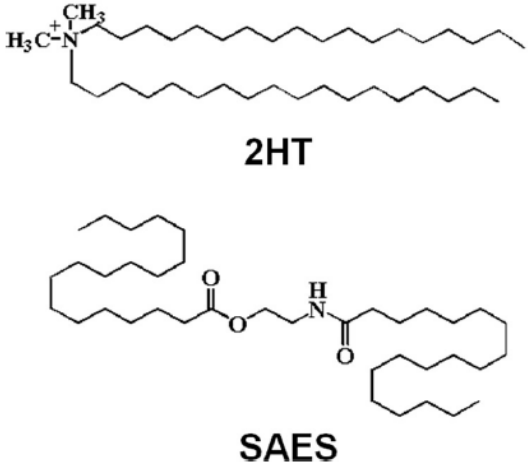

Figure 3.1. Molecular structures of ionic and polar compounds intercalated with GO: dimethyl ditalloyl ammonium (2HT),2-stearamidoethyl stearate (SAES).

Measurements of the water loss by TGA and elemental analysis of the desiccated GO powders indicate that the GO composition is $O_{0.47}H_{0.2}\cdot 0.28H_2O$. On the basis of the guest weight uptake and measurements of the water loss by TGA, the composition of GO/2HT and GO/2HT/SAES intercalates has been evaluated as $CO_{0.47}H_{0.2}\cdot(C_{36}H_{76}N)_{0.059}\cdot 0.15H_2O$and $CO_{0.47}H_{0.2}\cdot(C_{36}H_{76}N)_{0.059}\cdot(C_{38}H_{75}O_3N)_{0.057}\cdot$0.15H2O, respectively. The content of 2HT guest ions in GO/2HT intercalates was 3.0 mmol/g GO, i.e. less than one half of the maximum possible uptake, as calculated on the basis of the cation exchange capacity. The content of the second polar guest (SAES) in GO/2HT/SAES intercalates was 2.9 mmol/g GO, with a 2HT/SAES molar ratio not far from 1/1. The above reported compositions correspond to a molar ratio between carbon in the graphite oxide layers and alkyl chains of the intercalated guest species (CGO/chains) of roughly 8/1 and 4/1, in GO/2HT and GO/2HT/SAES intercalates, respectively.

3.2.1 Characterization of graphite intercalation compounds with ammonium cations

The X-ray diffraction pattern of a graphite oxide powder, as obtained by oxidation of graphite samples exhibiting high shape anisotropy **[24-25]**, shows a broad 001 peak corresponding to an interlayer distance of 0.84 nm, with a correlation length of 5.4 nm (**Fig. 3.2A**). The pattern of **Fig. 3.2A** also shows narrow 100 and 110 peaks corresponding to a long-range order in the graphitic planes (correlation length perpendicular to the 100 planes higher than 30 nm). The X-ray diffraction pattern of a GOIC with ionically bonded di(hydrogenated tallow)-dimethylammonium (2HT) is shown in **Fig. 3.2B**. This GOIC was prepared by first dispersing GO powder in a aqueous solution of NaOH and by a further treatment with an aqueous solution of dimethyl ditalloyl ammonium chloride (2HTCl).

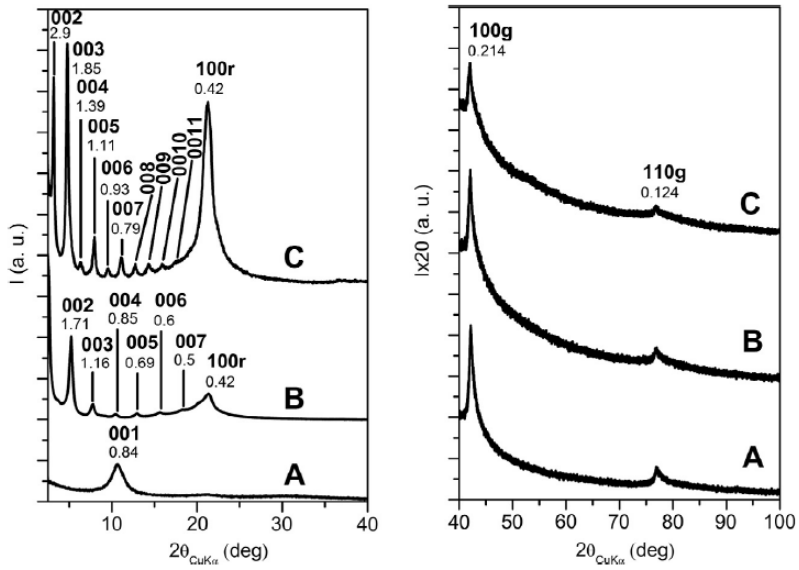

Figure 3.2. X-ray diffraction patterns (CuKa) of the starting graphite oxide (A) and of the derived GOIC, which includes the 2HT cation with two long hydrocarbon chains (B) or 2HT and SAES (C). The symbols g and r indicate reflections relative to the graphite oxide planes and to the hexagonal rotator order, respectively.

The pattern shows essentially unaltered 100 and 110 reflections, clearly indicating the maintenance of the in-plane graphite oxide order. Moreover, many narrow 00ℓ reflections (with ‘ up to 8) appear, which correspond to a spacing between graphite oxide layers of 3.4 nm with a correlation length increased up to 14 nm. The pattern of **Fig. 3.2B** also presents a reflection at d = 0.42 nm, which suggests the occurrence of a hexagonal rotator order **[26-31]** of the long hydrocarbon chains of the intercalated ammonium salt. The broadness of this reflection indicates a correlation length of this hexagonal rotator order in the interlayer space, in directions parallel to the graphite oxide layers, close to 7 nm.

Surprisingly, the crystalline order of the obtained GOIC with 2HT can be largely increased by adding a second guest species. In particular, by adding polar molecules including long hydrocarbon chains, like e.g. 2-stearamidoethyl stearate (SAES) or stearic acid (SA), the in-plane graphite oxide order is maintained while all the other above described kinds of

order are improved. For instance, the X-ray diffraction pattern of the GO sample of Fig. **3.2A**, after treatment with 2HT and SAES, is reported in Fig. **3.2C**. In this pattern, at least eleven 00ℓ reflections are present with an increased correlation length (D = 42 nm) and with a largely increased spacing (d = 5.8 nm). The intense and narrow diffraction peak at d = 0.42 nm, typical of hexagonal arrangements of long n-alkanes **[26-31],** indicates an increase of the correlation length for the hexagonal rotator order (in the direction parallel to the graphite oxide layers) from 7 nm up to 10 nm, as a consequence of the addition of a second polar guest. These GOIC with rotator order in the intercalated layers, lead to polycrystalline films exhibiting macroscopic orientational order, by simple casting procedures. For instance, X-ray diffraction patterns of films having a thickness of nearly 30 μm, as obtained by casting from aqueous suspensions of GO and of the derived GO/2HT/SAES intercalate, are shown in Fig. 3A and B, respectively. In particular, the EDGE patterns, i.e. photographic patterns taken with X-ray beam parallel to the film surface, present intense (00ℓ) reflections on the equatorial line (corresponding to the already described interlayer distances of 0.84 nm and 5.8 nm for GO and GO/2HT/SAES in **Fig. 3.3A** and **B**, respectively).

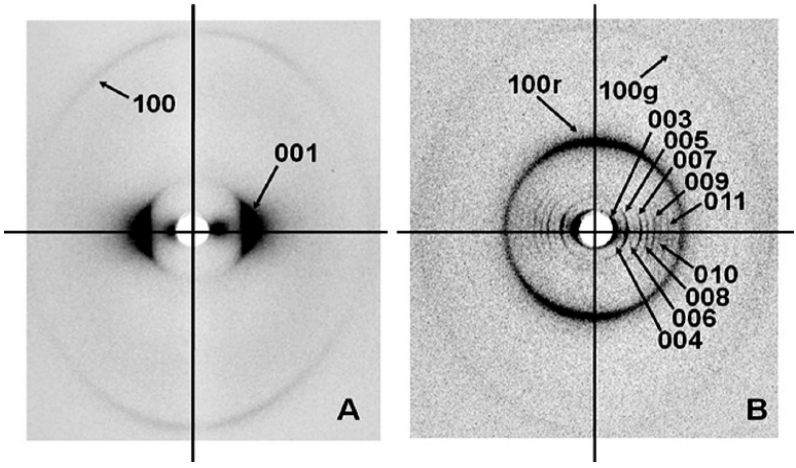

Figure 3.3. Photographic X-ray diffraction patterns (CuKa) of films cast from aqueous suspensions of graphite oxide (A) and of the derived GOIC with 2HT and SAES (B), as collected with the X-ray beam parallel to the film (EDGE patterns). The hkl Miller indexes of the main reflections are indicated and the symbols g and r discriminate 100 reflections relative to the graphite oxide planes and to the rotator order, respectively.

As already described for GO **[20]**, these diffraction data can be rationalized by the orientation of the graphite oxide layers preferentially parallel to the film plane. By using the procedure described in Chapter 6 , a degree of parallelism of this plane with respect to the film surface has been evaluated as f00l =0.85. As for the reflection at d = 0.42 nm in **Fig. 3.3B**, its polarization along the meridian of the EDGE pattern is in agreement with the assignment as
100 reflection of a hydrocarbon rotator order, nearly perpendicular to the graphite oxide layers. Analogous results have been obtained for the GO/2HT intercalate.

3.2.2 Structural reversibility of the graphite oxide intercalation compounds with temperature

The presence of an hexagonal rotator order is clearly confirmed by combined differential scanning calorimetry (DSC) and WAXD

measurements. For both GOIC of **Fig. 3.2B** and C, the DSC scans show an irreversible first heating followed by reversible cooling and heating scans. For instance, for the GOIC with 2HT (**Fig. 3.4B**), the first heating scan shows an intense endothermic peak located at 42°C, while the subsequent cooling and heating scans present exothermic and endothermic peaks at 25°C and at 35°C, respectively (**Fig. 3.4A**).

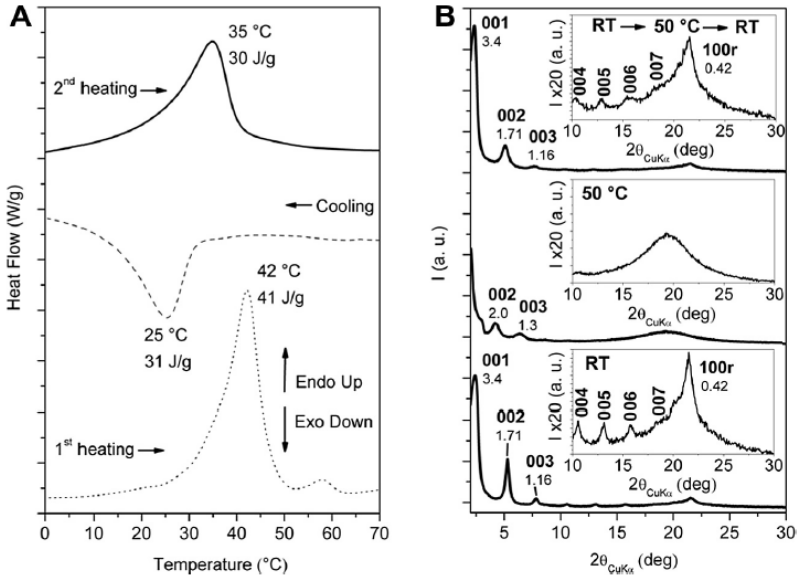

Figure 3.4. DSC scans of the GOIC with 2HT: (dotted) first heating scan; (dashed) cooling scan; (continuous) 2nd heating scan. (B) WAXD at RT, 50°C and at RT after thermal treatments up to 100°C.

The WAXD patterns of the GO/2HT powder at room temperature, at 50°C and at room temperature after treatment at 50°C, have been reported in **Fig. 3.4B**. The pattern at 50°C shows that the endothermic phenomena of **Fig. 3.4A** lead to the disappearance of the diffraction peak at d = 0.42 nm and hence to the loss of the rotator order. Moreover, the pattern at 50°C shows shifts of the 00ℓ reflections, indicating an increase of the interlayer spacing from 3.4 nm to 4.0 nm. The pattern at room temperature of the

GOIC, after annealing at 50°C, shows a renewed reflection at d = 0.42 nm as well as 00ℓ peaks corresponding to the former narrower periodicity (3.4 nm). This demonstrates, as already observed for other layered materials intercalated with long hydrocarbon chain molecules**[31]**, that both loss of hexagonal rotator order and increase of the interlayer spacing are thermally reversible. An analogous behavior has been observed for the GO/2HT/SAES intercalate, with main crystallization and melting peaks of the rotator phase being located at 88°C and 82°C, respectively.

3.2.3 Structure of the graphite oxide intercalation Compounds

The X-ray diffraction pattern of the GOIC of Fig. 2B presents a high similarity with those of ordered intercalate structures obtained by self-assembling of stearate ions in layered double hydrotalcite clay (LDH), in which C18 chains form bilayer structure in the vertical direction and a distorted hexagonal structure in the lateral direction, within the LDH interlayer space.**[32]**

For the GOIC of Fig. 2B, an analogous structure with inclined bilayers is here suggested (**Fig. 3.5A** and **B**). The tilt angle of these inclined bilayers can be evaluated as a = 60°, on the basis of the basal spacing (d001 = 3.4 nm), by assuming that the thickness of the graphite oxide layer is close to 0.8 nm **[1]** , and that the length of two fully extended 2HT cations is 5.0 nm.

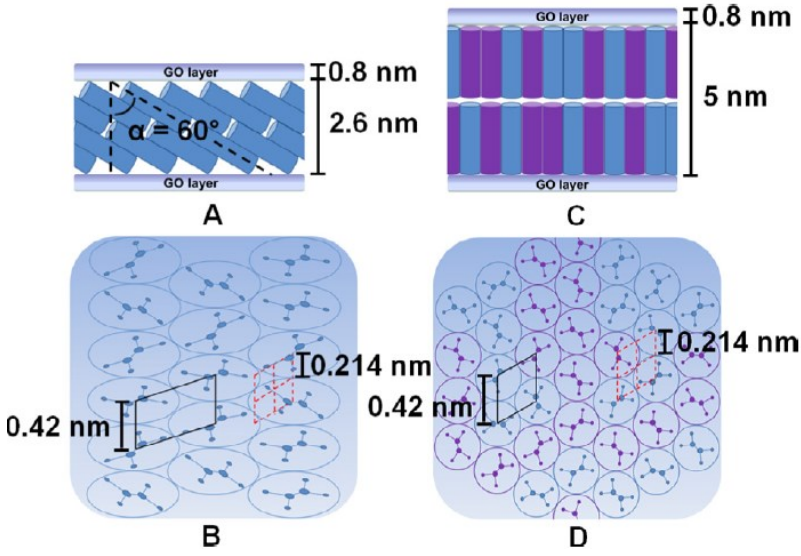

Figure 3.5. Schematic presentation of the crystalline structures of the GOIC with the ammonium ion 2HT (A and B) or within additional polar guests with C18 hydrocarbon tails (C and D). The cylinders of the lateral views (A and C) indicate hydrocarbon tails of the ammonium cation (blue) or of the additional polar guest (purple). For the top views (B and D), ellipses and circles indicate hydrocarbon chains inclined and perpendicular to the graphite oxide layers, respectively. Moreover, dashed red lines show four adjacent hexagonal cells of GO while thick black lines show the hexagonal rotator cell (in D) and the corresponding pseudo-cell on a section parallel to the GO layers (in B). The definition of the alkyl chains tilt angle a is shown in A.

For a = 60°, the surface occupied by eight graphite oxide unit cells (four are indicated as dashed red lines in **Fig. 3.5B**) is nearly equal to the surface occupied by a pseudo-cell of the rotator order, being parallel to the GO planes (indicated as thick black lines in **Fig. 3.5B**). Hence, the intercalate GO/2HT exhibits a CGO/chains molar ratio of nearly 8/1, in good agreement with the molar ratio as independently evaluated by gravimetric measurements. As for the more ordered GOIC of **Fig. 3.5C** including both 2HT and SAES guests, on the basis of the large interlayer spacing (5.8 nm), analogous to those observed for cationic clays intercalated with

ammonium salts with C18 tails (6 nm) [43], a structure with perpendicular bilayers can be suggested. In fact, the observed basal spacing is equal to the sum of the periodicity of GO (≈0.8 nm) **[24-30]** and of the length of two fully extended 2HT cations (≈5.0 nm) **[40]**. It is also worth adding that the patterns of **Fig. 3.2C** and **Fig. 3.3B** present a clear odd–even effect for the 00ℓ reflections, with definitely more intense odd reflections. This phenomenon can be easily rationalized on the basis of the model with perpendicular alkyl chains (**Fig. 3.5C**). In fact, this model presents a minimum of atomic density in the middle of the graphitic interlayer space, due to non-bonded interactions between the tails of the long hydrocarbon chains, being clearly consistent with the reduced intensity of the 00ℓ reflections for ‘ even.

The basal planes of the hexagonal cells of the rotator order (a_r = 0.42 nm, thick black lines), and of GO (a_g = 0.214 nm, dashed red lines) are compared in **Fig. 3.5D**. A good fit between the two hexagonal cells, with $a_r = 2a_g$ corresponding to four hexagonal cells of GO per one hexagonal cell of the rotator order, is apparent and clearly indicates a molar ratio of CGO/chains = 4/1. Again, the intercalate composition as derived by structural considerations well agrees with the composition as derived by gravimetric guest uptake.

It is worth adding that the observed long range hexagonal rotator order of GOIC of **Fig. 3.2C** (D_{100r}=10 nm) is possibly associated with this good fit between the hexagonal cell bases of GO and of the hydrocarbon rotator order. The two structures of **Fig. 3.5** are also validated by density considerations. In fact, an evaluation of the density in the interlayer space provides a similar density for both intercalates (0.98 g/cm^3) not far from the value observed for crystalline polyethylene.

3.3 Graphite Oxide Intercalation and Exfoliation compounds with Phosphonium ions.

Quaternary phosphonium salts constitute a new generation of efficient, broad-spectrum, low-toxicity antiseptic, which has been proposed as active compound for antibacterial materials. **[33-34]** Antibacterial materials based on quaternary phosphonium salts, carried by clay minerals, have shown long-acting antibacterial activity.**[35-36]** However, their application is strongly limited by their bad dispersion in water.**[37-38]** This problem has been overcome by preparation of phosphonium salt composites with graphite oxide (GO),**[39]** which can lead to GO/ion compounds. **[40]** In fact, it is well-known that the treatment of graphite with strong mineral acids and oxidizing agents leads to graphite oxide (Hummers' and Studenmaier's methods) whose layers exhibit a strong hydrophilicity and also a rich intercalation chemistry with organic ions. **[41-48]** In particular, the structural organization of compounds of GO with organic ions can largely vary between regularly intercalated crystalline **[41-47]** to fully exfoliated amorphous.**[49-50]**

To achieve a control of the release rate of ions in aqueous media for these new antibacterial materials, a precise control of the molecular and crystalline organization of the GO/phosphonium compounds is required. In this work, procedures that are suitable to produce highly ordered graphite oxide intercalation compounds (GOIC) or fully disordered graphite oxide exfoliated compounds (GOEC), are reported. These limit intercalated and exfoliated compounds are structurally characterized, and their largely different ion release behaviors in neutral and acid aqueous solutions are compared.

3.3.1 Intercalation compounds with quaternary phosphonium ions

Graphite oxide intercalation compounds with phosphonium ions are prepared in analogy with the procedure reported by Matsuo et al. for graphite oxide intercalation compounds with quaternary alkylammonium

ions. The molecular structures of the two phosphonium ionic compounds used in this work, are reported in **Fig. 3.6.**

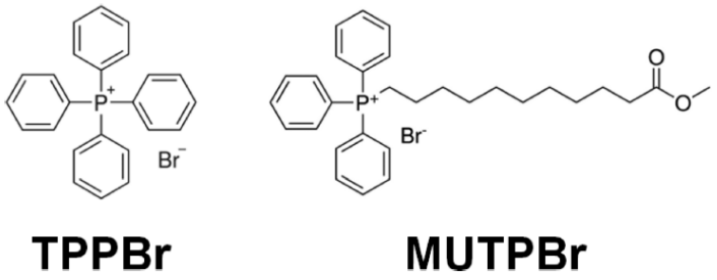

Figure 3.6. Molecular Structures of Tetraphenylphosphonium Bromide(TPPBr) and 11-Methoxy-11-oxo-undecyltriphenylphosphonium Bromide (MUTPBr).

The X-ray diffraction patterns of GOIC with ionically bonded TPP^+ and $MUTP^+$ are shown in **Fig. 3.7B,C**, respectively. Both patterns show 100 and 110 reflections, clearly indicating the maintenance of in-plane graphite oxide order. In particular, these reflections and hence the in-plane graphitic order remain unaltered after transformation of GO in GOIC compound with TPP+ (**Fig. 3.7A,B**). Moreover, few 00l reflections (with l up to 3) appear, which correspond to increases of spacing between graphite oxide layers from 0.84 nm up to 1.40 and 1.34 nm, as a consequence of intercalation of TPP^+ and $MUTP^+$, respectively. The correlation length perpendicular to the graphitic layers, as evaluated from the 001 reflection, increases from 5.4 nm up 12 and 8 nm for GOIC with $MUTP^+$ and TPP^+, respectively.

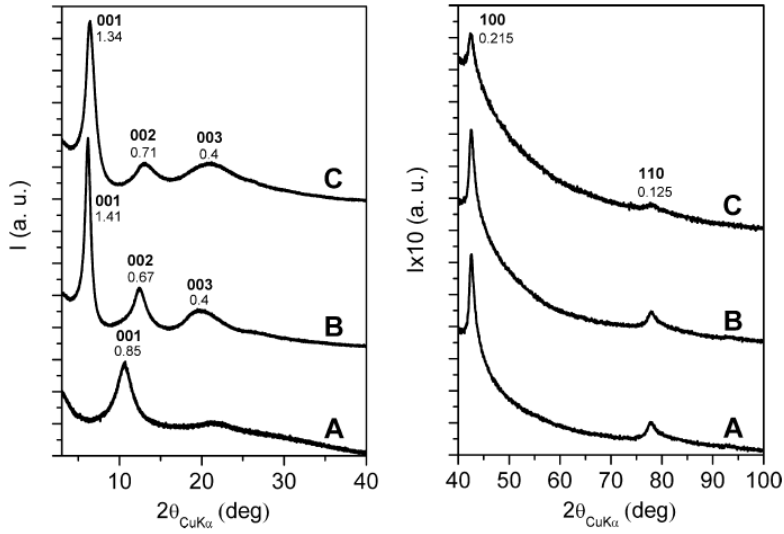

Figure 3.7. X-ray diffraction patterns (CuKα) of the starting graphite oxide (A) and of the derived GOICs including phosphonium ions: TPP+ (B) or MUTP+ (C).

Differently from some recently described intercalates with ammonium ions of GO **[41]**,**[51]** and clays,**[52]** GOIC with $MUTP^+$ does not show additional order in the packing of its long hydrocarbon chains. The whole information from the X-ray diffraction patterns of **Fig. 3.7** indicates that similar crystalline structures are obtained for both GOICs, with a higher structural order for the compound including the symmetric TPP+ ion. These GOICs, by simple casting procedures, lead to polycrystalline films exhibiting macroscopic orientational order. For instance, X-ray diffraction patterns of films having a thickness of nearly 50 μm, as obtained by casting from aqueous suspensions of GO and of the derived GOIC with TPP+, are shown in **Fig. 3.8A,B**, respectively. In particular, the EDGE patterns, i.e., photographic patterns taken with X-ray beam parallel to the film surface, present intense (00ℓ) reflections on the equatorial line, corresponding to the interlayer distances of 0.84 and 1.4 nm for GO and GOICs with TPP+, in agreement with the powder diffraction patterns of **Fig. 3.7A,B**, respectively. However, the THROUGH patterns, i.e., photographic patterns taken with X-ray beam perpendicular to the film surface (not shown), present uniform Debye rings, being intense for the in-plane 100 reflections.

As already described for GOIC with quaternary ammonium ions, **[53]** these diffraction data can be rationalized by the orientation of the graphite oxide layers preferentially parallel to the film plane. By using the procedure described in the experimental section, a degree of parallelism of this plane with respect to the film surface has been evaluated as $f_{00\ell} \approx 0.85$ for both GO and GOIC with TPP^+.

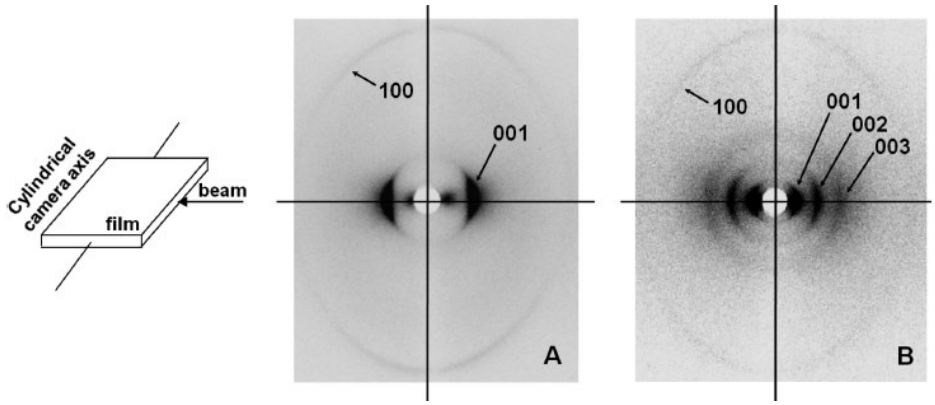

Figure 3.8. Photographic X-ray diffraction patterns (CuKα) of films cast from aqueous suspensions of graphite oxide (A) and of the derived GOIC with TPP+ (B). The patterns have been collected with the X-ray beam parallel to the film. The hkl Miller indexes of the main reflections are indicated.

3.3.2 Exfoliation compounds with quaternary phosphonium ions

The X-ray diffraction pattern of the GO as basified by the treatment with NaOH solution is shown in **Fig. 3.9A**. It is clearly apparent that the 001 peak of GO is replaced by a broad halo centered at d = 0.37 nm, clearly indicating loss of order perpendicular to the graphite oxide layers. However, the maintenance of the 100 and 110 peaks indicates maintenance of the in-plane GO order and hence formation of exfoliated GO layers.

The X-ray diffraction patterns of the compound of exfoliated GO with ionically bonded TPP^+ and $MUTP^+$ are shown in **Fig. 3.9B,C**, respectively. Both patterns are dominated by maintenance of the 100 and 110 GO peaks as well as by the maintenance of a broad amorphous halo of the exfoliated GO (**3.9A**), whose maximum is shifted from d = 0.37 nm to d ≈ 0.4 nm. For both patterns a broad amorphous halo appears below 2θ ≈ 8°, which could be possibly attributed to a minor amount (<10%) of GOIC crystallites with very small correlation length perpendicular to the GO layers.

It is worth adding that GO compounds with phosphonium ions present a crystalline order perpendicular to the GO layers being intermediate between those of the presently reported GOIC and GOEC samples.

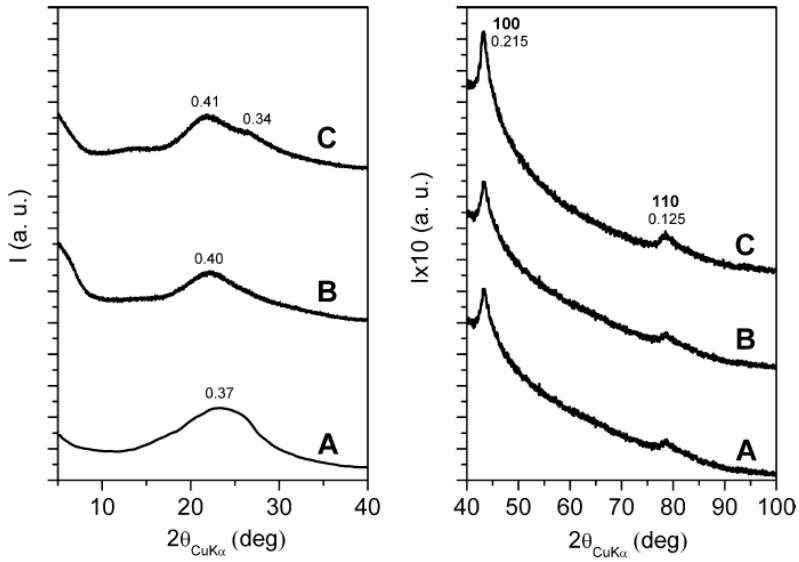

Figure 3.9. X-ray diffraction patterns (CuKα) of the exfoliated GO, as obtained by basification (A), and of the exfoliated compounds with phosphonium ions: TPP^+ (B) or $MUTP^+$ (C).

3.3.3 Structural Organization of GOIC and GOEC Compounds with TPP^+.

Elemental analysis of the desiccated GO powders and measurements of the water loss by TGA allow to evaluate the GO composition as $CO_{0.39}H_{0.12}{\cdot}0.05H_2O$. Measurements of the guest weight uptake allow to establish that the amount of TPP+ in both GOIC and GOEC is not far from 30 %wt. This value is much lower than the maximum possible uptake, as calculated on the basis of the GO cation exchange capacity (72 %wt). The X-ray diffraction data of **Fig. 3.7** indicates that GOIC compounds with both considered phosphonium ions exhibit a crystal structure with long-range order only parallel and perpendicular to the GO layers. In particular, the periodicity between the graphite oxide layers is close to 1.4 nm (**Fig. 3.7B**), while a long-range order is maintained in the graphite oxide layers.

There is no evidence of order in the arrangement of the phosphonium ions in the interlayer space, which are present in an amount close to one ion per 18 graphitic carbons. Of course, in the interlayer space, beside the phosphonium salt and water, also Na+ ions are present in an amount that, on the basis of the evaluated CEC, subtracted by the amount of exchanged phosphonium ions, is roughly equal to 11%wt and corresponding to one Na^+ ion per three graphitic carbons.

The crystalline structure of GOIC with TPP^+ of **Fig. 3.7B** presents a density value, calculated on the basis of the interlayer distance and elemental analyses, close to 1.9 g/cm^3, i.e., intermediate between the densities of the corresponding GO (1.6 g/cm^3) and of the starting graphite (2.3 g/cm^3).

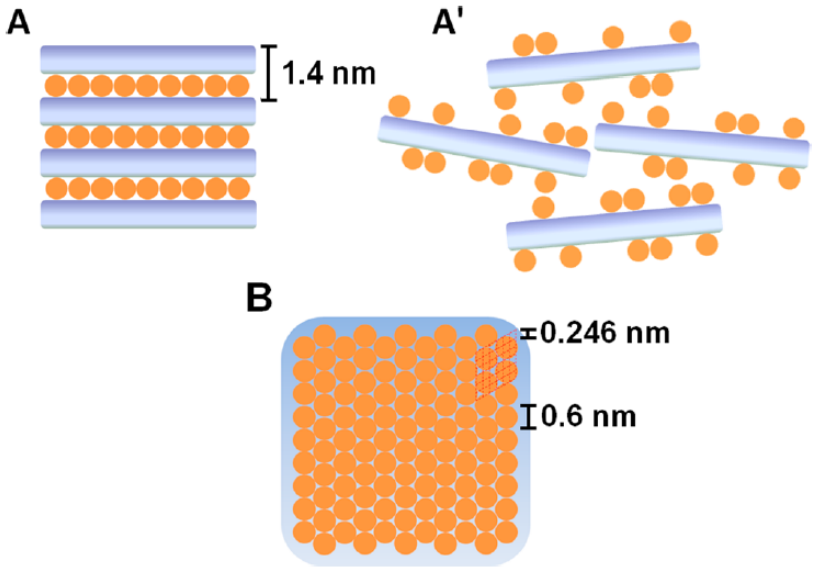

Figure 3.10. Schematic presentation of the crystalline structure of GOIC with TPP+ (ions shown as spheres): (A) lateral view, showing the distance between graphite oxide layers; (B) top view, showing the average presence of one TPP+ ion per nine graphitic unit cells (18 carbons). Schematic presentation of the exfoliated structure of GOEC with TPP+ (A').

This density value is, however, definitely higher than the values calculated for the crystalline structures of GOIC with ammonium ions that exhibit long hydrocarbon tails (in the range 1.0−1.1 g/cm3).

A schematic representation of the exfoliated compound with TPP+ is shown in **Fig. 3.10A'**. The scheme shows that GO layers with ionically bound phosphonium ions maintain only the in-plane order of the graphitic carbons.

3.3.4 Spectroscopic characterization of GOIC and GOEC Compounds with TPP+.

The FTIR spectra, in the range 2000−400 cm^{-1}, of GOIC and GOEC compounds with TPP+ have been compared with those of GO and TPPBr in **Fig. 3.11**. The spectra show that many vibrational peaks of TPP+ are clearly apparent both for GOIC and GOEC. In particular, a closer look to the peak positions shows that most peaks are significantly red-shifted and that these shifts are definitely higher for GOEC compound. For instance, the peak at 1485 cm^{-1} is shifted 3 cm^{-1} for GOIC and 11 cm^{-1} for GOEC, while the peak at 694 cm^{-1} is shifted 6 cm^{-1} for GOIC and 10 cm^{-1} for GOEC. These shifts are possibly due to the reduced confinement of TPP+ in the GO compounds, with respect to TPPBr, which of course is strongly reduced for the exfoliated compound. Also interesting are changes in the spectral region 1800−1500 cm^{-1} that includes some relevant vibrations of GO. In fact, the intense C・C stretching peak at 1633 cm^{-1} is shifted down to 1625 cm^{-1} for GOIC. These data confirm the formation of GO compounds with TPP^{+}.

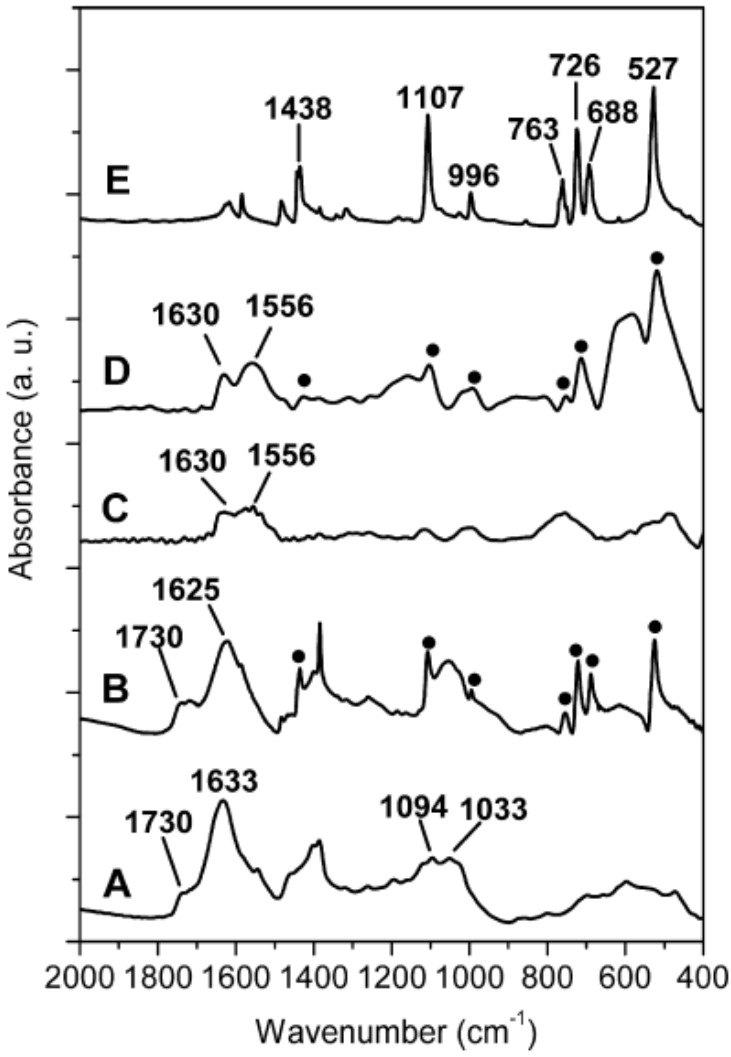

Figure 3.11. FTIR spectra of the starting graphite oxide (A), GOIC with TPP+ (B), exfoliated GO (C), GOEC with TPP+ (D), and TPPBr (E). Filled circles indicate the peaks of TPP+ in GOIC and GOEC samples.

3.3.5 Release of Organo-Phosphonium Ions in Aqueous Solutions from GOIC and GOEC

The obtained GOIC and GOEC with TPP+ have been compared as for their kinetics of release of the ionic antibacterial agent in aqueous solutions.
In particular, we have considered neutral (pH = 7 with 10 wt% of NaCl) and acid (pH = 1.3, HCl 0.05 M) solutions with pH similar to those of human stomach and colon, respectively. The amount of TPP^+, as released from GOIC (red curves) and GOEC (blue curves) in a neutral (circles) or in an acid (triangles) solution, is plotted versus soaking time in **Fig 3.12A**. These amounts have been evaluated by UV measurements in the spectral range 250−350 nm on the aqueous solutions. In particular, the UV spectra as obtained after the soaking time of 82 h are compared in **Fig 3.12C**. The data of Figure 6A clearly show that the release of the TPP+ ions in the aqueous acid solution is complete both for GOIC (∼33 wt %) and GOEC (∼27 wt %), after 70−80 h. In the neutral saline solution, the ion release is only partial but still high from GOEC (∼12 wt %, after 82 h, i.e., nearly 44 wt % of the TPP+ content) while poor for GOIC (∼4 wt %, i.e., nearly 12 wt % of the TPP^+ content). In the latter case, an equilibrium release value is reached after nearly 70 h.
These desorption data can be rationalized on the basis of X-ray diffraction characterization of the compound after the ion release tests, as compared with those of the starting compounds (**Fig. 3.13**). The X-ray diffraction patterns of GOIC and GOEC with TPP+ before and after ion release in neutral and acidic aqueous solutions are plotted in **Fig. 3.23a–c** and **d–f**, respectively.

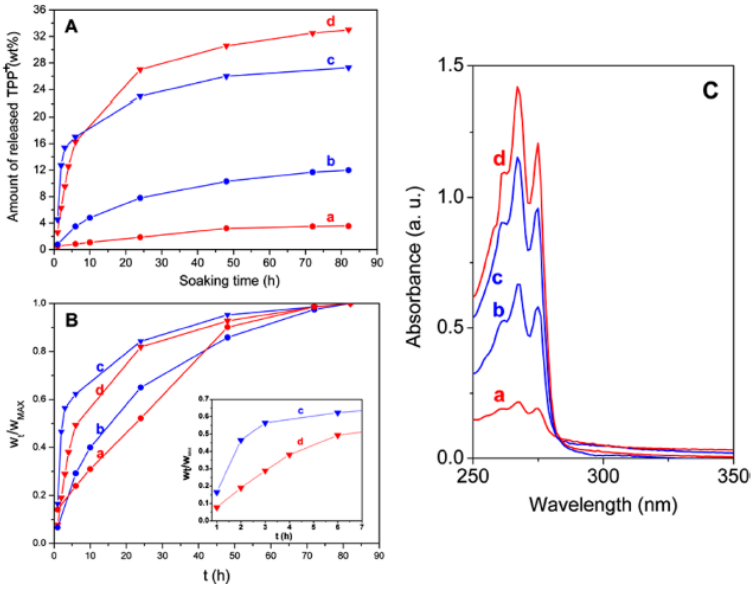

Figure 3.12. TPP+ release from GOIC (red curves and symbols) and GOEC (blue curves and symbols) in neutral saline (a,b; circles) or in acidic (c,d; pH = 1.3; triangles) aqueous solutions: (A,B) kinetics of ion release versus soaking time, expressed as percent content with respect to the GO compound (A) or as fraction of the long-term release (B); (C) UV measurements, in the spectral range 250–350 nm, on the aqueous solutions after 82 h of soaking time.

All patterns of **Fig. 3.13** maintain unaltered the 100 and 110 (the latter not shown) peaks, indicating the maintenance of the in-plane graphitic order, independently on the GO/TPP^+ compound as well as of the considered ion release conditions. As for GOIC, the minor ion release in neutral saline water does not alter the crystalline order (cf. **Fig 3.13 a,b**), with only a broadening of the 00l reflections. In particular, the broadening of the 001 reflection indicates a decrease of the correlation length perpendicular to the graphene layers from 12 nm down to 9 nm. The X-ray diffraction pattern of GOIC sample after complete ion release in acidic water (**Fig. 3.13c**) shows instead a replacement of the 00l peaks by a broad peak being located at $2\theta \approx 12.5°$, possibly corresponding to the packing of few layers of GO (with a periodicity of d = 0.709 nm and a correlation length of 2.6 nm). A broader and weaker halo with its maximum roughly located at $2\theta \approx$

20.5° (d = 0.43 nm) is also present (**Fig. 3.13c**), possibly indicating the presence of a minor amount of exfoliated GO.

Hence, the pH sensitive ion release from GOIC (red curves in **Fig. 3.12A**) is due to the stability of its crystalline structure in neutral solutions and its complete destruction in acid solution, due to the progressive exchange of phosphonium ions with protons. As for GOEC, the ion release in neutral saline water leads only to minor changes in the X-ray diffraction patterns (**Fig. 3.13d,e**). In particular, two broad halos located at 2θ ≈ 6.4° and 13.6°, already present in the pattern of GOEC (**Fig. 3.13d**) become more intense after TPP+ release in saline water (**Fig. 3.13e**).

This suggests that the ion exchange in the saline water favors the transformation of a minor amount of GOEC in the thermodynamically more stable GOIC, although with a correlation length lower than 3 nm. The X-ray diffraction pattern of GOEC sample after complete ion release in acidic water (**Fig. 3.13**) shows instead only a broad halo being roughly centered at 2θ ≈ 26.5°, corresponding to fully exfoliated graphite. This indicates that long-term treatments of GOEC in the acid aqueous environment leads to a substantial reduction of the graphene oxide layers to graphene layers. **[53-54]**

Also informative is a closer look to the release kinetics of **Fig. 3.12A**, as obtained by plotting the data as a fraction of the long-term release versus the soaking time (Figure 6B). For the faster kinetics of ion release in the acidic solution, an enlargement of the first few hours is also shown as inset of Figure 6B. It is apparent that, as expected, the release kinetics are faster for GOEC than for GOIC. Moreover, for GOIC both in neutral (curve a in **Fig. 3.12A**) and acidic (curve d in the inset of **Fig. 3.12B**) aqueous solutions, the ion release is linear with time, for hours. This ion release being linear with time (generally indicated as zero order release) **[54-56]** can be possibly rationalized by water diffusion in GOIC behind a sharp front separating swollen and unpenetrated solid.**[56][57]**

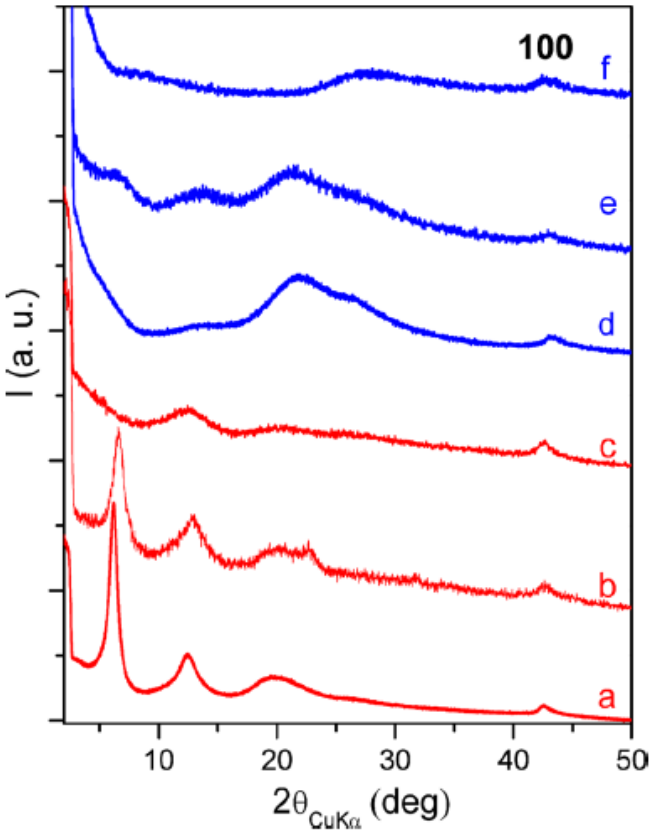

Fig 3.13. X-ray diffraction patterns (CuKα) of GOIC (a–c) and GOEC (d–f) with TPP+ before (a,d) and after partial ion release in neutral aqueous solutions (b,e) or complete ion release in acidic aqueous solutions (c,f). The 100 graphitic reflection is maintained for all samples.

Conclusions

Starting from GO, graphite oxide intercalation compounds (GOIC) with bulky guest molecules and with large interlayer spacing, which exhibit a high crystalline order in the interlayer space, have been obtained. In particular, intercalation in the interlayer space of ionic guest molecules with two long hydrocarbon tails leads to an increase of the interlayer spacing up to 3.4 nm, moreover the inclusion in the interlayer space of an additional guest molecule, being polar and also including one or two long

hydrocarbon chains, leads to additional increase of the interlayer spacing (up to 5.8 nm) and of the crystalline order. Besides the increase of the spacing, the presence of an hexagonal rotator order of the intercalated hydrocarbon chains, and its reversibility with temperature, are clearly confirmed by combined differential scanning calorimetry (DSC) and WAXD measurements.

Preparation procedures suitable to produce highly ordered graphite oxide intercalation compounds (GOIC) or fully disordered graphite oxide exfoliated compounds (GOEC) have been described, for two different quaternary phosphonium salts too. Intercalated compounds were prepared by using the same procedure for GOIC with ammonium salts, while exfoliated compounds were prepared by exfoliation of GO powders in NaOH aqueous solutions, followed by treatment of the exfoliated GO powders with the organic salt.

The two prepared GOICs exhibit a similar crystalline structure, with long-range order only parallel and perpendicular to the GO layers, with no evidence of order in

the arrangement of the phosphonium ions in the interlayer space. By simple casting procedures, macroscopic films with

high degree of uniplanar orientation of GOIC crystallites have also been obtained.

Finally, their kinetics of release of the ionic antibacterial agent. The obtained results indicate that, by controlling the crystalline structure of the GO compounds, it is possible to control the release kinetics of cations in water. For neutral saline solutions, the ion release is only partial and much lower for GOIC than for GOEC. For acid solutions, for pH close to that one of the human stomach, the ion release becomes complete for both GOIC and GOEC (close to 30 wt %). For GOIC, the ion release in both environments is constant with time, at least for release lower than 40 wt %, i.e., it can be described in terms of zero order kinetics. Hence, GOICs exhibit pH sensitive cation release, with zero order kinetics, which could be helpful for applications requiring triggered and constant supply of active ions.

References

[1] Y. Matsuo, T. Niwa, Y. Sugie. *Carbon* **1999**, 37, 897–901.

[2] I. Dekany, R. Kruger-Grasser, A. Weiss. *Colloid. Polym. Sci.* **1998**, 276, 570–6.

[3] Y. Matsuo, K. Hatase, Y. Sugie. *Chem. Lett.* **1999**, 12, 1109–10.

[4] Z. Liu, Z. M. Wang, X. Yang, K. Ooi. *Langmuir* **2002**, 18, 4926–32.

[5] Y. Matsuo, Miyabe T, Fukutsuka T, Sugie Y. *Carbon* **2007**, 45, 1005–12.

[6] S. Stankovich, D.A. Dikin, O.C. Compton, G.H.B. Dommet, R.S. Ruoff, S.B.T. Nguyen. *Chem. Mater.* **2010**, 22, 4153–7.

[7] K. Zhang, L. Mao, L.L. Zhang, H.S.O. Chan, X.S. Zhao, J. Wu. *J. Mater. Chem.* **2011**, 21, 7302–7.

[8] Acik M, Dreyer DR, Bielawski CW, Chabal YJ. J Phys Chem C 2012;116:7867–73.]

[9] R. Bissessur, S.F. Scully. *Solid State Ionics* **2007**, 178, 877–82.

[10] H. Bai, C. Li, X. Wang, G. Shi. *J. Phys. Chem. C* **2011**, 115, 5545–51.

[11] T.N. Blanton, D. Majumda. *Powder Diffr.* **2012**, 27, 104–7.

[12] Y. Okahata, A. Shimizu. *Langmuir* **1989**, 5, 954–9.

[13] R.A. Vaia, R.K. Teukolasky, E.P. Giannelis. *Chem. Mater.* **1994**, 6, 1017–22.

[14] P. Beaudot, M.E. De Roy, J.P. Besse. *Chem. Mater.* **2004**, 16, 935–45.

[15] M.A. Osman, M. Ploetze, P. Skrabal. *J. Phys. Chem. B* **2004**, 108, 2580–8.

[16] L.Y. Wang, G.Q. Wu, D.G. Evans. *Mater. Chem. Phys.* **2007**, 104, 133–40.

[17] M. Galimberti, A. Lostritto, A. Spatola, G. Guerra. *Chem. Mater.* **2007**, 19, 2495–9.

[18] F. Kooli. *Langmuir* **2009**, 25, 724–30.

[19] M. Galimberti, S. Senatore, L. Conzatti, G. Costa, G. Giuliano, G. Guerra. *Polym. Adv. Technol.* **2009**, 20, 135–42.

[20] M. Galimberti, S. Giudice, V. Cipolletti, G. Guerra. *Polym. Adv. Technol.* **2010**, 21, 679–84.

[21] M. Kajino, T. Saito, M. Okamoto, H. Sato, Y. Ozaki.

Appl. Clay. Sci. **2010**, 48, 73–80.

[22] A. Das, K.W. Stockelhuber, R. Jurk, D. Jehnichen, G. Heinrich. *Appl. Clay. Sci.* **2011**, 51, 117–25

[23] S. Babu, M.S. Seehra. *Carbon* **1996**, 34, 1259–65.

[24] M. Mauro, V. Cipolletti, M. Galimberti, P. Longo, G. Guerra. *J. Phys. Chem. C* **2012**, 116, 24809–13.

[25] S.Y. Chazhengina, E.N. Kotelnikova, I.V. Filippova, S.K. Filatov. *J. Mol. Struct.* **2003**, 647, 243–57.

[26] M. Dirand, Z. Achour-Boudjema. *J. Mol. Struct.* **1996**, 375, 243–8.

[27] V. Chevallier, D. Petitjean, M. Bouroukba, M. Dirand. *Polymer* **1999**, 40, 2129–37.

[28] Fu D, Liu Y, Su Y, Liu G, Wang D. J Phys Chem B 2011;115:4632–8.

[29] D. Fu, Y. Liu, G. Liu, Y. Su, D. Wang. *Phys. Chem. Chem. Phys.* **2011**, 13, 15031–6.

[30] G. Ungar, N. Masic. *J. Phys. Chem.* **1985**, 89, 1036–42.

[31] Y. Ide, M. Ogawa. *J. Colloid. Interface. Sci.* **2006**, 296, 141–9.

[32] T. Itoh, N. Ohta, T. Shichi, T. Yui, K. Takagi. *Langmuir* **2003**, 19, 9120–6.

[33] L.Z. Zhang, J.C. Yu, H.Y. Yip, Q. Li, K.W. Kwong,; W. Xu, P. K. Wong. *Langmuir* **2003**, 19, 10372−10380.

[34] Ohashi, F.; Ueda, S.; Taguri, T.; Kawachi, S.; Abe, H. Appl. ClaySci. 2009, 46, 296−299.

[35] P. Herrera, R.C. Burghardt, T.D. Phillips. *Vet. Microbiol.* **2000**, 74, 259−272.

[36] X. Cai, S.Z. Tan, M.H. Liao, T. Wu, R.F. Liu, B. J. Yu. *Cent.South Univ. Technol.* **2010**, 17, 485−491.

[37] G. Ramorino, F. Bignotti, S. Pandini, T. Ricco. *Compos. Sci. Technol.* **2009**, 69, 1206−1211.

[38] J.W. Rhim, S.I. Hong, C.S. Ha. *LWT-Food Sci. Technol.* **2009**, 42, 612−617.

[39] X. Cai, S. Tan, M. Lin, A. Xie, W. Mai, X. Zhang, Z. Lin, T. Wu, Y. Liu. *Langmuir* **2011**, 27, 7828−7835.

[40] A.G. Xie, X. Cai, M.S. Lin, T. Wu, X.J. Zhang, Z.D. Lin, S. Tan. *Mater. Sci. Eng. B* **2011**, 176, 1222−1226.

[41] Y. Matsuo, T. Niwa, Y. Sugie. Carbon **1999**, 37, 897−901.
[42] Y. Matsuo, K. Hatase, Y. Sugie. *Chem. Lett.* **1999**, 1109−1110.
[43] Z.M. Liu, Y. Wang, X. Yang, K. Ooi. *Langmuir* **2002**, 18, 4926−4932.
[44] C. Nethravathi, M. Rajamathi. *Carbon* **2006**, 44, 2635−2641.
[45] Y. Matsuo, T. Miyabe, T. Fukutsuka, Y. Sugie. *Carbon* **2007**, 45, 1005−1012.
[46] S. Stankovich, D.A. Dikin, O.C. Compton, G. H. B. Dommett, R.S. Ruoff, S.T. Nguyen. *Chem. Mater.* **2010**, 22, 4153−4157.
[47] K. Zhang, L. Mao, L.L. Zhang, H.S.O. Chan, Zhao, X. S. J. Wu. *J. Mater. Chem.* **2011**, 21, 7302−7307.
[48] M. Acik, D.R. Dreyer, C.W. Bielawski, Y.J. Chabal. *J. Phys. Chem. C* **2012**, 116, 7867−7873.
[49] P. K. Ang, S. Wang, Q. Bao, J.T. Thong, K.P. Loh. *ACS Nano* **2009**, 3, 3587−3594.
[50] M. Mauro, M. Maggio, V. Cipolletti, M. Galimberti, P. Longo, G. Guerra. *Carbon* **2013**, 61, 395−403.
[51] V. Cipolletti, M. Galimberti, M. Mauro, G. Guerra. *Appl. Clay Sci.* **2014**, 87, 179−188.
[52] Z. Bo, X. Shuai, S. Mao, H. Yang, J. Qian, J. Chen, J. Yan, K. Cen. *Sci. Rep.* **2014**, 4, 4684.
[53] J. Zhang, H. Yang, G. Shen, P. Cheng, J. Zhang, S. Guo. *Chem. Commun.* **2010**, 46, 1112−1114.
[54] H. Liu, S. Farrell, K.J. Uhrich. *Controlled Release* **2000**, 68, 167−174.
[55] L. Perioli, T. Posati, M. Nocchetti, F. Bellezza, U. Costantino, A. Cipiciani. *Appl. Clay Sci.* **2011**, 53, 374−378.
[56] N.L. Thomas, A.H. Windle. *Polymer* **1982**, 23, 529−542.
[57] M. Mauro, M. Maggio, A. Antonelli, M.R. Acocella, G. Guerra. *Chem. Mater.* **2015**, 27, 1590-6.

CHAPTER 4

Carbon Black Oxide and Carbon black oxide adducts with organic ammonium ions

Oxidation studies on carbon black (CB) show that the degree of oxidation largely increases with initial BET surface areas. WAXD patterns suggest that oCB samples are mainly constituted by a disordered spatial arrangement of highly defective graphene oxide structural layers, with short in-plane correlation length (2–3 nm). This is confirmed by the ability of oCB to form ordered intercalation compounds, as for the first time reported here. In fact, tetraalkylammonium cations in which two of the alkyl groups possess long hydrocarbon tails (2HT) are able to induce formation of intercalate crystalline structures not only by ion exchange in ordered GO crystals but also by self-assembling with small and disordered oCB layers.

4.1 Preparation, Composition and Surface Areas of Carbon Black Oxide Samples

Four commercial carbon black samples, exhibiting largely different BET surface areas (in the range 33-151 m^2/g), have been oxidized according to the procedure described in Chapter 2. The oxygen content largely increases with the initial BET values, as shown by increase of the O/C weight ratio as evaluated by elemental analysis (**Table 4.1** and **Fig. 4.1**, left scale).

TABLE 4.1 Elemental analysis of oxidized carbon black (oCB) and of graphite oxide and graphene oxide samples.[a]

Sample	C (wt%)	H (wt%)	O (wt%)	S (wt%)	O/C
oCB(SA_{CB}= 33 m^2/g)	85.9	0.2	13.7	<0.2	0.16
oCB(SA_{CB}= 77 m^2/g)	70.2	0.8	26.0	2.7	0.37
oCB(SA_{CB}= 125 m^2/g)	60.3	1.6_5	35.0	2.8	0.58
oCB(SA_{CB}= 151 m^2/g)	50.3	2.3	41.7	5.4	0.83
Graphene oxide	59.4	0.6	37.1	2.6	0.62
Graphite oxide	56.1	1.2	39.8	2.7	0.71

[a] Elemental composition of anhydrous samples: The error in C and O content is close to 1wt% while the error in H content is close to 0,1 wt%; water contents (as evaluated by TGA, after equilibration at room temperature in air with a relative humidity of 45%) was in the range 10-15 wt%, for all the examined samples.

For the sake of comparison, the elemental analyses of a graphite oxide (GO) sample, as obtained by the same oxidation procedure from a high-surface-area (330 m^2/g) graphite, as well as of this GO sample after 24 h of ball milling (exfoliated GO, eGO) are also reported in Table 1. It is apparent

that comparable degrees of oxidation are achieved for high surface area carbon black and graphite samples.

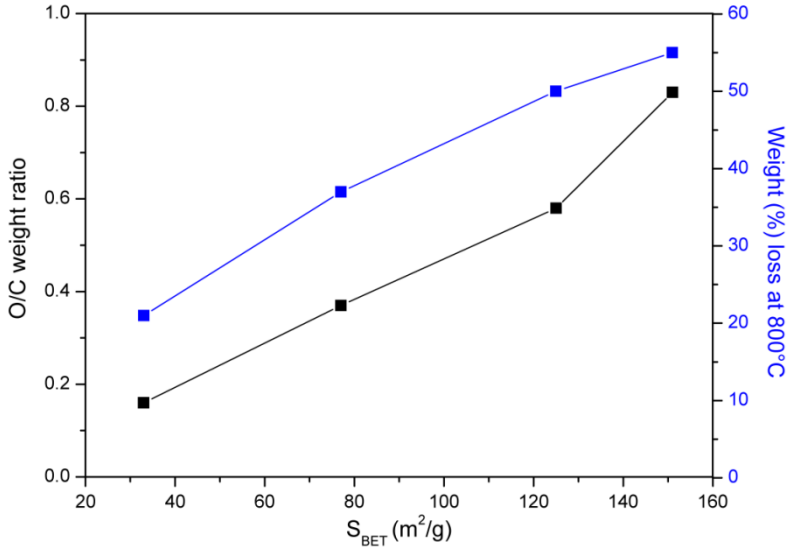

Figure 4.1. O/C weight ratio (left scale, black squares) and weight loss at 800°C in TGA scans (right scale, blue triangles) of the oxidized CB samples, versus the BET surface area of the starting CB samples.

Differences in oxidation behavior of CB samples exhibiting different BET values is also clearly shown by TGA scans, like those shown in **Fig. 4.2** The weight loss largely increases with the oCB oxygen content and, hence, with the initial BET surface area. This is shown, for instance, by the weight loss at 800°C as taken from TGA scans of **Fig. 4.2**, which is reported versus the BET surface area of the initial CB samples in **Fig. 4.1** (right scale).

TGA scans of GO and eGO samples, as obtained by the same oxidation procedure, are also shown in **Fig 4.2**. It is apparent that oCB, GO and eGO samples, for similar O/C ratios, present similar TGA losses. However, for GO and eGO samples the main weight loss phenomenon is split in two steps, rather than continuous, as for oCB samples. This is possibly more clearly shown by the DTGA scans of **Fig. 4.2B**.

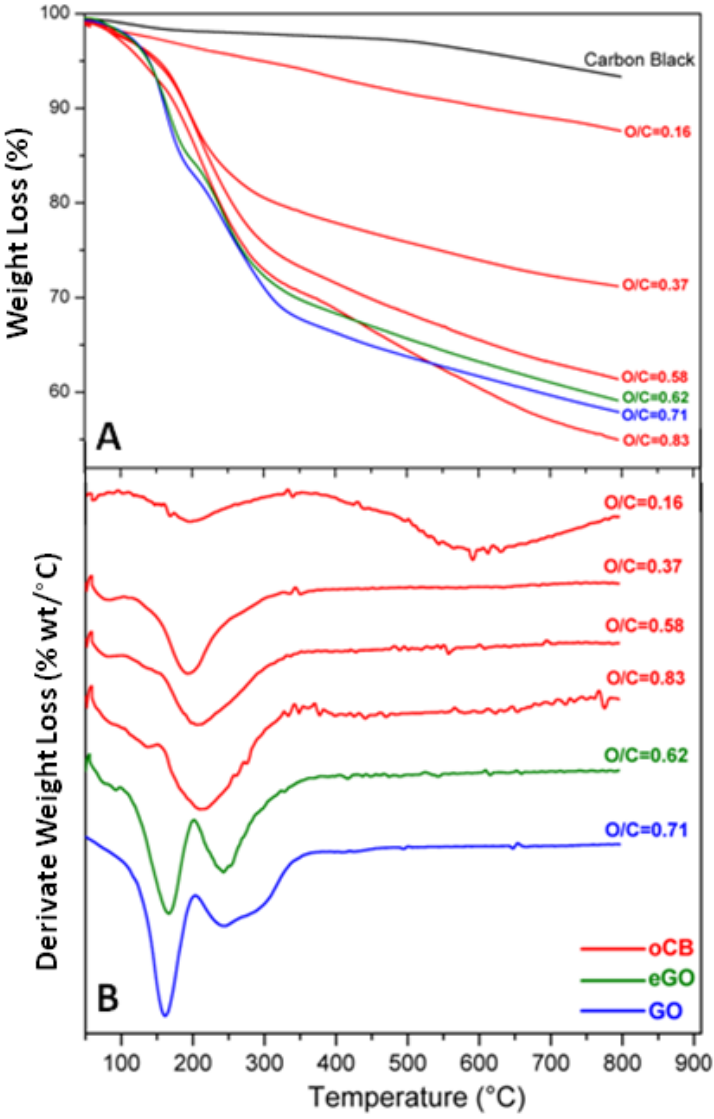

Figure 4.2 TGA scans at 20K/min, after drying at 100°C in the TGA apparatus, of oCB and GO and eGO samples: (A) TGA; (B) DTGA. Close to each curve, their O/C weight ratio is indicated.

Although elemental analyses and TGA scans suggest similar oxidation behaviors of graphite and carbon black, large differences in reactivity of the obtained oxygenated functional groups are clearly pointed out by DSC scans (**Fig. 4.3**). All samples show an endothermic peak, whose intensity

increases with the degree of oxidation, which is centered in the temperature range 105-130°C, with a ΔH_{endo} which increases with the O/C ratios up to 250-300 J/g. This endothermic peak is possibly mainly associated with removal of intercalated water.**[27-31]** DSC behavior is, however, completely different at higher temperatures. In fact, oCB samples present broad endothermic phenomena, with multiple peaks. In particular, the maximum ΔH_{endo} value for the whole broad endothermic phenomenon (close to 490 J/g) is observed for the most oxidized oCB sample (O/C=0.83). DSC scans of GO and eGO samples, on the contrary and in agreement with several literature reports, [27-31] exhibit intense exothermic peaks in the temperature region 170°C-220°C, with large enthalpy changes (ΔH_{exo} = 895 J/g and 460 J/g, for GO and eGO, respectively).

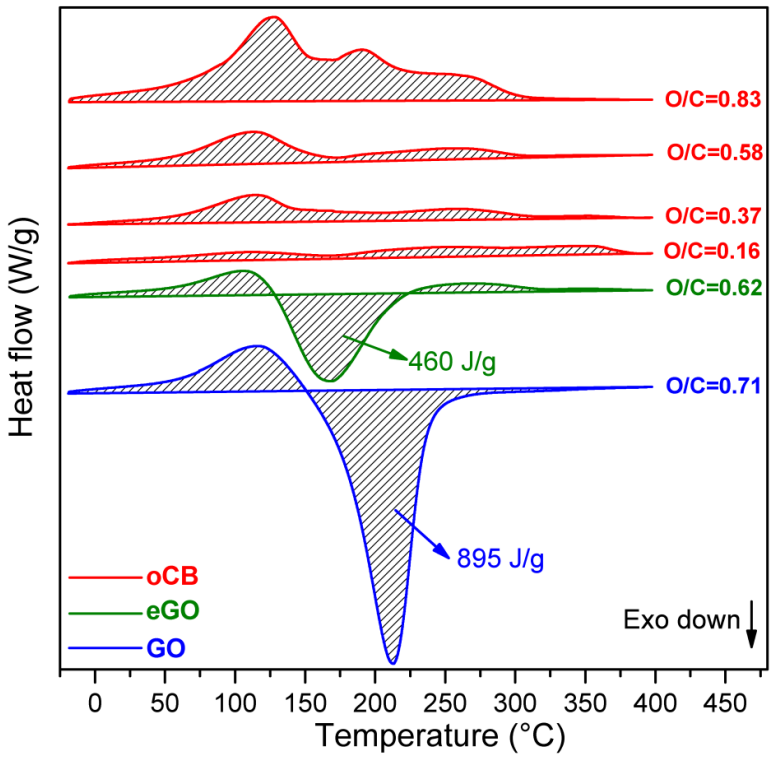

Figure 4.3 DSC scans at 10°C/min of GO, eGO and oCB samples. Close to each curve, their O/C weight ratio is indicated.

The chemical origin of the GO exothermic peak has not yet received full explanation in the literature. However, it is well established that the intense exothermic peak is associated with a dramatic mass loss, mainly due to loss of CO_2 and H_2O.**[27-31]**

We add here some simple thermodynamic considerations, relative to possible dehydration and decarboxylation reactions leading to double bond formations. These reactions, in fact, are endothermal when lead to isolated or even conjugated double bonds while become exothermal only when also lead to aromatization.

The prevalence of endothermal phenomena for oCB can be possibly rationalized by prevalence of dehydration and decarboxylations reactions, which do not lead to aromatization.

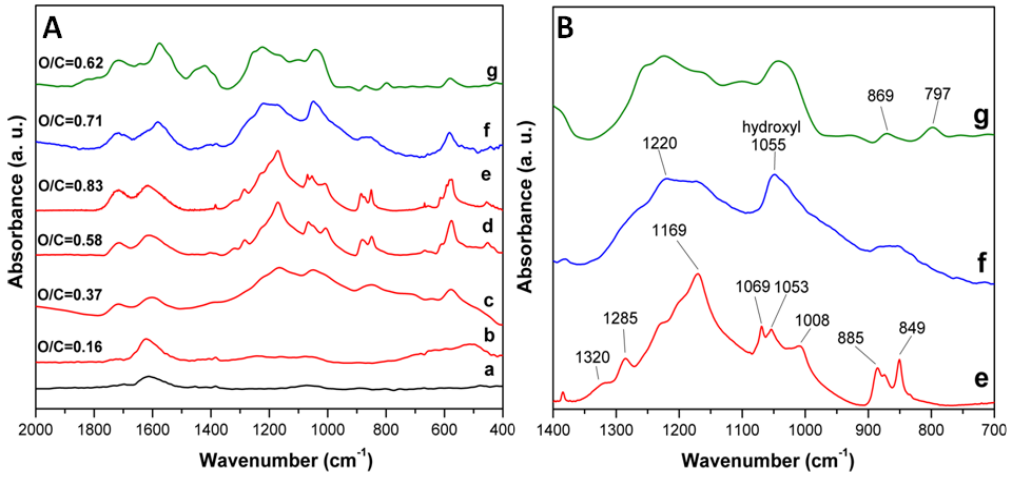

Figure 4.4 FTIR spectra of CB (**a**), oCB (**b-e**), graphite oxide (**f**) and graphene oxide (**g**) samples, in different spectral ranges: (A) 2000-400 cm^{-1}; (B) 1400-700 cm^{-1} (only for spectra **e** and **f**). In A, close to each curve of oxidized samples, their O/C weight ratio is indicated.

The different oxidation degree for the prepared oCB samples clearly appears also from FTIR spectra (**Fig. 4.4**). In particular, as O/C ratio increases, the carboxylic 1718 cm-1 peak consistently increases. Moreover,

with increasing oxygen content, many vibrational peaks appear in the 1300-900 cm^{-1} range (mainly referring to C-O stretching of ether, epoxy, alcoholic and carboxylic groups) as well as two well defined peaks at 885 and 849 cm^{-1} assigned to the asymmetric stretching and deformation vibrations of epoxy groups respectively and a 575 cm^{-1} peak which could be possibly attributed to peroxides. **[32]** FTIR spectra of oCB, for O/C weight ratio higher than 0.5 (e.g. **Fig. 4.4d,e**), are very similar to each other. However, they are definitely different from those of graphite oxide samples obtained by oxidation of different kinds of graphites (e.g., **Fig. 4.4f**) as well as of graphene oxide samples (by mechanical milling **[33]** of graphite oxide, **Fig. 4.4g**). Spectral differences between oCB and GO samples are more clearly pointed out in **Fig. 4.4B**. This more detailed comparison shows that most vibrational peaks are better defined in oCB while some peaks also become more intense. The presence for oCB of well defined vibrational peaks located at 1320, 1169, 849 cm^{-1} and 1008 cm^{-1} indicate the occurrence of an increased fraction of epoxy groups and ether (furan type) groups **[32]**, respectively. Moreover, the well defined vibrational peak located at 1069 cm^{-1} reveals the contribution of an increased amount of sulfonic group **[34,35]**.

WAXD patterns (CuKα) of the considered CB samples and of the corresponding oCB samples are compared in **Fig. 4.5**.

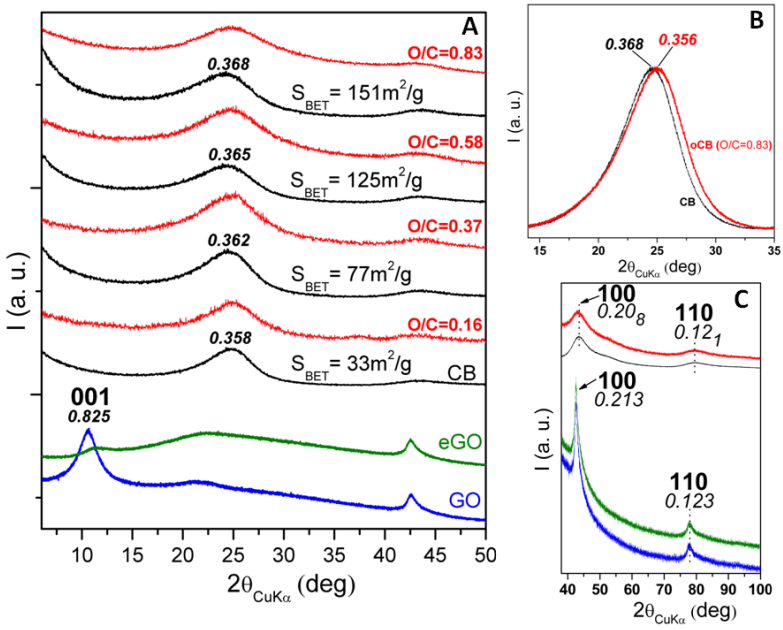

Figure 4.5 (A) X-ray diffraction patterns of CB samples with different BET surface areas, before (black curves) and after the oxidation procedure (red curves). Close to each couple of patterns the starting BET value and the final O/C weight ratios are indicated. (B,C) Enlarged X-ray diffraction patterns of CB with S_{BET} = 151 m^2/g and of the corresponding oCB with O/C=0.85, for different 2θ ranges: (B) 15°-35°; (C) 38°-100°.

All carbon black samples present very similar diffraction patterns (black in **Fig. 4.5**), with broad diffraction halos. However, with increasing the CB surface area, the maximum of the more intense diffraction halo is slightly shifted (from 0.358 nm up to 0.368 nm, **Fig. 4.5A**), thus indicating a corresponding slight increase of average distances between scattering atoms. WAXD patterns of CB samples also present two minor halos centered, independently of the CB surface areas, at 0.21 and 0.12 nm (**Fig. 4.5C**), corresponding to 100 and 110 in-plane graphite reflections. **[36-40]** The broadness of the 100 and 110 reflections of the used carbon black indicate correlation lengths in the range 2.1-2.3 nm, which are definitely

smaller than correlation lengths of 100 and 110 reflections of GO and eGO samples (in the range 11.1-11.3 nm).

WAXD patterns of the corresponding oCB samples are shown as red curves in **Fig. 4.5**. The oxidation procedure does not significantly change position, broadness and intensity of the 100 and 110 diffraction peaks (**Fig. 4.5C**), clearly indicating that the extensive oxidation poorly affects the graphitic in-plane correlation lengths. As for the main diffraction halo, some broadening and minor shift with increasing the degree of oxidation is observed. In particular, for the most oxidized sample the half-eight-width β slightly increases from 5.4 to 5.8 nm (**Fig. 4.5B**), indicating induction of additional disorder by the oxidation procedure. Correspondingly, the position of its maximum moves from 0.368 nm down to 0.356 nm (**Fig. 4.5B**), at least is in part due to S_{BET} decrease from 151 m^2/g down to 60 m^2/g, which is associated with oxidation.

It is worth adding that the comparison between WAXD patterns of CB and corresponding oCB samples (**Fig. 4.5**) also gives relevant information on CB and oCB structures. It is well known that, by progressive oxidation of graphite to graphite oxide, the basal periodicity progressively increases from 0.34 nm typical of graphite up to values in the range 0.7-0.8nm **[41-48]**, for O/C weight ratios in the range 0.5-1.0. The nearly unaltered position of the main diffraction halo, even for high levels of oxidation (O/C ratios higher than 0.8, **Fig. 4.5A**), makes questionable its interpretation in terms of a very broad 002 graphitic reflection **[37]**, while suggests that CB and oCB samples can be interpreted as a disordered spatial arrangement of graphene and graphene oxide layers, exhibiting short in-plane correlation length.

4.2 oCB/2HT adducts

X-ray diffraction patterns (CuKα) of 2HTCl (a), oCB (b), and of oCB/2HT adducts, as obtained from oCB samples with O/C weight ratios in the range 0.16-0.83 (c-f), are shown in **Fig. 4.6**.

The patterns of **Fig. 4.6c-f** show that, for O/C ratio ≈ 0.45, well defined diffraction peaks appear: at d = 4.8 nm (inset B of **Fig. 4.6**), d = 1.6 nm and d = 0.94 nm (inset C of **Fig 4.6**). These peaks can be rationalized as 001, 003 and 005 reflections of an oCB/2HT intercalate structure and clearly suggest that the shoulder appearing at d = 2.4 nm (indicated by a red arrow in **Fig. 4.6A**) can be attributed to the corresponding 002 reflection. This shows a clear odd-even effect for the 00l reflections, with definitely more intense odd reflections. The observed periodicity of 4.8 nm, being definitely higher than the 001 periodicity of the 2HTCl salt (3.3 nm, **Fig. 4.6a**), and the disappearance of all diffraction peaks of this salt clearly indicate the adduct formation.

Patterns b-f of **Fig 4.6** also show that, as O/C ratio increases, a broad diffraction peak centered at d = 0.42 nm appears and increases its intensity while the main carbon black amorphous halo progressively reduces its intensity. This peak can be rationalized by the formation of a hexagonal hydrocarbon rotator order, analogous to those formed in intercalate compounds of surfactants, exhibiting long hydrocarbon chains, with graphene oxide **[21]** (**Fig. 4.6g**) as well as with organoclays **[22-25]**.

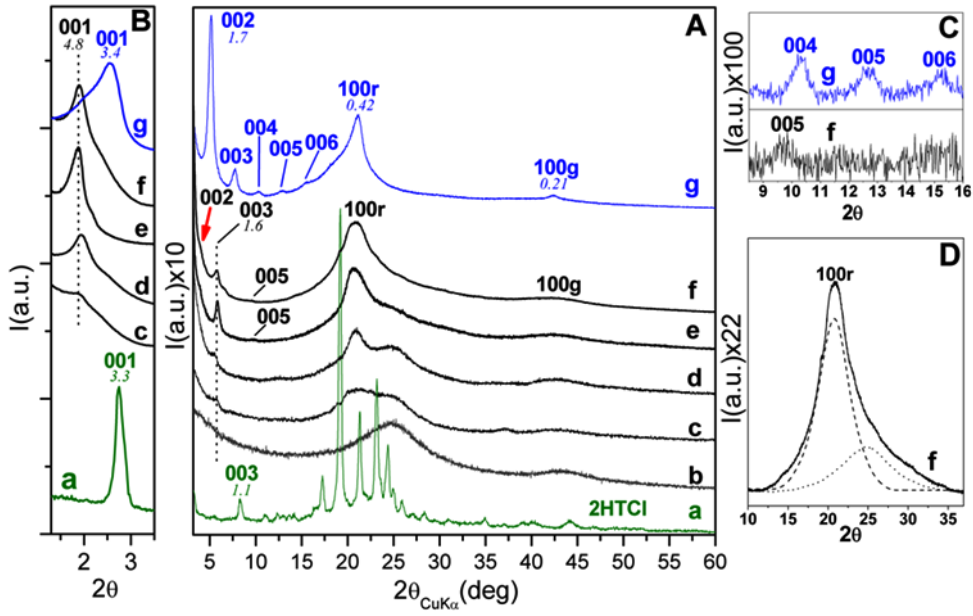

Figure 4.6. X-ray diffraction patterns of : a) 2HT; b) one of the prepared oCB sample; c-f) oCB/2HT adducts, as obtained from oCB samples with different O/C molar ratios: 0.16 (c), 0.37 (d), 0.58 (e), 0.83 (f); g) (graphene oxide)/2HT adduct. Insets B and C show enlarged patterns for 2θ ranges 1.4°-3.5° and 8°-16°, respectively. The inset D shows an enlarged f pattern, for 2θ range 10°-37°, with intensity contributions from rotator phase (dashed line) and from residual amorphous carbon (dotted line).

The large spacing observed for oCB/2HT intercalates (4.8 nm), suggests an orientation of the ion hydrocarbon tails being nearly perpendicular with respect to the graphitic layers, as shown in **Fig. 4.7**. This hypothesis is confirmed by the well-defined odd-even effect for the 00l reflections, with definitely more intense odd reflections (Fig. **4.6d-f**). In fact, this feature can be rationalized by the minimum of atomic density in the middle of the graphitic interlayer space of the intercalate (lateral view of **Fig 4.7**), due to non-bonded interactions between tails of the hydrocarbon chains.

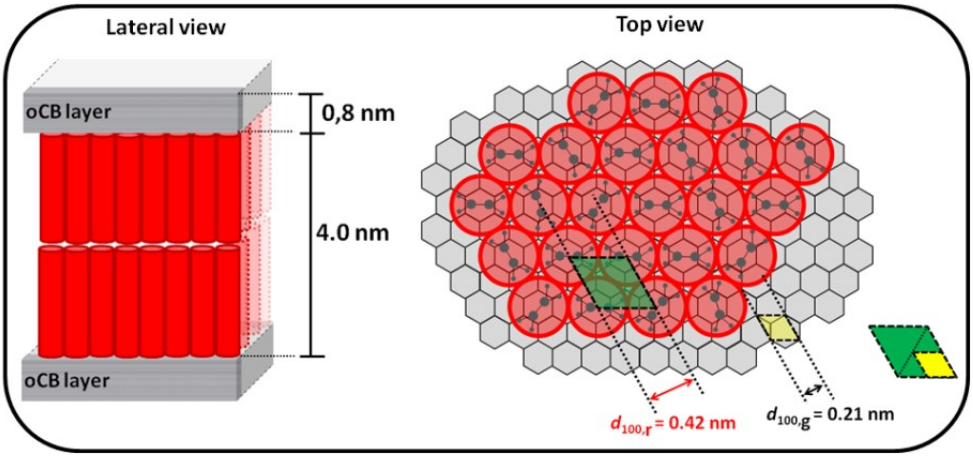

Figure 4.7. Schematic lateral and top views of the proposed crystalline structure of the oCB/2HT intercalate. Red cylinders and circles indicate hydrocarbon tails of the ammonium cation, for lateral and top view, respectively. In the top view, bases of hexagonal unit cells of graphite (yellow rhombus) and of the hydrocarbon rotator order (green rhombus) and dotted lines representing 100 crystal planes of graphite (d = 0.21 nm) and of the rotator order (d ≈ 0.42 nm).

The intercalate crystal structure of **Fig. 4.7** is possibly stabilized by the good fit between the bases of the hexagonal unit cells of graphitic layers (with 2 carbon atoms and d_{100} = 0.21 nm) and of the rotator order (with 1 hydrocarbon tail and d100 ≈ 0.42 nm), as shown in the top view of **Fig. 4.7**. This intercalate structure hence exhibits 1 hydrocarbon tail per 8 graphitic carbon atoms, i.e. 1 ion 2HT per 16 graphitic carbon atoms.

This molar ratio is definitely higher than those evaluated for the oCB/2HT adducts. In fact, even for the most oxidized sample, n_{2HT}/n_C is only 1/30, according to gravimetric measurements (W2HT/ WoCB = 0.825) or 1/27 according to elemental analysis (C=74.5 wt%, O= 15.5wt%, H=8.3 wt%, N=1.6 wt%). This indicates that nearly 50% of the oCB sample is not involved in the formation of the intercalate ordered structure. This conclusion based on gravimetric and structural data, well agrees with the partial maintenance of the oCB amorphous halo whose maximum is

located at 2θCuKα ≈ 25° at d ≈ 0.36 nm (**Fig. 4.6 c-e**), which is still present even in the pattern of **Fig. 4.6f** (inset D).

For the sake of comparison, the WAXD pattern of the obtained adduct from crystalline graphite oxide and 2HT (GO/2HT adduct, which also includes 1 ion 2HT per 16 graphitic carbon atoms **[21]**) is shown in **Fig. 4.6g**. GO/2HT adduct presents with respect to oCB/2HT adducts: (i) a definitely shorter periodicity with d001 = 3.4 nm rather than 4.8 nm; (ii) a regular decrease of the intensity of the 00l reflections with l and hence absence of the odd-even effect; (iii) a higher crystalline order, as pointed out by the presence of 00l reflections with 1<l<7 (inset C of **Fig. 4.6**); (iv) a definitely sharper diffraction peak at d ≈ 0,42 nm. Features (i) and (ii) are rationalized by an inclined rather than perpendicular orientation of the hydrocarbon tails with respect to the graphitic layers **[21]**. Feature (iv) indicates a higher correlation length (D100r = 7.2 nm rather than 3.0 nm) for the hexagonal rotator order. It is also worth adding that for GO/2HT adduct, gravimetric measurements ($n_{2HT}/n_C \approx 1/17$), indicate that essentially the whole GO sample is involved in formation of the intercalate structure.

Hence, going from fully intercalated GO/2HT adducts to partially intercalated oCB/2HT adducts, the orientation of the hydrocarbon tails from inclined becomes nearly perpendicular to the graphitic planes. It is reasonable to assume that this preferential perpendicular orientation could be determined by the small lateral size of the carbon black layers and hence to the small lateral size of the hydrocarbon chain bundles.

Crystalline oCB/2HT adducts like those of **Figures 4.6d-f** remain stable after mechanical milling, as well as after extraction by supercritical carbon dioxide. On the contrary, for dispersion of the adduct in n-hexane followed by fast solvent removal, the oCB/2HT adduct can be fully exfoliated, also with complete loss of the ordered rotator phase of the ionically bonded long hydrocarbon chains.

Also informative are SEM images of oCB and of the corresponding oCB/2HT adducts. This is shown, for instance, for the oCB sample with O/C = 0.83, in Figure 8. It is clearly apparent that the amorphous oCB sample presents micrometric morphologies while the oCB/2HT adduct exhibits a much finer

morphology, possibly platelets (see inset of **Fig. 4.8**) whose lateral size is in the range 20-50 nm.

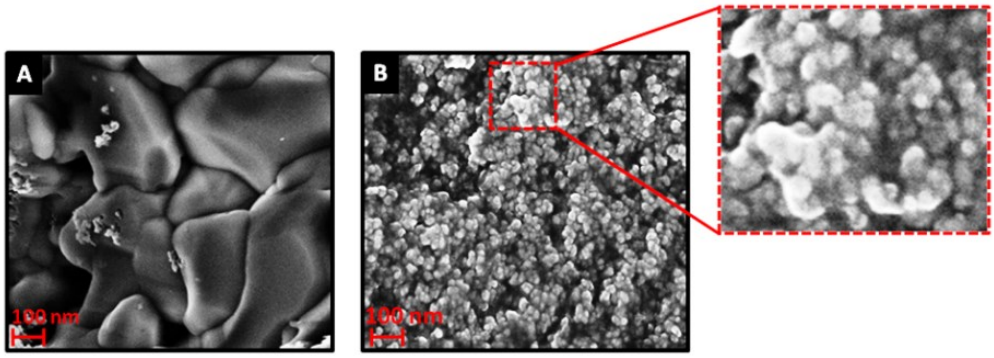

Figure 4.8. SEM images of oCB, with O/C molar ratio of 0.83 (A) and of the corresponding oCB/2HT adduct (B).

It is worth adding that the analogous preparation procedure, when conducted with the ammonium salt with only one long hydrocarbon chain (1HT), leads to a oCB/1HT adduct with an analogous rotator phase peak at d = 0.42 nm, which however does not show low 2θ peaks typical of the intercalate structure. Hence, the ammonium ion exhibiting only one hydrocarbon chain is able to decorate small layers of CB by a hydrocarbon rotator phase. However, it is not able to induce formation of the 3D ordered intercalate phase.**[49]**

Conclusions

Oxidation studies on different carbon black (CB) samples show that, for a same oxidation procedure, the degree of oxidation largely increases with the BET surface areas of the starting CB. WAXD patterns of CB and oCB samples can be interpreted by a disordered spatial arrangement of defective graphene and graphene oxide layers, exhibiting short in-plane correlation length (typically in the range 2–3 nm).

Ordered intercalation compounds can be also obtained if the starting material is completely disordered like oxidized CB (oCB). These intercalation compounds with oCB (with a O/C molar ratio higher than 0.3) have been prepared following the same procedure of that reported for the preparation of GOICs. X-ray diffraction patterns of oCB/2HT adducts show, not only few 00l reflections that indicate an intercalate crystalline structure with spacing between graphitic layers of 4.8 nm, but also *hk*0 reflections typical of the hexagonal rotator order of the intercalated hydrocarbon chains (with d_{100}=0.42 nm).

The unexpected formation of an ordered intercalate crystalline structure from highly disordered oxidized CB can be rationalized by: (i) replacement of metal ions with ammonium ions on graphitic layers of oxidized CB; (ii) organization of ionically bonded hydrocarbon chains in hexagonal rotator phases; (iii) self-assembling of decorated graphitic layers in 3D ordered intercalate crystalline structures, with hydrocarbon chains nearly perpendicular to the graphitic planes.

References

[1] J.O. Besenhard. *Carbon* **1976**, 14, 111-115.

[2] W.Q. Deng, X. Xu, W.A. Goddard. *Phys. Rev. Lett.* **2004**, 92, 166103.

[3] S. Chakraborty, J. Chattopadhyay, W. Guo, W. E. Billups, *Angew. Chem.* **2007**, 119, 4570–2.

[4] J. Li, L. Vaisman, G. Marom, J. K. Kim. *Carbon* **2007**, 45, 744–50.

[5] S. Heguri, N. Kawade, T. Fujisawa, A. Yamaguchi, A. Sumiyama, K. Tanigaki, M. Kobayashi. *Phys. Rev. Lett.* **2015**, 114, 1-5.

[6] H. Fujimoto, A. Tressaud. *Carbon* **2015**, 82, 176-83.

[7] Y. Matsuo, T. Niwa, Y. Sugie. Carbon **1999**, 37, 897–901.

[8] Z. Liu, Z.M. Wang, X. Yang, K. Ooi. *Langmuir* **2002**, 18, 4926–32.

[9] W. Yan, M.M. Lerner. *Carbon* **2004**, 42, 2981–7.

[10] Y. Matsuo, T. Miyabe, T. Fukutsuka, Y. Sugie. *Carbon* **2007**, 45, 1005–12.

[11] T. E. Sutto, T.T. Duncan, T.C. Wong. *Electrochim. Acta* **2009**, 54, 5648-55.

[12] S. Stankovich, D.A. Dikin, O.C. Compton, G.H.B. Dommet, R.S. Ruoff, S. B.T. Nguyen. *Chem. Mater.* **2010**, 22, 4153-7.

[13] T. Maluangnont, G.T. Bui, B.A. Huntington, M.M. Lerner. *Chem. Mater.* **2011**, 23, 1091-5.

[14] K. Zhang, L. Mao, L.L. Zhang, H.S.O. Chan, X.S. Zhao, J. Wu. *J. Mater. Chem.* **2011**, 21, 7302-7.

[15] W. Sirisaksoontorn, A.A. Adenuga, V.T. Remcho, M.M. Lerner. *J. Am Chem. Soc.* **2011**, 133, 12436-8.

[16] F. Guo, W. Xing, J. Zhou, L. Zhao, J. Zeng, Z. Liu, Q. Xue, Z. Yan, *Acta Crytall.* **2014**, 148, 220-7.

[17] X. Ai, J. Yu, M. Gu, T.B. Tang, T.J. Zhang. *Phys. Chem C* **2015**, 119, 17438-43.

[18] K. Spyrou, M. Calvaresi, E.K. Diamanti, T. Tsoufis, D. Gournis, P. Rudolf, F. Zerbetto. *Adv. Funct. Mater.* **2015**, 25, 263-9.

[19] M. Mauro, M. Maggio, A. Antonelli, M.R. Acocella, G. Guerra. *Chem. Mater.* **2015**, 27, 1590-6.

[20] C. Cabrillo, F. Barroso-Bujans, R. Fernandez-Perea, F. Fernandez-Alonso, D. Bowron, F.J. Bermejo. *Carbon* **2016**, 100, 546-55.
[21] M. Mauro, M. Maggio, V. Cipolletti, M. Galimberti, P. Longo, G. Guerra. Carbon **2013**, 61, 395-403.
[22] M. Galimberti, A. Lostritto, A. Spatola, G. Guerra. *Chem. Mater.* **2007**, 19, 2495-9.
[23] M. Galimberti, S. Senatore, L. Conzatti, G. Costa, G. Giuliano, G. Guerra. *Polym. Adv. Tech.* **2009**, 20, 135–42.
[24] M. Galimberti, S. Giudice, V. Cipolletti, G. Guerra. *Polym. Adv. Tech.* **2010**, 21, 679-84.
[25] V. Cipolletti, M. Galimberti, M. Mauro, G. Guerra. *Appl. Clay. Sci.* **2014**, 87, 179-88.
[26] W.S. Hummers, R.E. Offeman. *J. Am. Chem. Soc.* **1958**, 80, 1339.
[27] A. Lerf, H. He, M. Forster, J. Klinowski. *J. Phys. Chem. B* **1998**, 102, 4477–4482.
[28] McAllister, M.J. J.–L. Li, D.H. Adamson, C. Hannes, H.C. Schniepp, A.A. Abdala, L. Jun, M. Herrera-Alonso, D.L. Milius, R. Car, R.K. Prud'homme, I.A. Aksay. *Chem. Mater.* **2007**, 19, 4396-4404.
[29] H.A. Becerril, J. Mao, Z. Liu, R.M. Stoltenberg, Z. Bao, Y. Chen. *ACS Nano* **2008**, 3, 463-470.
[30] C.–M. Chen, J. –Q. Huang, Q. Zhang, W. –Z. Gong, Q.–H. Yang, M.–Z. Wang, Y.-G. Yang. *Carbon* **2012**, 50, 659–667.
[31] S. You, S.M. Luzan, T. Szabó, A.V. Talyzin. *Carbon* **2013**, 52, 171–180.
[32] M. Acik, G. Lee, C. Mattevi, A. Pirkle, R.M. Wallace, M. Chhowalla, K. Cho, Y. Chabal. *J. Phys. Chem. C* **2011**, 115, 19761–19781.
[33] I.Y. Jeon, Y.R. Shin, G.J. Sohn, H.J. Choi, S.Y. Bae, J. Mahmood, Jung, S.M. J. M. Seo, M.J. Kim, D.W. Chang, L. Dai, J.B. Baek. *Proc. Natl. Acad. Sci. U.S.A.* **2012**, 109, 5588−5593.
[34] Z. Wei, Y. Yang, Y. Hou, Y. Liu, X. He, S. Deng. *Chem. Cat. Chem.* **2014**, 6, 2354–2363.
[35] D. He, Z. Kou, Y. Xiong, K. Cheng, X. Chen, M. Pan, S. Mu, Carbon, 2014, 66, 312–319.

[36] M.R. Acocella, M. Mauro, L. Falivene, L. Cavallo, G. Guerra. *ACS Catal.* **2014**, 4, 492-6.
[37] H. Shi, J.N. Reimers, J.R.J. Dahn. *Appl. Cryst* **1993**, 26, 827-36.
[38] T. Ungár, J. Gubicza, G. Ribárik, C. Pantea, Waldek, T. Zerda. *Carbon* **2002**, 40, 929–37.
[39] W. Ruland, B. Smarsly. *J. Appl. Cryst.* **2002**, 35, 624-33.
[40] M. Mauro, V. Cipolletti, M. Galimberti, P. Longo, G. Guerra. *J. Phys. Chem. C* **2012**, 116, 24809-13.
[41] Y.G. Andreev, P.G. Bruce. *J. Appl. Cryst.* **2016**, 49, 24–30.
[42] D. Chen, H. Zhu, T. Liu. *Appl. Mater. Interfaces* **2010**, 2, 3702-8.
[43] Z.J. Fan, W. Kai, J. Yan, T. Wie, L.J. Zhi, J. Feng, Y.M. Ren, L.P. Song, F. Wie. *ACS Nano*, **2011**, 5, 191-8.
[44] Y. Guo, C. Bao, L. Song, B. Yuan, Y. Hu. *Ind. Eng. Chem. Res.* **2011**, 50, 7772-83.
[45] S. Zhang, Y. Shao, H. Liao, M.H. Engelhard, G. Yin, Y. Lin. *ACS Nano* **2011**, 5, 1785–91.
[46] J. Wang, X. Wang, C. Xu, M. Zhang, X. Shang. *Polym. Int.* **2011**, 60, 816–22.
[47] H. Kim, S. Kobayashi, M.A. Abdur Rahim, M.J. Zhang, A. Khusainova, M.A. Hillmyer. *Polymer* **2011**, 52, 1837-46.
[48] M. Maggio, M. Mauro, M.R. Acocella, G. Guerra. *RSC Adv.* **2016**, 6, 44522.
[49] M. Maggio, M. R. Acocella, G. Guerra. *RSC Adv.* **2016**, 6, 105565–10557.

CHAPTER 5

Graphite and Graphene Oxide paper

Nowadays, it is widely acknowledged in the scientific community that large scale production of single or few layers of graphene can be achieved by top-down processes of exfoliation and reduction of GO, through chemical or thermal treatments. **[1-4]**

It is also well recognized that the development of three-dimensional structures with graphene oxide and graphene layers, e.g. aerogels **[5-11]** or papers,**[12-20]** is expected to improve their manufacturability as well as to expand their applications.

In particular, free-standing GO paper can be obtained by vacuum filtration of colloidal dispersions of graphene oxide sheets.**[12-20]**

However GO papers, due to the high content of polar functional groups, generally exhibit a strong tendency to go back into suspension in the presence of solvents (mainly if polar or highly polar, like water), which is a major inconvenience for many applications.

This work presents GO papers as prepared after basification of the colloidal GO aqueous suspension (thereafter defined as basified GO paper and shortly b-GO paper) that exhibit thermal stability and solvent resistance much higher than usual GO papers. Moreover, it is shown that basification of GO suspensions also facilitates processing, mainly solvent casting procedures that lead to definitely more flexible papers. Spectroscopic analyses of the obtained papers have been conducted aiming to a possible rationalization of the observed behavior.

5.1 Structural characterizations of GO and b-GO papers.

The X-ray diffraction pattern (CuKα) of graphite oxide powder, obtained by oxidation of graphite samples exhibiting high shape anisotropy **[4]** and used as starting material of the present study, is shown in **Fig. 5.1A**. The pattern shows the (001) peak corresponding to an interlayer distance of 0.82 nm, with a correlation length of 4.5 nm as well as the (100) and (110) peaks (at d=0.21 nm and d=0.12 nm, respectively) corresponding to a long-range order in the graphitic planes (e.g., correlation length perpendicular to the (100) planes higher than 30 nm).

The GO paper, obtained by vacuum filtration of a GO suspension,20 has a thickness of nearly 30 mm, a C/O ratio equal to 1.4 (first line of Table 1) and a density of 1.79 +/- 0.01 g cm^3, similar to those reported in the literature for analogous GO papers.**[12]**

The X-ray diffraction pattern as taken by an automatic diffractometer of this GO paper (**Fig. 5.1**) is similar to that one reported in Fig. 1 of ref. 20 and shows only the (001) diffraction peak. This clearly indicates that, irrespective of the full exfoliation in the aqueous dispersion, GO aggregates again to graphite oxide, coming back to the starting interlayer distance (0.82nm), even with a slightly increased correlation length(from 4.5 up to 4.8 nm). The comparison between the patterns of **Fig. 5.1A** and **B** also shows an increased intensity of the (001)peak with respect to the amorphous halo as well as the disappearance of (100) and (110) peaks for the GO paper. These features are due to the occurrence in the GO paper of

uniplanar orientation of the graphitic planes parallel to the paper surface. This uniplanar orientation is clearly shown by the photographic patterns of **Fig. 5.1B' and 5.1B''**, as taken with EDGE and THROUGH geometries, i.e. by placing the X-ray beam parallel and perpendicular to the paper surface, respectively (as sketched in the lower part of **Fig. 5.1**.

In fact, as already observed for EDGE patterns of other graphite and GO papers and films,**[21,22]** the (001) reflection is present as arcs centered on the equator (corresponding to a degree of parallelism of the (001) graphite oxide planes with respect to the paper surface equal to $f_{00\ell} \approx 0.83$) while the (100) reflection is present as broad arcs centered on the meridian (**Fig. 5.1B'**). Of course, the corresponding pattern as taken by an automatic powder diffractometer (**Fig. 5.1B),** which mainly collects information relative to the equator of the EDGE pattern, completely loses information relative to the hk0 reflections.

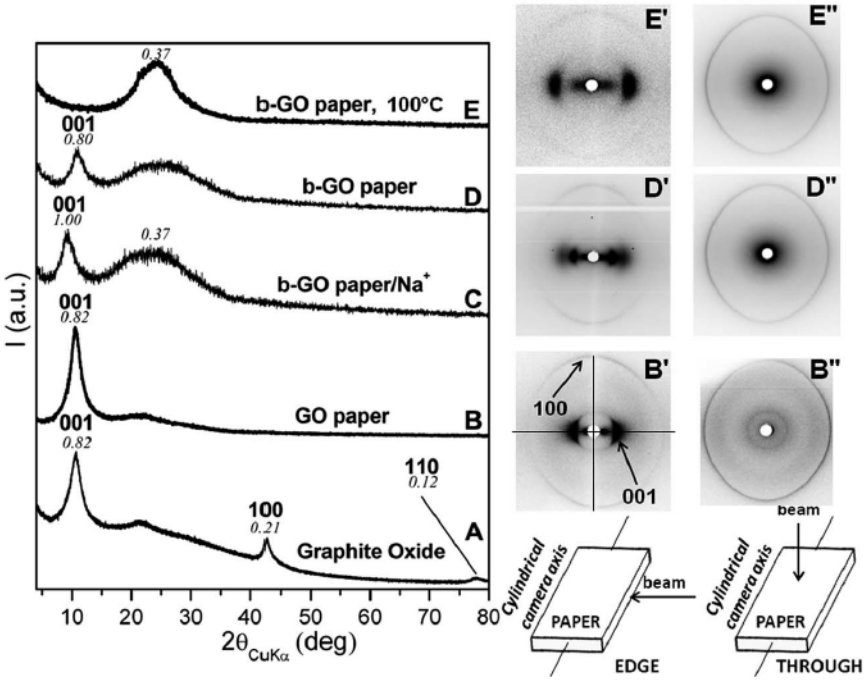

Figure 5.1. X-ray diffraction patterns (CuKa) as collected by an automatic powder diffractometer (A–E) or by a photographic camera with the X-ray beam parallel

(B0, D0 and E0 for EDGE diffraction geometry) or perpendicular to the sample surface (B", D" and E" for THROUGH diffraction geometry) for: (A) the starting graphite oxide powder; (B, B' and B") GO paper obtained by vacuum filtration of GO suspension; (C) b-GO paper, by casting of a basified GO suspension, including 13 wt% of sodium ions; (D, D0 and D00) b-GO cast paper, after sodium removal by washing with HCl solution; (E, E0 and E00) b-GO paper treated at 100 °C for 15 s. The hk' Miller indexes of the main reflections are indicated.

The b-GO paper, as obtained by casting of a b-GO suspension, has a thickness of nearly 30 mm, a C/O ratio equal to 1.1 (third line of Table 1). Hence, the adopted basification procedure leads to an increase of the oxygen content with respect to the GO paper, possibly mainly due to opening of epoxide groups on the GO layers as promoted by hydroxyl ions.

Irrespective of its higher oxygen content (1st and 3rd line of Table **5.**1) the density of the b-GO paper (1.82 +/- 0.01 g/cm^3) is even slightly higher than for the GO paper (1.79 +/- 0.01 g/cm^3).

The WAXD patterns of the cast b-GO paper, as taken by an automatic powder diffractometer, before and after sodium removal (≈13 wt%, corresponding to a C/Na ratio not far from 6), by washing with a 10 wt% aqueous HCl solution, are shown in **Fig. 5.1C** and **D**, respectively. A shift to a lower diffraction angle of the (001) reflection indicates a definitely increased interlayer spacing (d_{001}=1.0 nm, **Fig. 5.1C**), which disappears after sodium removal (d_{001}=0.8 nm, Fig. 1D). This clearly indicates the formation of an intercalate crystalline structure of graphite oxide **[21,23]** with sodium ions,38 which goes back to crystalline graphite oxide, after sodium removal by hydrochloric acid treatment.

For both patterns of **Fig. 5.1C and D**, a relevant increase of the intensity of the amorphous halo (roughly centered at d=0.37 nm) is observed. Due to the increase of oxygen content (elemental analysis of Table 1), these halos although not far from the graphitic interlayer spacing (d=0.34 nm) cannot be attributed to graphite oxide reduction. Their high intensity instead indicates a strong loss (of nearly 70%) of graphite oxide crystallinity.

X-ray diffraction patterns of the cast and washed b-GO paper as taken by a photographic camera with EDGE and THROUGH geometries, are shown in

Fig. 5.1D' and **D''**, respectively. From the EDGE photographic pattern of Fig. **1D'**, it is apparent that not only the (001) graphite oxide peak but also the broad amorphous halo are centered on the equator. Rather surprisingly, the degree of parallelism with respect to the paper surface of the amorphous halo ($f_{00\ell}$ ≈ 0.69) is even higher than for the narrower peak at d=0.8 nm (**Fig. 5.1D**), corresponding to the (001) peak of the graphite oxide component ($f_{00\ell}$ ≈ 0.60).

WAXD patterns similar to those of **Fig. 5.1D, D'** and **D''** are obtained for different sonication conditions, with intensity of the amorphous halo gradually increasing with sonication time and temperature. For instance, after sonication of the GO dispersion at 80°C for 12 h, the WAXD pattern of the obtained paper (not shown) exhibits an amorphous halo again centered at d z=0.37 nm, whose intensity is nearly 10 times higher than the intensity of the (001) graphite oxide peak still located at d =0.8 nm.

A complete loss of the (001) peak, i.e. of the crystalline order perpendicular to the graphite oxide planes can be reached by simple annealing of the b-GO paper. For instance, the WAXD pattern of the cast paper, after 15 s of treatment at 100 °C (**Fig. 5.1E**) shows only a broad halo centered at d z 0.37 nm (**Fig. 5.1F**), which is very similar to the diffraction halo of amorphous carbon **[24]** as well as of largely oxidized amorphous carbon. The two-dimensional patterns of **Fig. 5.1E'** and **5.1E"** show that the broad amorphous halo of the annealed b-GO paper is only present in the EDGE pattern (E') and centered on the equator. This again indicates a rather high degree of parallelism of graphene oxide layers, with respect to paper surface ($f_{00\ell}$ = 0.67).

The loss of crystalline order perpendicular to the GO planes, which characterize the b-GO paper of **Fig. 5.1E**, leaves essentially unaltered the in plane hk0 reflections, as shown by a comparison between (100) rings in the THROUGH patterns (Fig. **5.1B''**, **D''** and **E''**).

Hence the present results clearly indicate that the basification procedure leads to macroscopic papers with loss of crystalline order perpendicular to the GO planes, without reducing the in plane crystalline order of the GO planes. Moreover, the degree of parallelism with respect to the paper

plane of the GO layers (f circa 0.67) is still comparable with that one of the graphite oxide crystallites being present in the GO paper of **Fig. 5.1B** ($f_{00\ell}$ ≈0.83).

5.2 Structural changes with thermal and microwave treatments

GO and b-GO papers are largely different as for their structural changes as a consequence of thermal treatments. For instance, the changes of WAXD patterns, as collected by an automatic powder diffractometer, for GO and b-GO papers, as a consequence of thermal treatments in the range 200–400 °C are compared in **Fig. 5.2A** and **B**, respectively.

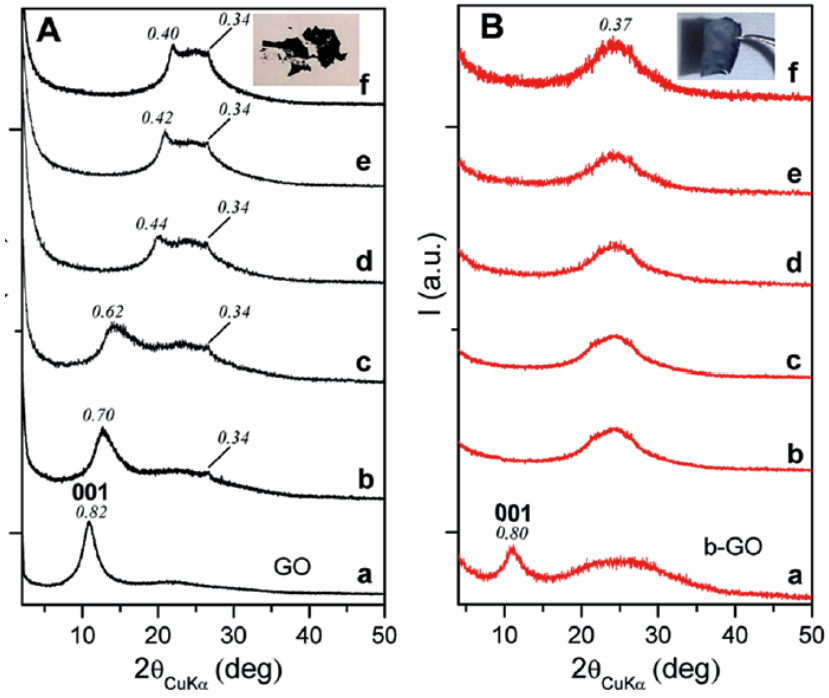

Figure 5.2. X-ray diffraction patterns (CuKα) as collected by an automatic powder diffractometer for GO paper (A) and b-GO paper (B), as a consequence of different thermal treatments: (a) unannealed; (b) 200 °C for 30 s; (c) 200 °C for 3 min; (d) 200 °C for 30 min; (e) 200 °C for 300 min; (f) 400 °C for 3 min. The d spacing,

expressed in nm, of the observed peaks is indicated. The insets in the top of the figures show photographs of GO (A) and b-GO (B) papers after treatment at 400 °C for 3 min.

As for GO paper treatments at 200 °C, the (001) peak progressively moves to higher diffraction angles and correspondingly the interlayer spacing reduces from 0.82 nm down to 0.40 nm. A weak but narrow graphitic peak at d=0.34 nm, for all the considered annealing conditions, also appears (**Fig. 5.2Ab–f**) and clearly indicates the formation of a minor amount of ordered graphitic structure. Even after the thermal treatment at 400 °C (**Fig. 5.2f**), the GO paper still contains minor amounts of reduced graphite oxide crystallites (peak at d=0.40 nm) as well as of graphite crystallites (peak at d=0.34 nm). Moreover, the GO paper after the thermal treatment at 400°C is fully disintegrated (see inset in the upper part of **Fig. 5.2A**).

Largely different are the WAXD patterns of the b-GO paper after thermal treatments at 200 °C and 400 °C (**Fig. 5.2Bb–f**), which all present only a broad amorphous halo, as for the b-GO paper annealed at 100 °C (**Fig. 5.1E, E' and E''**).

Particularly relevant is the maintenance of integrity of the b-GO paper, even after the thermal treatment at 400 °C, which is instead fully lost for GO paper (compare insets in the upper part of **Fig. 5.2A and B**, respectively).

Structural changes for GO and b-GO papers, as a consequence of room temperature microwave treatments have also been studied by WAXD patterns (as collected by powder diffractometer), as shown in **Fig. 5.3.**

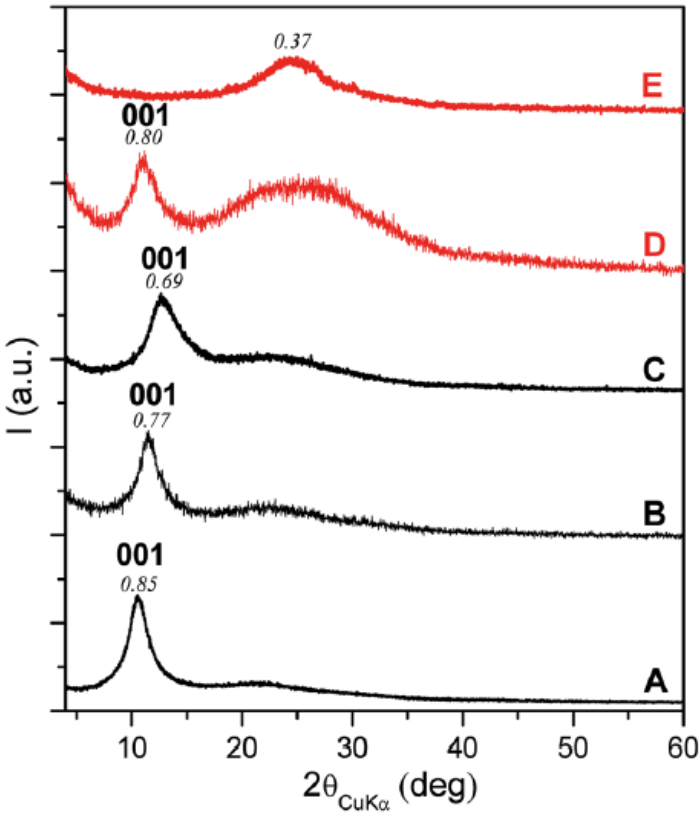

Figure 5.3 X-ray diffraction patterns (CuKα), as collected by an automatic powder diffractometer, for: GO paper untreated (A), microwave treated at 900 W for 2 min (B) and for 40 min (C); b-GO paper untreated (D) and microwave treated at 400 W for 15 s (E).

The (001) graphite oxide peak of the GO paper is gradually shifted toward higher 2θ values, and after 40 min of treatment the d spacing decreases from 0.85 nm down to 0.69 nm, with a reduction of the correlation length perpendicular to the graphitic layers from 4.4 nm to 3.5 nm **(Fig. 5.3A–C).** The (001) graphite oxide peak of the b-GO paper (**Fig. 5.3D**), on the contrary, after only 2 min of microwave treatment completely disappears leading to an amorphous halo (**Fig. 5.3E**), which is again indistinguishable from that one observed for the thermally treated b-GO paper (**Fig. 5.1E**). Elemental analysis of the microwave treated b-GO paper (last line of Table **5.**1) indicates a negligible reduction of oxygen content with respect to the

starting b-GO paper (3rd line of Table **5.**1), clearly showing that the amorphous halo centered at d=0.37 nm is due to loss of three dimensional order of graphene oxide layers rather than to their reduction.

Hence, the minor graphite oxide component of the b-GO paper, differently from the large graphite oxide component of GO paper, can easily loose (both by thermal or microwave treatments) its crystalline order perpendicular to the graphene oxide layers, always maintaining the GO paper integrity.

Relevant information on structural organization of b-GO paper also comes from N_2 sorption experiments. In fact, as prepared b-GO papers that maintain graphite oxide crystalline order (Fig. 1D) exhibit negligible BET surface areas (<1 m^2/g). b-GO paper samples, which have lost crystalline order perpendicular to the GO planes both by annealing at 100 °C (**Fig. 5.1E**) or by microwave treatments (**Fig. 5.3E**), present definitely higher BET values (4.6 +/- 0.1 m^2/g). BET surface area values further increase as a consequence of b-GO paper reduction processes, which maintain the complete loss of crystalline order perpendicular to the GO planes. For instance, for b-GO papers after 1 min of annealing at 400 °C and 500 °C, where the C/O weight ratio increases up to 1.9 and 2.6 (Table 1), the BET values increase up to 20 m^2/g and 75 m^2/g, respectively.

5.3 Thermal behavior

TGA and DSC measurements of GO and b-GO papers are compared in **Fig. 5.4**. TGA measurements (**Fig. 5.4A**) and the corresponding differential plot (DTGA, **Fig. 5.4B**) show the well-known thermal degradation phenomenon, corresponding to deoxygenation mainly by CO_2 evolution, **[41]** which for both GO and b-GO papers occurs at nearly 200 °C. However, the weight loss for the b-GO paper (11%) is close to one half of the weight loss of the GO paper (21%).

This nearly halved degradation phenomenon, for b-GO paper, is clearly confirmed by DSC measurements (**Fig. 5.4C**), which show that the corresponding exothermic peak (centered in the temperature range 195–

198°C) is also nearly halved. In fact, the enthalpy change is equal to 1.1 and 0.53 kJ/g, for GO and b-GO paper, respectively.

Both TGA and DSC measurements indicate that thermal deoxygenation phenomena, are largely depressed for b-GO paper with respect to GO paper. These data are also clearly confirmed by elemental analyses, as collected in Table 1. In fact, as consequence of treatment at 300°C, the C/O weight ratio of GO paper increases from 1.4 up to 4.6 (1st and 2nd lines of Table 1) while for the b-GO paper only increases from 1.1 up to 1.7 (3rd and 4th lines of Table 1). Elemental analyses of b-GO paper treated at 400°C and 500°C (5th and 6th lines of Table 1) show that the C/O weight ratio increases only up to 2.6.

Hence, after treatment at 300°C, the GO paper has an oxygen content of 17.8 wt% while the b-GO paper has a nearly double oxygen content (37wt%). A possible molecular origin of the definitely more difficult thermal deoxygenation of b-GO papers, with respect to GO papers, is discussed in Section 4.6.

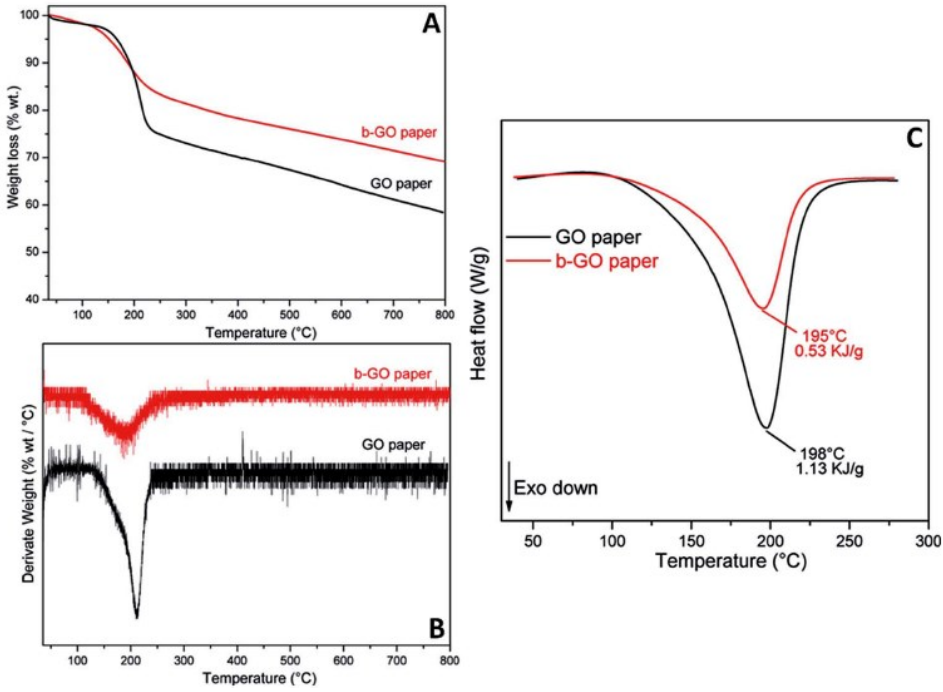

Figure 5.4. Scans at heating rate of 10 °C/min of GO paper (black line) and b-GO paper (red line): (A) TGA; (B) DTGA; (C) DSC.

5.4 Dimensional stability in solvents

Although b-GO paper exhibits an oxygen content definitely higher than for usual GO paper (see, elemental analysis in Table 4.1), they present a much higher dimensional stability when dispersed in both polar and apolar solvents, mainly in the presence of sonication.

TABLE 5.1. Elemental analysis of different papers based on GO.[a]

Paper	C (wt%)	H (wt%)	O (wt%)	C/O
GO	57.2	1.4	41.3	1.4
GO (300°C)	81.8	0.6	17.6	4.6
b-GO	52.1	0.9	47.0	1.1
b-GO(300°C)	62.4	0.8	37.6	1.7
b-GO (400°C)	64.9	1.1	33.8	1.9
b-GO (500°C)	71.4	1.2	27.4	2.6
b-GO (microwave)	52.4	1.0	46.6	1.1

[a] Elemental composition of anhydrous samples: The error in C and O content is close to 1wt% while the error in H content is close to 0,1 wt%; water contents (as evaluated by TGA, after equilibration at room temperature in air with a relative humidity of 45%) was in the range 13±2 wt%, for all the examined samples.

The dimensional stability in the presence of some solvents, after vigorous stirring and three months of storage, for GO paper (by vacuum filtration) and for b-GO papers (both by vacuum filtration and casting procedures), is shown by photographs of vials in **Fig. 5.5**.

Both b-GO papers maintain their dimensional integrity after sonication in organic solvents like acetone, ethanol and hexane while the GO paper breaks in many pieces.

Both b-GO papers are also completely stable to sonication in polar organic solvents, like dimethylformamide (DMF, lower part of **Fig. 5.5**) and N-methyl-pyrrolidone (NMP), with solvents remaining fully transparent, while the GO paper in part goes back into suspension and the solvents become heavily turbid.

In water (intermediate part of **Fig. 5.5**), the GO paper comes back to GO suspension, the b-GO(VF) paper breaks in few pieces also losing some fine particles (less than 1 wt%) that generate water turbidity, while b-GO(C) paper remains intact in fully transparent water.

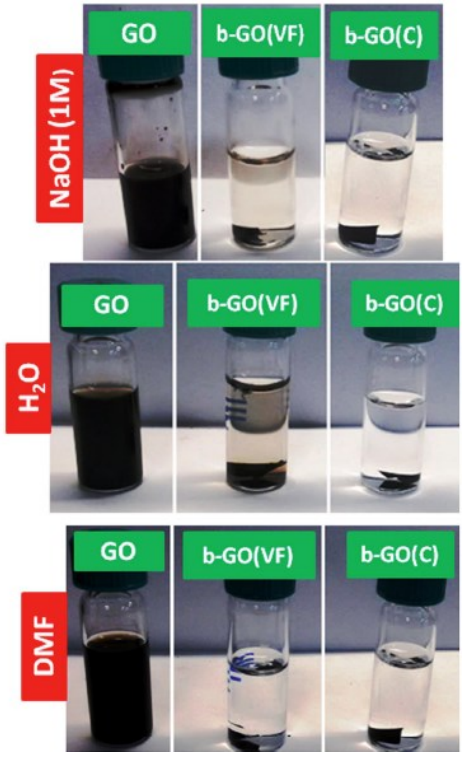

Figure 5.5. Photographs of vials containing three different solvents (dimethylformamide, water and NaOH 1 M aqueous solution) and three different kinds of papers: GO; b-GO by vacuum filtration (b-GO(VF)) and b-GO by casting (b-GO(C)). The photographs have been taken after vigorous stirring and three months of storage.

b-GO(C) paper also exhibits a remarkable dimensional stability in acidic and alkaline aqueous solutions, also for high concentrations. This is shown, for instance, in the upper part of **Fig. 5.5**, for a 1 M aqueous solution of NaOH, which fully destroys GO paper and becomes slightly turbid in the presence of b-GO(VF). An analogous behavior is observed for the same GO papers in 1 M aqueous solutions of HCl.

It is worth adding that b-GO papers exhibit the above described high solvent resistance both before and after the acidic treatment leading to ion

removal. Hence, the high solvent resistance of b-GO papers is not due to interactions involving the added metal cations or possible multivalent cationic metal contaminants.

5.5 Paper flexibility

Mechanical properties of b-GO paper are comparable or even better than those of the usual GO paper. This is shown, for instance, for bending tests evaluating radius of curvature (as one half of the minimum opening of a gauge, before sample breaking, see **Fig. 5.6A**) of papers of different thickness.

The plot of **Fig. 5.6B** clearly shows that papers by vacuum filtration present similar radius of curvature, irrespective of the preparation from GO or b-GO (upper curve). However, cast papers that were obtained only from b-GO suspensions exhibit a definitely higher flexibility (lower curve with red squares). In particular, the cast paper with lowest thickness (12 mm) is fully foldable, i.e., does not break in our bending test, even for radius of curvature equal to zero. It is worth adding that this 12 mm b-GO paper survived a repeated folding test (1000 folds) with a curvature radius of 200 mm. Moreover, after the repeated folding test the thin paper was crumpled (**Fig. 5.6C**) and then laid out in a plane (**Fig. 5.6D**), without any fracture.

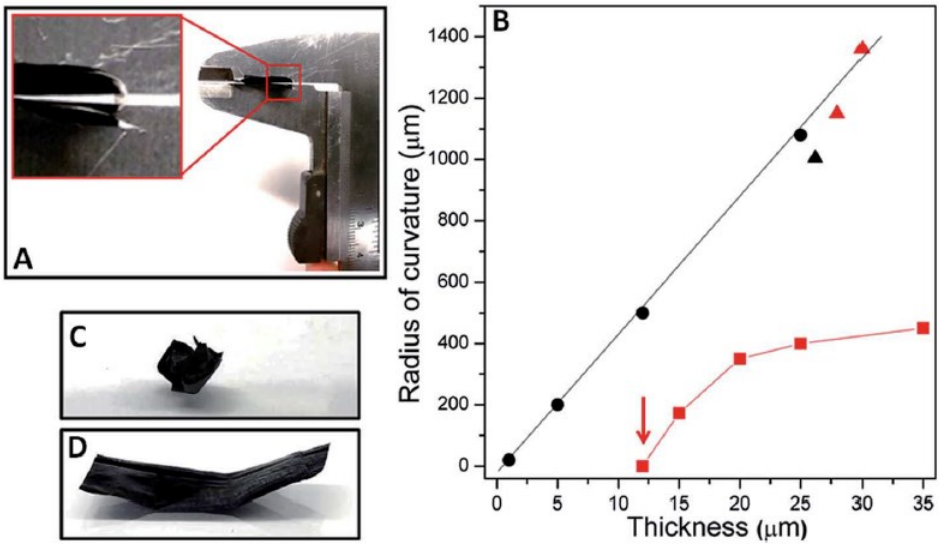

Figure 5.6. (A) Bending tests evaluating the minimum opening of a gauge, before paper breaking. (B) The radius of curvature, calculated as one half of this minimum opening, reported versus the papers thickness, for b-GO papers and GO papers. In particular, triangles indicate data for papers by vacuum filtration, squares data for papers by casting while circles indicate literature data taken from Ruoff et al.20 An arrow indicates the cast b-GO paper that is fully foldable, i.e. does not break in our bending test. (C and D) Photographs of a 12 mm b-GO paper: (C) crumbled (D) and then laid out in a plane.

5.6 FTIR characterization and possible rationalization of b-GO properties

Many favorable properties of b-GO paper with respect to GO paper could be rationalized by formation of covalent bonds between GO layers: (i) largely improved filmability, which is generally associated with higher molecular masses of the dispersed molecules; (ii) largely improved solvent resistance, which is generally associated with crosslink formation; (iii) paper integrity after complete loss of stacking order of GO as induced by thermal or microwave treatments, which again is favored by covalent bonds between graphene layers; (iv) higher paper density, irrespective of lower crystallinity, of higher oxygen content and of lower degree of planar orientation.

This section reports an infrared characterization of functional group on the GO layers, aiming to understand the chemical nature of the possible covalent links between GO layers. The FTIR reflection–absorption spectra of the prepared GO papers have been studied for the range 4000–400 cm^{-1} and are compared for the spectral range 2000–800 cm^{-1}, in **Fig. 5.7**.

The FTIR spectra of the GO paper (**Fig. 5.7A**) present peaks at 825 cm^{-1} and 1275 cm^{-1}, due to the bending and asymmetric stretching modes of the epoxy (C–O–C) group, and a peak at 1740 cm^{-1}, which is generally attributed to C-O stretching vibration of carboxylic functionalities.**[25]** The intense peak at 1640 cm1, can be possibly attributed to an overlap of different vibrational modes as C]C stretching vibration46 (which is activated in GO due to oxygen functional groups and defects) and bending mode of intercalated water.**[26]**

Largely different are the spectra of the obtained b-GO papers that are mainly characterized by a very broad band roughly centered at 1335 cm^{-1} (Fig. 7B), which does not help to establish the chemical nature of the functional groups on the layers.

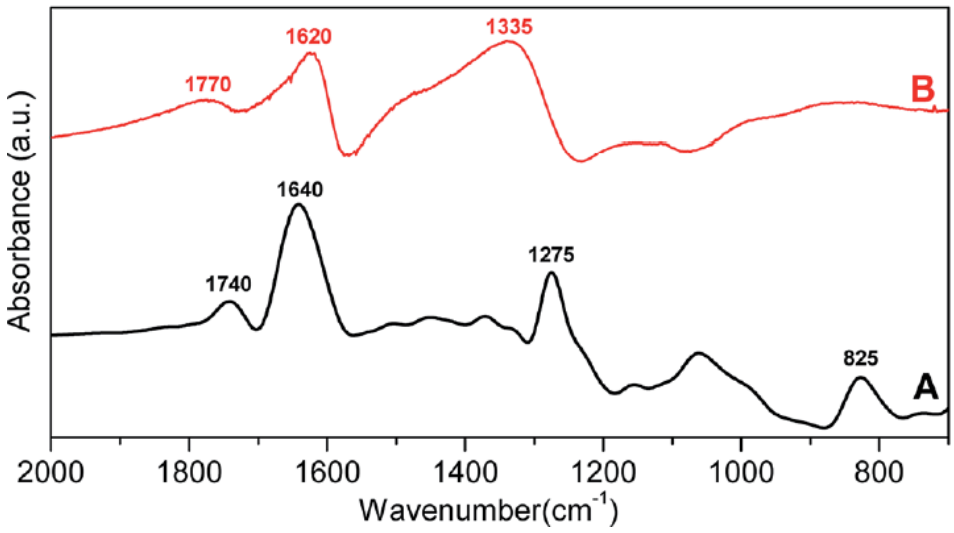

Fig. 5.7 FTIR reflection–absorption spectra of GO paper (A) and b-GO paper (B) for the spectral range 2000–800 cm1.

However, the b-GO spectra show, beside a clear reduction of the carboxylic 1740 cm^{-1} peak (indicating a partial decarboxylation, usually associated with alkaline induced reduction) the complete disappearance of the epoxy vibrations at 825 cm^{-1} and 1275 cm^{-1}.

The disappearance of the epoxy groups shows that the NaOH concentration (0.05 M) used for b-GO preparation is effective to promote epoxy ring opening reaction (**Fig. 5.8A**), which produces alkoxy ions.**[27]** Some of these ions could attack the epoxy ring of a close layer (**Fig. 5.8B**), thus producing interlayer ether bonds (**Fig. 5.8C**).

The chemical mechanism for interlayer covalent bond formation, proposed in **Fig. 5.8**, is also able to rationalize the decreased thermal deoxygenation, as observed for b-GO papers (**Fig. 5.4**), irrespective of their higher oxygen content [(C/O)b-GO=1.1 vs. (C/O)GO=1.4]. In fact, the replacement of most hydroxyl groups by ether bonds in the paper preparation procedure would reduce the thermal decarboxylation reaction, which would be mainly based on disproportionation of hydroxyl groups of graphite oxide.**[28][29]**

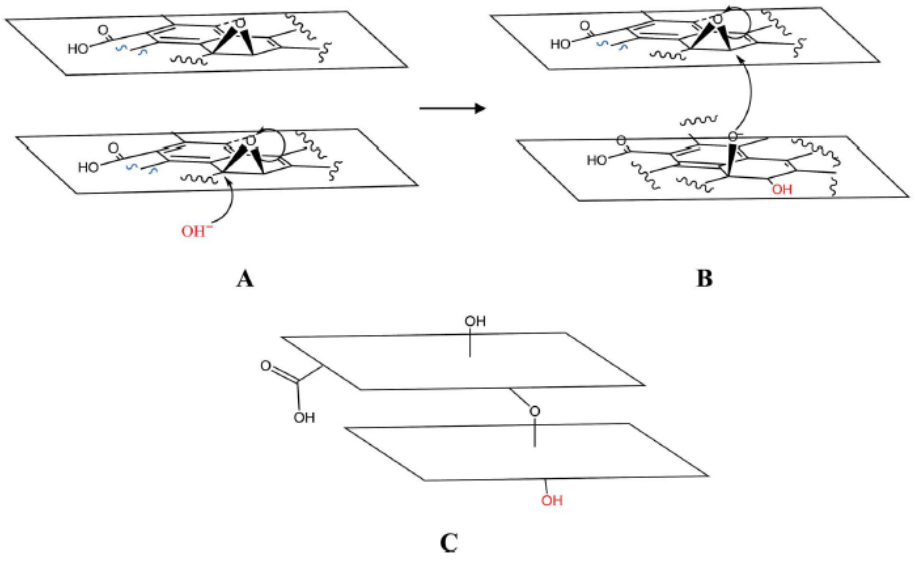

Fig. 5.8 Proposed mechanism for interlayer covalent bond formation for b-GO paper.

Conclusions

The ability of GO aqueous suspensions to form robust GO paper is largely improved by basification of the suspension prior of vacuum filtration or casting procedures. In particular, casting procedures, which generally lead to brittle GO paper, for the case of basified GO suspensions lead to tough papers of macroscopic size, for a broad range of thickness (at least in the range 5–50 mm).

Flexibility of b-GO papers, when obtained by casting procedures, is definitely improved with respect to usual GO papers. In particular, cast b-GO papers with low thickness (≈10 mm) do not break in our bending test, even for radius of curvature equal to zero.

Differently from usual GO papers, b-GO papers exhibit a remarkable dimensional stability, after thermal or solvent treatments. Dimensional stability in solvents is observed even after sonication and differences with

respect to GO papers are particularly impressive in the presence highly polar solvents, like water or DMF or NMP.

X-ray diffraction analyses indicate that b-GO papers have a much larger amorphous component. Thermal treatments of b-GO paper easily produce complete loss in stacking order of graphene oxide layers while thermal treatments of GO paper lead to their disintegration but only to partial loss in stacking order. Also microwave treatments at room temperature of b-GO paper easily lead to loss in stacking order of graphene oxide layers.

TGA and DSC measurements show that, for b-GO papers, thermal deoxygenation phenomena are less than halved with respect to those observed for GO paper.

Physical and chemical properties of b-GO paper suggest the
formation of interlayer covalent bonds. Infrared characterizations indicate that the main change observed moving from GO to b-GO papers is the disappearance of the epoxy peaks. This indicates that relevant properties of b-GO are induced by reactions of the hydroxyl ions with the epoxy groups on the GO layers. A possible mechanism leading to formation of interlayer ether bonds, for b-GO paper, is proposed.

References

[1] S. Park and R. S. Ruoff. *Nat. Nanotechnol.* **2009**, 5, 217–224.

[2] H. Kim, A. A. Abdala and C. W. Macosko, *Macromolecules* **2010**, 43, 6515–6530.

[3] R. Sengupta, M. Bhattacharya, S. Bandyopadhyay and A. K. Bhowmick. *Prog. Polym. Sci.* **2011**, 36, 638–670.

[4] M. Mauro, V. Cipolletti, M. Galimberti, P. Longo and G. Guerra. *J. Phys. Chem. C* **2012**, 116, 24809–24813.

[5] X. Zhang, Z. Sui, B. Xu, S. Yue, Y. Luo, W. Zhan. *et al. J. Mater. Chem.* **2011**, 21, 6494–6497.

[6] M. A. Worsley, P. J. Pauzauskie, T. Y. Olson, J. Biener, J. H. Satcher Jr and T. F. Baumann. *J. Am. Chem. Soc.* **2010**, 132, 14067–14069.

[7] M. A. Worsley, T. Y. Olson, J. R. I. Lee, T. M. Willey, M. H. Nielsen, S. K. Roberts, *et al. J. Phys. Chem. Lett.* **2011**, 2, 921–925.

[8] S. Nardecchia, D. Carriazo, M. L. Ferrer, M. C. Guti´errez and F. del Monte. *Chem. Soc. Rev.* **2013**, 42, 794–830.

[9] H. Hu, Z. Zhao, W. Wan, Y. Gogotsi and J. Qiu, *Adv. Mater.* **2013**, 24, 2219–2223.

[10] T. Wu, M. Chen, L. Zhang, X. Xu, Y. Liu, J. Yan, *et al. J. Mater. Chem. A* **2013**, 1, 7612–7621.

[11] S. Longo, M. Mauro, C. Daniel, P. Musto and G. Guerra, *Carbon* **2014**, 77, 896–905.

[12] D. A. Dikin, S. Stankovich, E. J. Zimney, R. D. Piner, G. H. B. Dommett, G. Evmenenko, *et al. Nature* **2007**, 448, 457–460.

[13] Y. Xu, H. Bai, G. Lu, C. Li and G. Shi. *J. Am. Chem. Soc.* **2008**, 130, 5856–5857.

[14] S. Park, J. An, I. Jung, R. D. Piner, S. J. An, X. Li, *et al. Nano Lett.* **2009**, 9, 1593–1597.

[15] S. Pei, J. Zhao, J. Du, W. Ren and H.-M. Cheng. *Carbon* **2010**, 48, 4466–4474.
[16] O. C. Compton and S. T. Nguyen. *Small* **2010**, 6, 711–723.
[17] F. Liu S. Song, D. Xue and H. Zhang, *Adv. Mater.* **2012**, 24, 1089–1094.
[18] W. Wan, Z. Zhao, H. Hu, Y. Gogotsi and J. Qiu. *Mater. Res. Bull.* **2013**, 48, 4797–4803.
[19] R.-Y. Liu and A.-W. Xu. *RSC Adv.* **2014**, 4, 40390–40395.
[20] M. Kim, D. Y. Kim, Y. Kang and O. O. Park. *RSC Adv.* **2015**, 5, 3299–3305.
[21] M. Mauro, M. Maggio, V. Cipolletti, M. Galimberti, P. Longo and G. Guerra. *Carbon* **2013**, 61, 395–403.
[22] C.-J. Kim, W. Khan and S.-Y. Park. *Chem. Phys. Lett.* **2011**, 511, 110–115.
[23] M. Mauro, M. Maggio, A. Antonelli, M. R. Acocella and G. Guerra. *Chem. Mater.* **2015**, 27, 1590–1596.
[24] H. Shang, Y. Lu, F. Zhao, C. Chao, B. Zhang and H. Zhang. *RSC Adv.* **2015**, 5, 75728–75734.
[25] C.-N. Yeh, K. Raidongia, J. Shao, Q.-H. Yang and J. Huang. *Nat. Chem.* **2015**, 7, 166–170.
[26] J. W. Kim, D. Kang, T. H. Kim, S. G. Lee, N. Byun, D. W. Lee, *et al. ACS Nano* **2013**, 7, 8082–8088.
[27] T. Taniguchi, S. Kurihara, H. Tateishi, K. Hatakeyama, M. Koinuma, H. Yokoi, *et al. Carbon*, **2015**, 84, 560–566.
[28] A. M. Dimiev, L. B. Alemany and J. M. Tour. *ACS Nano* **2013**, 7, 576–588.
[29] M. Maggio, M. Mauro, M. R. Acocella, G. Guerra. *RSC Adv.* **2016**, 6, 44522–44530.

General conclusions

New layered carbon-based materials were prepared and exhaustively characterized exploiting different characterization techniques, such as thermogravimetry (TGA), differential thermal calorimetry (DSC), Fourier transform infrared (FTIR) and wide angle X-ray diffraction (WAXD).

Pristine graphite (G) with high surface area and carbon black (CB) samples with different surface areas were selected as starting materials to prepare the corresponding oxidized samples, *i.e.* graphite oxide (GO) and carbon black oxide (oCB), with the Hummers' method.

Thanks to the strong hydrophilicity and to the lamellar structure of oxidized carbon-based materials, a rich intercalation chemistry is permitted.

In fact, after treatments of GO and oCB by strong basis, ordered intercalation compounds have been obtained, not only if the starting material is crystalline like graphite oxide, but also if it is completely amorphous like oxidized carbon black.

Starting basified GO, free-standing papers can be obtained by vacuum filtration, as well as by casting procedure, of colloidal dispersions of graphene oxide sheets.

The use of basified GO leads to more flexible, solvent resistant and thermally stable GO papers. Spectroscopic analyses of the obtained papers have been conducted aiming to a possible rationalization of the observed behavior.